FRETTING WEAR AND FRETTING FATIGUE OF Ti-6Al-4V

DIPLOMA THESIS

Josip Jurič

MONTANUNIVERSITÄT LEOBEN
Chair of Mechanical Engineering
Leoben, Austria

SUPERVISORS

Univ.-Prof. Dipl.-Ing. Dr. Wilfried Eichlseder
Chair of Mechanical Engineering, Montanuniversität Leoben, Austria
Dipl.-Ing. Dr. Bernd Oberwinkler
Chair of Mechanical Engineering, Montanuniversität Leoben, Austria

Leoben, June 2010

AFFIDAVIT

I declare in lieu of oath, that I wrote this thesis and performed the associated research myself, using only literature cited in this volume.

Josip Jurič

Leoben, June 2010

Acknowledgements

This diploma thesis was prepared at the Chair of Mechanical Engineering at the Montanuniversität Leoben (Austria).

I would like to thank **Univ.-Prof. Dipl.-Ing. Dr. Wilfried Eichlseder**, the head of the Chair of Mechanical Engineering, who laid the foundation for this work.

Special thanks to **Dipl.-Ing. Dr. Bernd Oberwinkler**. I thank him for teaching me in admirable simplicity and clarity, for many good ideas, his open-mindedness, for providing me vast freedom and great support in scientific as well as in organizational concerns. In fact, I cannot imagine a better supervisor than him.

Furthermore, I would like to thank all colleagues at the Chair of Mechanical Engineering, who supported me during my research. Special thanks to Dipl.-Ing. Johannes Reiser for his helpfulness.

Index of contents

1. Abstract

1.1. Abstract (English)

Titanium alloys and especially Ti-6Al-4V combine good mechanical properties such as high strength and excellent corrosion resistance with low density. The examples of applications have a wide range, from medical and automotive to aerospace engineering. Using more and more lightweight components for reduction of weight and increase of capacity leads to reduced stiffness, augmented oscillatory movements between contact surfaces, and finally to fretting damage.

The fretting behavior of the titanium alloy Ti-6Al-4V was characterized with fretting wear and fretting fatigue tests. Fretting wear tests were performed to characterize the wear behavior in respect of varying parameters such as contact pressure, relative slip amplitude and fretting cycles. Based on fretting tests at different temperatures caused by varying testing frequencies, the influence of temperature on fretting behavior was investigated. Fretting fatigue test were conducted to determine the reduction of durability in comparison to plain fatigue tests. Furthermore, the influence of different Ti-6Al-4V microstructures on fretting wear and fretting fatigue life was investigated.

Fretting wear tests showed that with increasing fretting cycles or relative slip amplitude, the wear mass increases, whereas no influence of the contact pressure was observed. A comparison of different Ti-6Al-4V microstructures revealed, that the bimodal microstructure has the highest wear resistance.
Fretting fatigue tests showed an essential reduction of durability due to fretting conditions in comparison to plain fatigue tests. The highest fretting fatigue strength of all investigated microstructures was determined for the mill-annealed microstructure.
The fretting fatigue strength of Ti-6Al-4V was estimated with existing fatigue models and the aid of finite element analysis. It was observed, that the equivalent stresses in the fretting contact were responsible for the fretting fatigue damage. They cause a local low cycle fatigue loading in spite of the global high cycle fatigue load of the specimen.

The performed fretting tests and the detailed analysis are the basis for the inclusion of the fretting damage in lifetime estimation of Ti-6Al-4V components.

1.2. Abstract (German)

Titanlegierung und insbesondere Ti-6Al-4V zeichnen sich durch gute mechanische Eigenschaften wie hohe Festigkeit, gute Korrosionsbeständigkeit und niedrige Dichte aus. Deshalb reichen die Anwendungsgebiete von Medizintechnik über Fahrzeugbau bis zur Luft- und Raumfahrt. Durch den zunehmenden Einsatz von Leichtbaukomponenten zur Gewichtsreduktion und Nutzlasterhöhung wird die Steifigkeit reduziert. Dies führt unter dynamischer Beanspruchung verstärkt zu oszillatorischen Schwingungen welche zu Fretting-Schädigungen und in weiterer Folge zum Versagen des Bauteils führen können.

Das Fretting-Verhalten von Ti-6Al-4V wurde mittels Fretting-Wear und Fretting-Fatigue Versuchen charakterisiert. Fretting-Wear Versuche wurden durchgeführt, um das Verschleißverhalten in Abhängigkeit von Parametern wie Kontaktdruck, relative Verschiebungsamplitude und Fretting-Zyklen zu ermitteln. Basierend auf Fretting-Versuchen mit unterschiedlichen lokalen Temperaturen, verursacht durch die variierenden Testfrequenzen, wurde der Einfluss der Temperatur auf das Fretting-Verhalten ermittelt. Fretting-Fatigue Versuche wurden ausgeführt, um den Lebensdauerabfall im Vergleich zu normalen Ermüdungsversuchen zu bestimmen. Desweiteren wurde der Einfluss von verschiedenen Ti-6Al-4V Mikrostrukturen auf das Fretting-Wear und die Fretting-Fatigue Lebensdauer untersucht.

Die Fretting-Wear Versuche zeigten, dass mit Anstieg der Fretting-Zyklen und der relativen Amplitude die Verschleißmasse ansteigt, während kein Einfluss des Kontaktdrucks festgestellt wurde. Im Vergleich der verschiedenen Ti-6Al-4V Mikrostrukturen, wies die bimodale Mikrostruktur die höchste Verschleißresistenz auf.
Fretting-Fatigue Versuche zeigten, dass Fretting zu einem essentiellen Lebensdauerabfall im Vergleich zu normalen Ermüdungsversuchen führt. Die mill-annealed Mikrostruktur, führte dabei zu den höchsten Fretting-Fatigue-Festigkeiten.
Die Fretting-Schwingfestigkeit von Ti-6Al-4V wurde mit existierenden Modellen und unter Zuhilfenahme der Finite-Elemente-Methode abgeschätzt. Dabei konnte gezeigt werden, dass erhöhte Vergleichsspannungen im Fretting-Kontakt für die Fretting-Fatigue-Schädigung verantwortlich sind. Diese verursachen eine lokale Low-Cycle-Fatigue Belastung trotz globaler High-Cycle-Fatigue Belastung der Frettingprobe.

Die durchgeführten Fretting-Versuche und die detaillierten Analysen bilden die Basis für eine Implementierung der Fretting-Schädigung in die Lebensdauerberechnung von Ti-6Al-4V Komponenten.

2. Introduction

The role of the mechanics of tribology is increasingly an important field for the industrial needs. Using more and more lightweight components for reduction of weight and increase of capacity, augmented oscillatory movements between contact surfaces occur. This leads due to reduced stiffness of components to fretting damage, which is a complex tribological process with multiple influencing variables.

Fretting can lead to a decrease of durability due to fretting wear, fretting fatigue and/or fretting corrosion. It is been noted in fatigue testing under fretting conditions that the fatigue strength can be reduced up to 50 to 70% in comparison to plain fatigue tests.

Fretting wear occurs when surfaces of two bodies in contact make a small relative oscillatory displacement through an external force or vibration. Does the oscillatory displacement in the contact surface occur through a cyclic load then we spoke about fretting fatigue. The damage with creation of oxidative wear particles is called fretting corrosion. The characteristic damage due to fretting is the formation of debris and crack initiations between two bodies in contact. [27]

The fretting fatigue phenomenon can be characterized by the following main features:

- Stick-slip conditions with highly concentrated surface damage
- Relatively low wear and debris formation
- Non-proportional and multiaxial contact stress state
- High stress gradients
- Contained plastic deformations and material transfer at the contacting surfaces

This diploma thesis investigates the influences of fretting on the fatigue behavior of the titanium-base alloy Ti-6Al-4V. Thereby, different influences on fretting wear and fretting fatigue such as microstructure, temperature, relative slip amplitude, fretting cycles and contact pressure are analyzed.
Fretting wear tests with varying relative slip amplitude, normal load and fretting cycles are performed with a purpose designed rig. The measurements of dissipated energy, wear mass, frictional force and temperature during fretting wear tests, allow a qualitative evaluation of the fretting process.
The influence of different microstructures of Ti-6Al-4V on fretting wear, are investigated. For the comparison of the fretting wear tests with different microstructures, an indicator for the resistance against fretting, the wear energy density, is used. Furthermore, the influence of microstructure on the fretting fatigue behavior of Ti-6Al-4V is investigated and evaluated. Fretting tests are conducted at varying testing frequencies to determine the influence of frequency and hence temperature (friction-caused heating) on surface damage and wear loss.
The fretting contact is modeled in a finite element analysis, to compute the stress state in the fretting zone. Further a model for the fretting fatigue strength of Ti-6Al-4V is estimated with existing fatigue models and simulated plain fatigue results.

3. State-of-the-art

3.1. Tribology

Tribology is the science and engineering of interacting surfaces in relative motion. It includes the study and application of the principles of friction, lubrication, wear and their interrelationships. Tribology is crucial to modern machinery which uses sliding and rolling surfaces. Examples of productive friction are brakes, clutches, driving wheels on trains and automobiles, bolts and nuts. Examples of productive wear are writing with a pencil, machining, polishing and shaving. Examples where unproductive friction and wear occur are internal combustion and aircraft engines, gears, cams, bearings and seals. [5]

The ambition of tribology is the optimization of tribological systems, in detail:

- Progression of the degree of efficiency and of the capacity
- Increase of the reliability and durability
- Decrease of the costs of maintenance

3.1.1. History of tribology

One of the first known applications in reducing friction in translationary motion was used by the Egyptians circa 1880 BC at the transportation of large statues. In a illustration of such a transportation, 172 slaves are being used to drag a large statue, weighting about 61 tf along a wooden track. One man, standing before the statue, is pouring a liquid into the path of motion. Perhaps he was one of the earliest lubrication engineers. [5]

The first scientific approach concerning friction was done by Leonardo da Vinci (1452-1519). Da Vinci deducted the laws governing the motion of a rectangular block sliding over a flat surface. He introduced, for the first time, the concept of coefficient of friction as the ratio of the friction force to normal load. However, his work had no historical influence, because his notes remained unpublished for hundreds of years. In 1699, the French physicist Guillaume Amontons rediscovered the laws of friction after he studied dry sliding between two flat surfaces. He ascertained that the friction force that resists sliding at an interface is directly proportional to the normal load. Furthermore, he found out that the amount of friction force does not depend on the apparent area of contact. These observations were verified by French physicist Charles-Augustin Coulomb, which added a third law that proves that the friction force is independent of sliding speed. He also made a clear distinction between static friction and kinetic friction. [5]

Many other developments occurred during the 1500s, particularly in the use of improved bearing materials. Further developments were associated with the growth of industrialization in the latter part of the eighteenth century. Early developments in the petroleum industry started in the 1850s.
The essential laws of viscous flow were postulated by Sir Isaac Newton in 1688. The scientific understanding of lubricated bearing operation did not occur until the end of the nineteenth century. Indeed, the beginning of our understanding of the principles of hydrodynamic lubrication was afforded by the experimental studies of Beauchamp Tower (1884) and the theoretical interpretations of Osborne Reynolds (1886) and related work by N.P. Petroff (1883). Since then, hydrodynamic bearing theory and practice developed extremely rapid to meet the demand for reliable bearings in new machinery. [5]

Wear is a much younger subject than friction and bearing development, and it was initiated on a largely empirical basis. Scientific studies of wear developed little until the mid-twentieth century. Ragnar Holm [20] made one of the earliest substantial contributions to the study of wear. [5]

The industrial revolution (1750-1850 AD) is recognized as a period of rapid and impressive development of the machinery of production. The use of steam power and the subsequent development of the railways in the 1830s led to promotion of manufacturing skills. Since the beginning of the twentieth century, from enormous industrial growth leading to demand for better tribology, knowledge in all areas of tribology has expanded tremendously. [5]

3.1.2. Tribological system

Compared to material parameters such as tensile strength or elastic modulus, the resistance opposite to wear is not a well defined material parameter. It depends on interrelations between all involved elements of the wear act, which can be summarized in the tribological system (Fig. 3.1). A tribological system consists of the surfaces of two components that are in moving contact and their according surroundings.
The tribological system depends on time, because in the wear act the initial and final condition are entirely different.

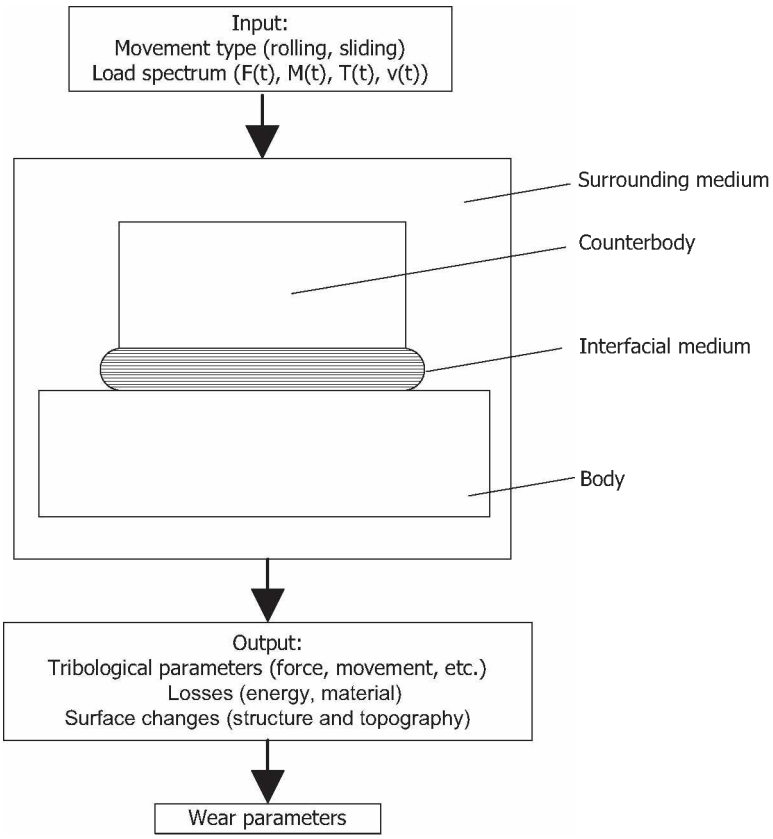

Fig. 3.1: Tribological system

3.1.3. Surface topography

The surface characteristic of the friction partners is basically affected by the progression of the interaction process. Tribological relevant for the surface properties are [14]:

- Micro geometry of the surface
- Elastic and plastic contact properties
- Surface energy- wetting ability
- Addiction to adhesion
- Microstructure
- Adsorption- and reaction films
- Coatings

As depicted in Fig. 3.2, the surface of a metal component may consist of a number of layers. The work-hardened layer is formed by plastic deformation during the manufacturing process. The yield properties of this layer differ significantly from the substrate metal; In addition, the manufacturing process induces residual stresses. Most metals oxidize and a layer of oxides normally form on top of the work-hardened layer. Some adsorbed wetness or gas is often present on top of the oxide film and the topmost layer contains contaminants such as dirt or grease. The contaminant and oxide layers are often quite thin and have an effect on the coefficient of friction between two surfaces. Their influence on the overall elastic behavior of the contact is generally small. However, work-hardening generally affects the yield properties of a material rather than its elastic properties. Yield properties are relevant in cases of surface-initiated material failure. [17]

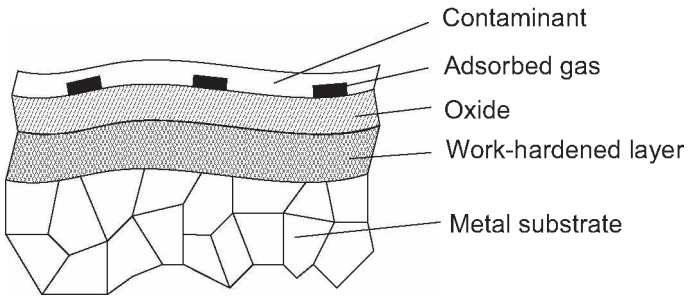

Fig. 3.2: Schematic illustration of the surface structure of a metal [6]

In addition to a complex material behavior, real surfaces also exhibit a complex geometry. No surface is microscopically flat and there is always a scale at which some of asperity can be detected.
It is convenient to differentiate between micro geometry (roughness), meaning the small scale irregularities of a surface, and form error, which is a measure of the deviation of the shape of the surface from its intended ideal shape (e.g. plane, cylindrical or spherical). Most commonly used measures for micro geometry are the arithmetic mean height R_a, (Equ. (3.1)), and the root mean square R_q, (Equ. (3.2)). [21]

$$R_a = \frac{1}{l_m} \cdot \int_0^{l_m} |y(x)| dx \qquad \text{Equ. (3.1)}$$

$$R_q = \sqrt{\frac{1}{l_m} \cdot \int_0^{l_m} y^2(x) dx} \qquad \text{Equ. (3.2)}$$

Fig. 3.3 shows an illustration of a roughness profile with marked arithmetic mean height and root mean square.

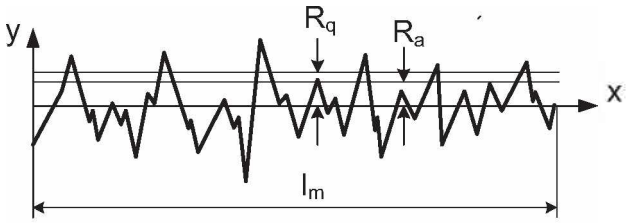

Fig. 3.3: Roughness profile

3.1.4. Contact between surfaces

In general there are two different contact types, cf. Fig. 3.4. If a cylinder is lightly pressed onto an elastic half-plane, a contact is generated along a line. This line becomes a narrow strip if the load is increased. This is an example of an incomplete contact. Extent of the contact is not fixed geometrically but depends on the applied load. These two bodies have a common tangent at the edge of the contact. The distribution of contact pressure is continuous and at the edge, pressure falls continuously to zero.
An example for a complete contact is given, when a flat ended punch is pressed into an elastic plane. Here the size of the contact is independent of the load. The two bodies have not a common tangent at the edge of the contact. By a complete contact, stress peaks occur at the edge of the contact. [17], [57]

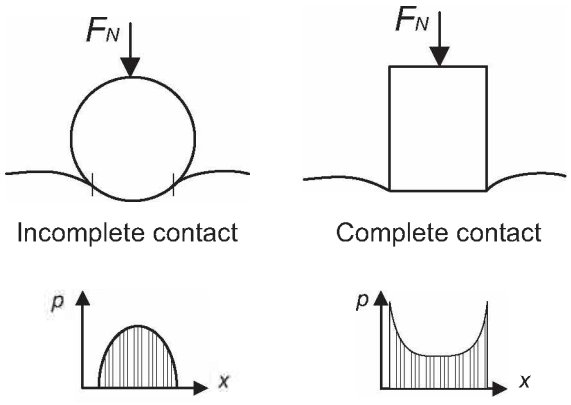

Fig. 3.4: Contact types [17]

In the elastic range of the material, the theory of Heinrich Hertz (1881) is commonly used to describe the contact. For example, if a sphere with radius R of an elastic material is pressed against a plane (cf. Fig. 3.5) under a normal load F_N, contact will occur between the two over a circular area of radius a, Equ. (3.3). [21]

$$a = \sqrt[3]{\frac{3 \cdot F_N \cdot R}{4 \cdot E}} \qquad \text{Equ. (3.3)}$$

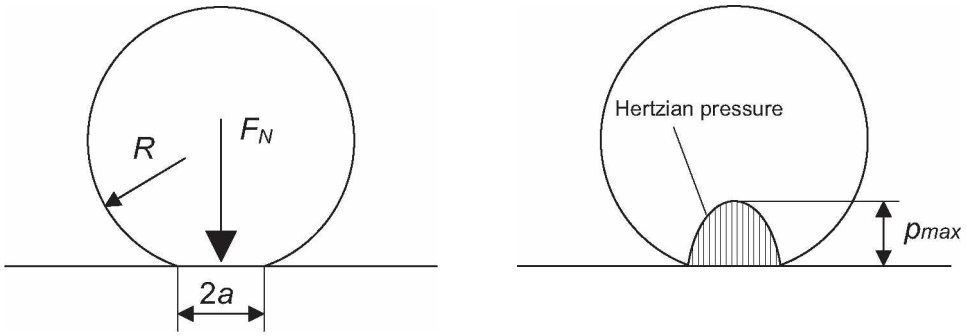

Fig. 3.5: Contact between a sphere and a plane surface under a load F_N

The elastic modulus which depends on Young's moduli, E_1 and E_2, and on the Poisson's ratios, ν_1 and ν_2, of the materials of the sphere and of the plane is defined in Equ. (3.4). The Hertzian pressure p_{Hertz} over the contact area is the ratio of the normal load F_N to the contact area $\pi \cdot a^2$ (cf. Fig. 3.5). The maximum pressure p_{max} is at the centre of the sphere. [21]

$$\frac{1}{E} = \frac{(1-\nu_1^2)}{E_1} + \frac{(1-\nu_2^2)}{E_2} \qquad \text{Equ. (3.4)}$$

In real contacts, when two nominally plane and parallel surfaces are brought gently together, contact will initially occur at only a few points. As the normal load is increased, the surface move closer together and a larger number of the higher areas or asperities on the two surfaces come into contact. Since these asperities provide the only points at which the surfaces touch, they are responsible for supporting the normal load on the surface and for generating any frictional forces which act between them. [21]

3.1.5. Friction

Friction is the resistance to the sliding of one solid body over or along another, as solid bodies are ordinarily understood in the macroscopic world. [4]
Frictional contact is usually assumed to be either „lubricated' or „dry'. When bodies are in lubricated contact, they are not in real contact at all; a thin layer of liquid or gas separates them. Most of the metal to metal contacts in a car engine are supposed to be lubricated. [45]
Subject to the movement type of the friction pairs a distinction is drawn between different friction modes (cf. Fig. 3.6).

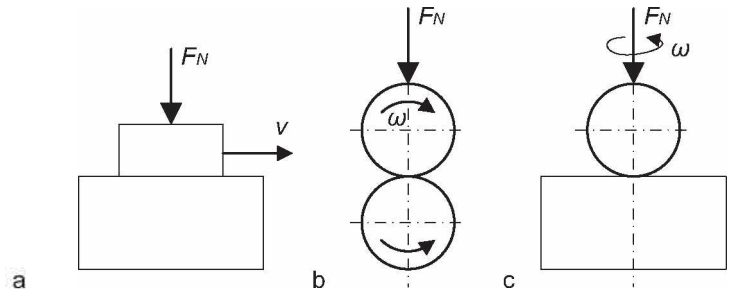

Fig. 3.6: Movement types of friction pairs: (a) sliding, (b) rolling (c) drilling [16]

The following friction conditions are defined according to DIN 50 320:

- Dry friction
- Lubricated friction
- Gas friction
- Mixed friction

Dry friction resists relative lateral motion of two solid surfaces in contact. Lubricated friction and gas friction resists relative lateral motion of two solid surfaces separated by a layer of liquid respectively gas. Mixed friction is a mixed combination of the friction conditions, primary dry and lubricated friction. [6]

Basic friction mechanisms were adhesion, deformation (plastic), crenation, and hysteresis by elastic deformation. In a tribological system all processes are present, but there is often only one dominant.

To describe the friction condition in a tribological system, DIN 50 281 provides different friction parameters [14]:

- Friction resistance (friction force F_R, coefficient of friction μ (cf. Equ. (3.5)), friction moment M_R)
- Friction energy
- Friction power
- Contact temperature in the friction area

$$\mu = \frac{F_R}{F_N} \qquad \text{Equ. (3.5)}$$

3.1.6. Wear

According to DIN 50 320, wear is the progression removal of material from a surface in sliding or rolling contact against a counter surface. Almost all machines lose their durability and reliability due to wear and the possibilities of new advanced machines are reduced because of wear problems. Therefore, wear control has become a strong need for the advanced and reliable technology of the future. [4]

The physical and chemical processes in a wear act are called wear mechanisms. Some commonly wear mechanisms are depicted in Fig. 3.7.

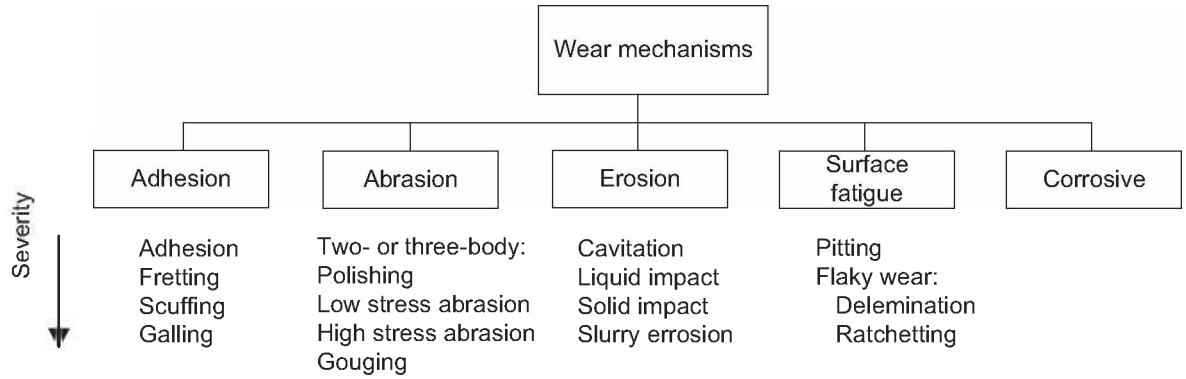

Fig. 3.7: A classification of wear processes

Adhesive wear occurs when two bodies slide over each other, or are pressed into one another, which promote material transfer between the two surfaces. A constant accumulation at one body is possible.

Abrasive wear occurs between surfaces of different relative hardness. In an abrasive wear mechanism, micro roughened regions and small asperities on the harder surface locally plow through the softer surface. The type of contact determines the mode of abrasive wear. Two body wear occurs when the grits are rigidly mounted or adhere to a surface, when they remove the material from the surface. Three-body wear occurs when the particles are not constrained, and are free to roll and slide down a surface

Erosive wear is the loss of material from a solid surface due to relative motion in contact with a gas or fluid that contingently contains solid particles.

Surface fatigue is a result of dynamic load on surfaces, which leads to initiation and propagation of cracks beneath the surface. As a consequence of this, wear parts break out from the loaded surface. With increasing friction the maximum of the effective stress move to the surface and with it the crack layer.

Corrosive wear occurs as a result of a chemical reaction on a wearing surface. The most common form of corrosion is due to a reaction between the metal and oxygen; however, other chemicals may also contribute. Corrosion products, usually oxides, have shear strengths different from those of the wearing surface metals from which they were formed. The oxides tend to flake away, resulting in the pitting of wearing surfaces. [21], [26]

3.1.7. Lubrication

High values of coefficient of friction in an engineering application would often lead to intolerably high friction forces and friction energy losses. For most practical uses, therefore, lubricants are used to reduce the frictional force between surfaces. In the most cases the lubricant is an oil or grease. The most important property of oil for lubrication purposes is its viscosity. Viscosity provides a measure of the resistance of a fluid to shearing flow. To improve the lubrication properties commonly additives were glazed. Basically lubrication oil is composed with base oil and additive packets. [14]

The functions of the lubricants are:

- Decrease friction and wear
- Reduce energy losses and operating temperature
- Cooling friction surfaces
- Protect from corrosion
- Cleaning friction surfaces
- Reduce acoustic level

3.2. Fretting

Fretting denotes a small oscillatory movement between two solid surfaces in contact. The direction of the motion is usually, but not necessarily, tangential to the surface. [21]

The general definition for fretting according to ASM Handbook: *"A special wear process that occurs at the contact area between two materials under load and subject to minute relative motion by vibration or some other force"*. [1]

Another contingency to define fretting is to arrange a barrier between fretting and reciprocating wear (cf. Fig. 3.8). Due to oscillatory sliding movement the contact size in the sliding direction ($2a$) and twice the sliding amplitude ($2\delta_0$) can be compared using the ratio $e=\delta_0/a$. The two cases of fretting, partial and gross slip (defined later), are situated in a domain with e<1 corresponding to a situation where a part of the wear scar of the flat is always in the contact. When the relative displacement between the contacting bodies is increasing the sliding region grows detriment of the sticking region. By further increasing of the relative displacement between the bodies the sticking fraction in the contact will be reduced to zero and the whole contact will slide. At a ratio $e>1$ the range is called reciprocating sliding wear, corresponds then to a situation where the entire wear scar is in the contact with the environment. [27], [9]

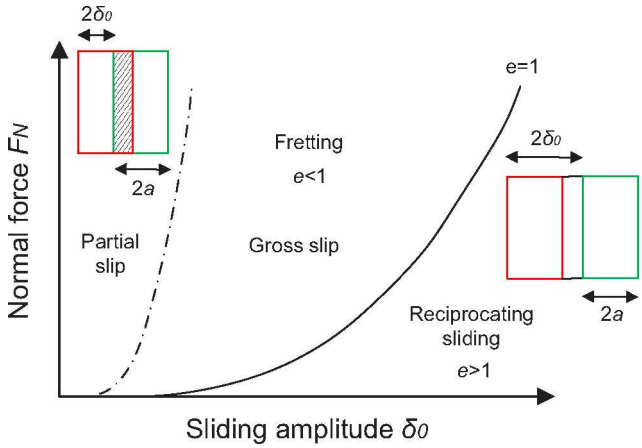

Fig. 3.8: Barrier between fretting and reciprocating sliding [27]

Fretting can be classified in fretting wear (FW), fretting fatigue (FF) and fretting corrosion (FC). These are the three commonly used terms to describe fretting processes.

Fretting wear occurs when surfaces of two bodies in contact make a small relative oscillatory displacement through an external force or vibrations. This damage often appears in tight fits. Does the relative oscillatory displacement in the contact surfaces occur through a cyclic load then we spoke about fretting fatigue (cf. Fig. 3.9). The damage with creation of oxidative wear particles is called fretting corrosion. Fretting corrosion can occur both in fretting fatigue and fretting wear. [27]

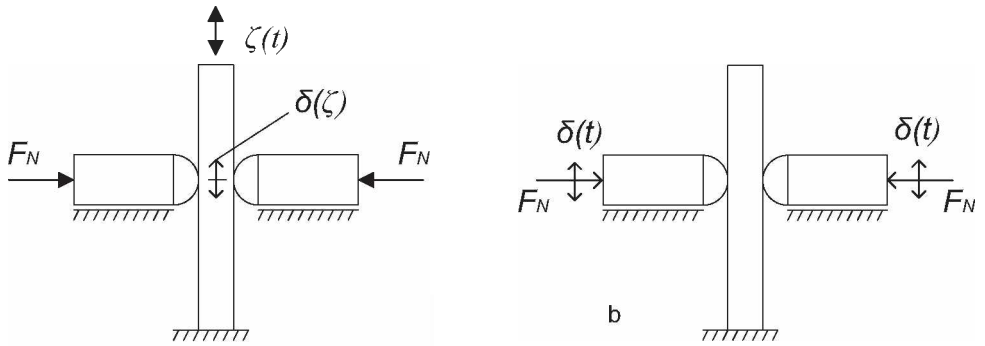

Fig. 3.9: Fretting fatigue (a), fretting wear (b)

In fact, two main types of damage can appear under both fretting wear and fretting fatigue conditions:

- Wear induced by fretting (WIF): this corresponds to classical material loss
- Cracking induced by fretting (CIF): cracks initiated on the surface can propagate up to the final failure of the specimen

Usually, the WIF damage is related to fretting wear and the CIF damage to fretting fatigue. Fretting wear and fretting fatigue are a loading of sliding materials due to sliding condition, while CIF and WIF are the consequences of the loading. Therefore it is commonly to keep the terms fretting wear, fretting fatigue and fretting corrosion to describe the loading and the terms WIF and CIF to describe the degradation. Following the two processes are described.

WIF is related to debris powder (red powder for steels, black powder for aluminium and titanium alloys). First WIF begins with the removal of superficial oxide layers and the increasing of the contact between the bodies through smoothing of the roughness. Then a new microstructure is formed called *"Tribological Transformed Structure"* (TTS) in the case of non-initially brittle materials. Through the high local stresses the material begins to form plastically and begins to harden. Hence the microstructure becomes brittle and broke by relative displacement. The metallic debris is then trapped, crushed and oxidized in the contact which induces the formation of a powder bed. A schematic cross-section of the contact in Fig. 3.10 shows the plastic deformed layer, the debris bed and the TTS. An example of the depth of the TTS versus the number of fretting cycles for titanium alloys is given in Fig. 3.11. [52]

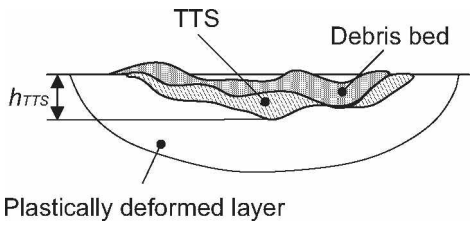

Fig. 3.10: Schematic view of a contact cross-section in the case of WIF [46]

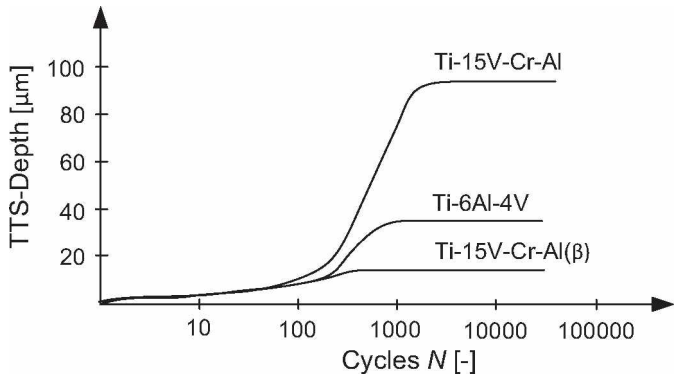

Fig. 3.11: Depth of the TTS versus the number of cycles for some titanium alloys [52]

The integration of particles as an additional tribological body tends to a three-body consideration of the tribological system (cf. Fig. 3.12). In the case of both fretting wear and fretting fatigue, a third-body approach is a basic need, since a particle must stay for a certain period in the interface before being ejected. [46]

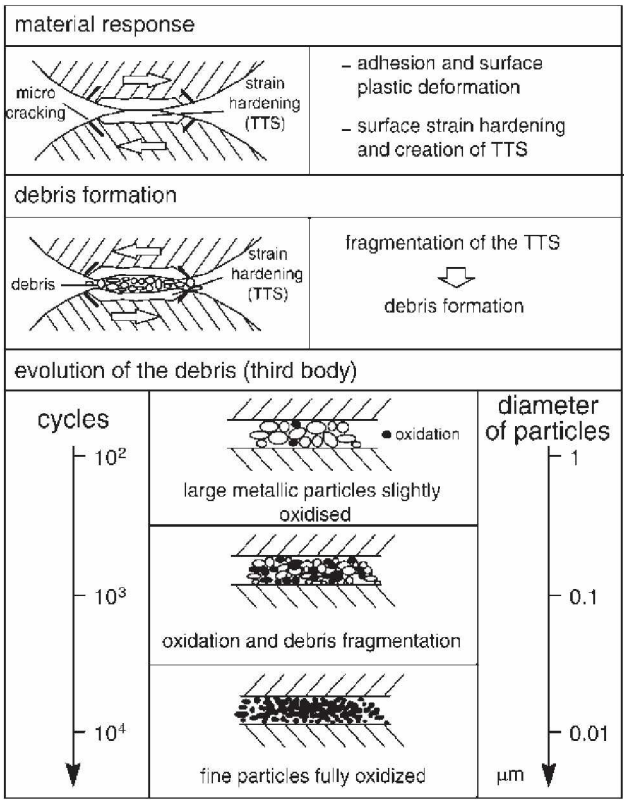

Fig. 3.12: Creation and evolution of the third body through the contact interface [46]

For CIF, several characteristic features are observed for the cracks forming on the contact surface:

- In some cases, few cracks nucleated on each side (as related to the friction movement) of the contact limit. Then on each side, a main crack develops which can lead to spalling.
- Cracks can also initiate and be distributed everywhere on the contact surface. Very often this induces the formation of coarse debris or spalls but usually only the mist external cracks propagate because of the compressive field beneath the surface.

Material loss and cracking sometimes appear as competitive processes: for instance, material loss can eliminate small superficial cracks or the opening of a deep crack can accommodate the main part of the imposed displacement and thus strongly reduce the slip amplitude and consequently the debris formation. Obviously the fretting processes appear to depend on very complex phenomena. Therefore, it appears very difficult to propose guidelines for the understanding of the material behavior and for the choice of material. [27], [46], [52]

For a better comprehension of the fretting process it is very important to understand the consequences of the loading in a fretting test. Through the different loading options there are different contact conditions in the contact area. Three different regimes of fretting are distinguished using dynamic tangential force and displacement measurements. The three regimes are:

- Stick regime
- Mixed stick and slip regime
- Gross slip regime

The stick regime is characterized by a very limited slide and surface damage. A tangential force versus displacement plot for a complete load cycle is a straight line. Only elastic deformation and no sliding losses occur. The mixed stick and slip regime contact surface is subdivided into a central stick area, surrounded by an annular yield and slip area. For soft materials, contact fatigue cracks are observed around the stick-slip boundary. The $F_T(\delta)$ curve displays a narrow hysteresis loop, indicating some plastic deformation and relaxation by sliding. The gross slip regime is recognized by a sudden drop in the recorded $F_T(\delta)$ curve, corresponding to a transition from static to kinetic friction. All adhesive asperity contact bridges are broken during every half –cycle and plastic deformation takes place in the bulk of the contact zone. The scars are characterized by sliding wear groove in the fretting direction. The $F_T(\delta)$ hysteresis loop is deformed by the incipient gross slip drop in F_T. The characteristic fretting loops for these three regimes are shown in Fig. 3.13. [53], [54]

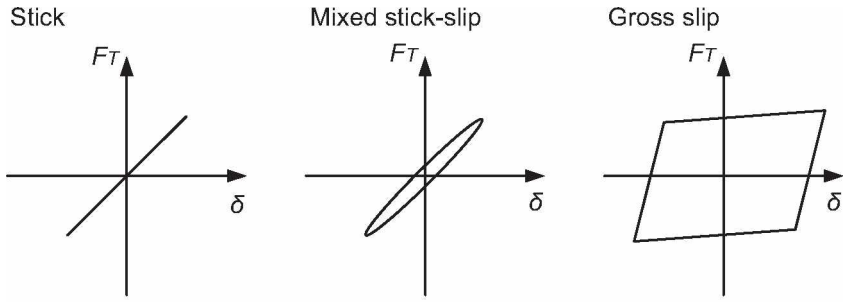

Fig. 3.13: Characteristic fretting loops [51]

Generally, there is a gradual transition from the stick regime to the mixed regime, whereas, the mixed-to-gross-slip transition is sharp. The mixed stick-slip regime is characterized by high cyclic surface stresses at the boundary between the stick zone and the slip annulus, promoting contact fatigue. Thus, conditions of mixed-stick slip will aggravate bulk fretting fatigue. Similarly, the sliding conditions of the gross slip regime are characteristic of fretting wear, during which surface fatigue cracks will be successively worn away. [54], [53]

In common, fretting hysteresis or fretting loops are used to evaluate the tangential force versus displacement characteristics. Additionally friction logs (3-D-graph, tangential force and imposed amplitude versus the number of cycles) are used to evaluate the fretting process. Third-body action or crack formations are illustrated using these friction logs.
Generally we can differentiate between closed, elliptical and trapezoidal cycles (cf. Fig. 3.13). *Closed cycles* (cc) characterize a non-dissipative process associated with purely elastic accommodation found in the stick zone. Machine and tangential contact stiffness is given by the slop of the line. *Elliptic cycles (ec)* characterize a slightly dissipative process und generated in contact in which partial slip is found or in cracked configuration with interfacial crack friction. Depending on operation conditions, the area of the ellipse varies in size. *Trapezoidal cycles (tc)* are characteristic of gross slip and characterize high dissipative processes. The horizontal segments exhibit the dissipative energy and the vertical segments the elastic displacement of the contact and of the test apparatus. [51]

As shown before in chapter 3.1.4 we can distinguish between incomplete and complete contact. We spoke about contacts where only a normal force was applied and without shear traction. In any fretting problems there are two fundamental features present. First, the contact must be experiencing shear traction and this normally means that a resultant tangential force is transmitted from one body to another. Secondly, there must be some degree of relative tangential displacement between the contacting surfaces so that slip takes place during cyclic variation of the applied load. [17]

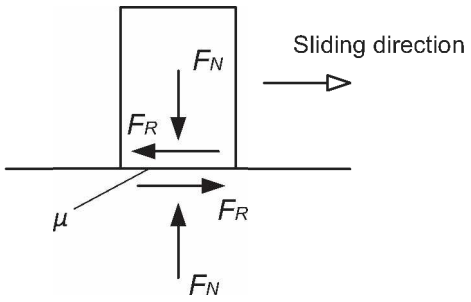

Fig. 3.14: Sliding between two rigid bodies [17]

Fig. 3.14 shows an illustration of sliding between two bodies. A friction force F_R occurs, proportional to the normal force F_N. Both forces are linked through the coefficient of friction μ (Equ. (3.6)).

$$F_R = \mu \cdot F_N \qquad \text{Equ. (3.6)}$$

In general, for the case of slipping the traction are related by the friction law, so that

$$|q(x,y)| = -\mu \cdot p(x,y) \qquad \text{Equ. (3.7)}$$

q(x,y) Shear stress
p(x,y) Pressure

For the case where there is no relative slip, the shear traction must be less than or equal to the limiting frictional value

$$|q(x,y)| \leq -\mu \cdot p(x,y) \qquad \text{Equ. (3.8)}$$

Equ. (3.7) and Equ. (3.8) give the usual interpretation of Coulomb friction employed in the analysis of elastic contacts where the friction law is taken to apply at each individual point within the contact rather than to a rigid body as a whole. It is possible to use this model to analyze elastic contacts where a shear force is applied which is less than the limiting frictional value.

Fig. 3.15 depicts the distribution of shear traction in a contact obtained for different values of $F_R/\mu \cdot F_N$. The central stick zone where the shear traction distributions are reduced in magnitude is immediately apparent. [17]

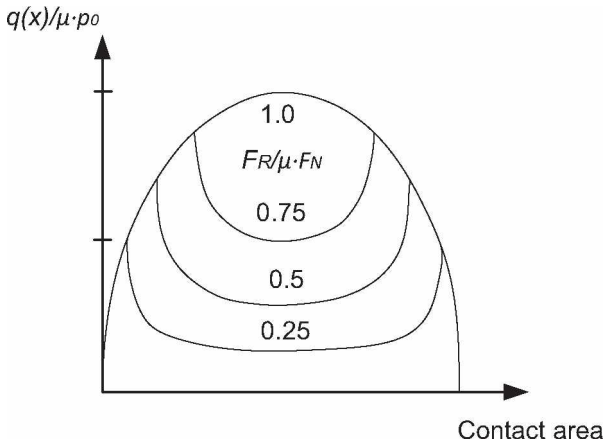

Fig. 3.15: Shear traction distribution in dependent to the tangential force [17]

For a detailed introduction to contact mechanics it is referred to the book "Mechanics of Fretting Fatigue", by D.A. Hills and D. Nowell [17].

3.2.1. Influencing variables of the fretting process

It was realized that fretting is a complex damage process with multiple states that are influenced by a large number of parameters. Dobromirski et al. [10] found that up to 50 variables might influence the fretting process. The parameters studied in research laboratories for fretting wear, fretting fatigue and fretting corrosion are:

- Contact pressure
- Tangential force
- Coefficient of friction
- External load
- Slip amplitude
- Contact area
- Frequency of vibration
- Number of cycles
- Temperature
- Surface roughness
- Hardness of contacting surfaces
- Thickness of oxide layers
- Ambient atmosphere
- Humidity
- Lubricants
- Residual stresses
- Work-hardening of surface
- Materials of contacting members
- Morphology of the materials
- Corrosion susceptibility
- Microstructure
- External load ratio
- Plain fatigue level
- Size effect
- Metallurgical compatibility

3.2.2. Fretting maps

One of the most important progresses is the development in fretting maps, which describe the overall behavior of fretting, such as contact conditions, fretting regime, wear mechanisms, crack nucleation and propagation. Normal contact load or contact pressure and displacement or relative slip, are important factors that control fretting wear and fretting fatigue. Most fretting maps constructed in the literature are two-dimensional diagrams in terms of these factors. The fretting maps are first established from Vingsbö et al. [54] to allow the comparing of different variables. Zhou and Vincent et al., [60]-[61], proposed independently two kinds of fretting maps:

- Running Conditions Fretting Maps (RCFM)
- Material Response Fretting Maps (MRFM)

The RCFM (Fig. 3.16 (a)) describes the process conditions including partial slip regime, mixed fretting regime (it is also called mixed stick and slip regime) and slip regime. The MRFM (Fig. 3.16 (b)) is divided into three domains, slight degradation or no degradation (ND), cracking (C) and wear (detachment particles, DP) domain. Concerning correspondence to the RCFM, slight degradation is mainly located in the partial slip regime, while wear with severe particle detachment occurs in the slip regime. The real contact area after test is similar in both partial slip regime and mixed fretting regime while it increases rapidly as a function of the number of cycles in the slip regime. Accompanying with severe cyclic plastic deformation, the mixed fretting regime was the most critical for crack nucleation and propagation. The formation of cracks was possible toward the stick-slip regimes at the higher number of cycles. [59], [54], [60], [36]

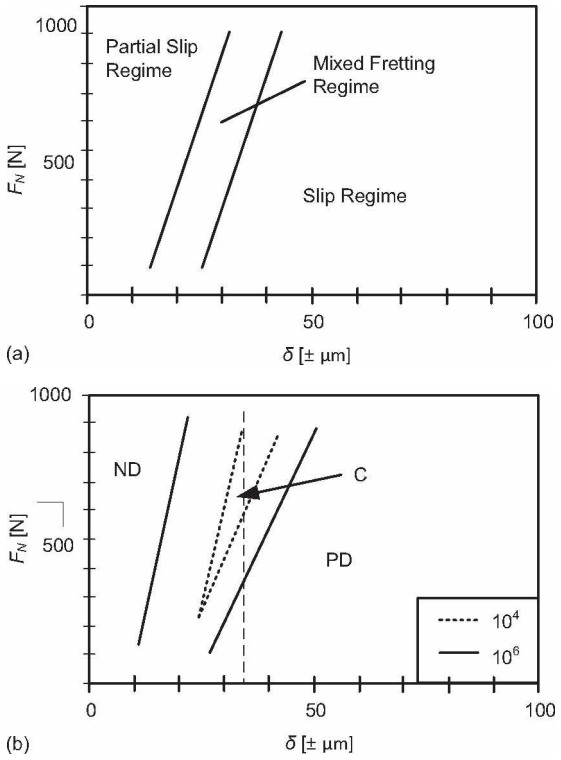

Fig. 3.16: Fretting maps in terms of normal force F_N vs. displacement amplitude δ: RCFM (a), MRFM (b) [59], [60]

Furthermore, it can be distinguished in fretting maps for fretting wear and fretting fatigue. The fretting maps shown in Fig. 3.16 belong to fretting wear. Based on running condition and material response fretting maps by Zhou and Vincent [60], [58], [61] and Petiot et al. [40] proposed fretting fatigue maps (Fig. 3.17) by varying normal load and maximum cyclic stress under fretting fatigue conditions.

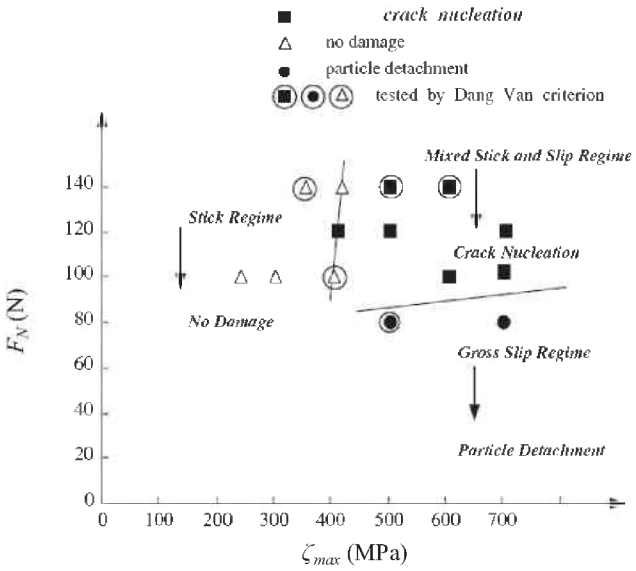

Fig. 3.17: Fretting fatigue map [59]

Nakazawa et al. [36] proposed fretting fatigue life maps in terms of contact pressure p and relative slip amplitude δ shown in Fig. 3.18, whereas the contour of fretting fatigue life instead of crack nucleation and propagation is clearly observed. The concavity represents the area where the life decreases extraordinarily, i.e., the crack nucleation and growth occur easily compared with other area. However, fretting regime and wear conditions are not noted in the fretting fatigue life map. [59]

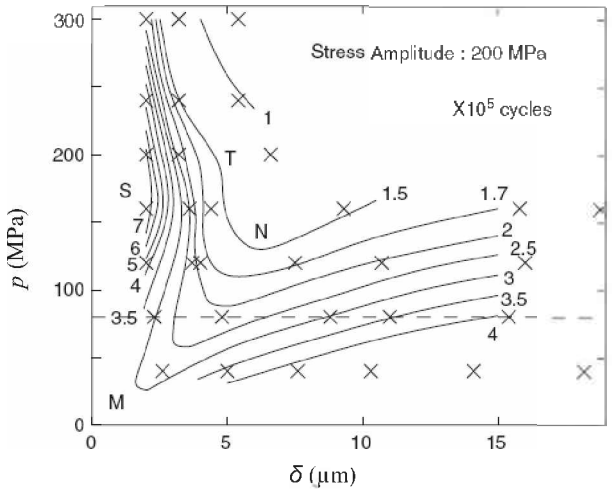

Fig. 3.18: Fretting fatigue life map [59]

A correlation between fretting wear and fretting fatigue is shown in Fig. 3.19, which shows a relationship between the number of cycles to crack nucleation N_i and displacement amplitude δ at a given normal load. [59]

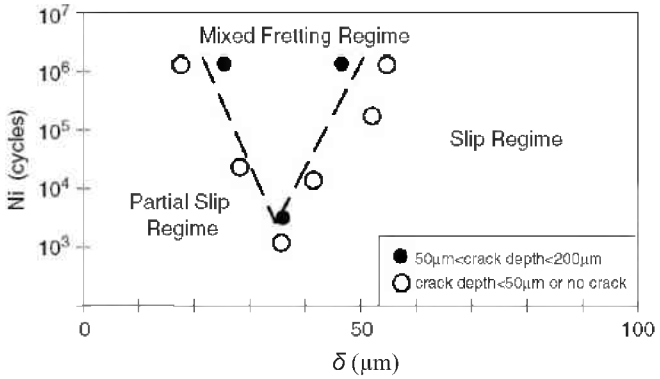

Fig. 3.19: Fretting wear life map [59]

3.2.3. Damage parameters

3.2.3.1. Fretting wear

The consequence of fretting wear is material loss; therefore it is meaningful to calculate the wear volume. The first model for calculation of the wear volume was developed by Archard [1]:

$$V_w = K_{Archard} \cdot P \cdot S \qquad \text{Equ. (3.9)}$$

V_w	Wear volume
$K_{Archard}$	Archard wear coefficient
P	Applied load
S	Sliding distance

Another alternative to calculate the wear volume was suggested by Fouvry et al. [12], [11]:

$$E_d = \sum_{1=1}^{N} E_{di} \qquad \text{Equ. (3.10)}$$

$$V_w = E_d \cdot K_{Energy} \qquad \text{Equ. (3.11)}$$

E_d	Dissipated friction energy for all cycles
K_{Energy}	Energy wear volume coefficient

For the use in finite element analysis, wear equations have to be adapted. In finite element analysis, wear needs to be computed at each contact node. The wear equation has to be applied locally by replacing the wear volume by a wear height and by using the contact pressure and sliding distance computed at the contact nodes. Maxian et al. [34], who computed the wear in a total hip replacement, applied the following formulation of the Archard equation at each contact node [9]:

$$h_{Wear} = K_{Archard} \cdot p \cdot s \qquad \text{Equ. (3.12)}$$

h_{Wear}	Wear depth
p	Local contact pressure
s	Local sliding distance

3.2.3.2. Fretting fatigue

- Ruiz Chen criterion

  Ruiz defined the Fretting Fatigue Damage Parameter (FFDP):

$$FFDP = \sigma_T \cdot \tau_R \cdot \delta \qquad \text{Equ. (3.13)}$$

ζ_T	Maximum tangential load (stress parallel to the surface)
η_R	Shear stress
δ	Slip amplitude at the surface

  The FFDP was formulated for the use on the dovetail joint of blade and disc in gas turbines, for the prediction of the fracture site. The maximum value of FFDP predicts the most probability location for the fracture site. It was established that no correlation between the lifetime and the FFDP is existed. Generally it can be said that the FFDP parameter is only for specific requirements adaptive. An example for successful utilization of the FFDP was shown by calculations with crimp connections related to bending. [9], [57]

- Smith-Watson-Topper parameter

  This criterion characterizes the form of a specific energy and is based on a physical background. The SWT parameter is composed of the maximum value of the stress component ζ_{max} perpendicular to a plane at any instant of an analyzed fretting cycle and $\Delta\varepsilon$, which is the difference between the maximum and minimum strain perpendicular to a plane, experienced during the cycle. With the aid of SWT parameter the determination of a critical plane will be realized. The highest calculated value of the SWT parameter determines the number of cycles to crack initiation and additionally the crack orientation in the critical plane. The parameter is used for materials where cracks initiate through a normal stress and grow practically from the beginning in mode I. [9], [57], [43]

$$SWT = \sigma_{max} \cdot \frac{\Delta \varepsilon}{2} \qquad \text{Equ. (3.14)}$$

- Shear stress range parameter

The shear stress rang (SSR) parameter describes a critical shear stress $\Delta\eta_{crit}$, whereas the maxima characterizes a critical plane where the crack initiation is expected. [37]

$$\Delta \tau_{crit} = \tau_{max} \cdot (1 - R_{\tau})^{m} \qquad \text{Equ. (3.15)}$$

R_η	Stress ratio for the considering plane
M	Fitting parameter
η_{max}	Maximum shear stress on the critical plane

- Fatemi-Socie parameter

The Fatemi and Socie criterion is focused on materials whose initiation and initial crack growth are produced by a growth process in mode II (shear stresses). As opposed to McDiarmid, it uses a range of shear strains instead of stresses. It also incorporates a term that reflects the opening of the crack, which is the normal maximum stress perpendicular to the plane of the maximum shear strain increments. The parameter is therefore [37]:

$$FS = \frac{\Delta \gamma_{max}}{2}\left(1 + k \frac{\sigma_{max}}{\sigma_y}\right) \qquad \text{Equ. (3.16)}$$

k	Material parameter (is fitted from the uniaxial and torsion fatigue tests data)
$\Delta\gamma_{max}$	Shear strain increment in the plane where it is maximum
ζ_{max}	Normal stress perpendicular to the plane where the maximum of $\Delta\gamma$ is produced
ζ_y	Yield strength

- Dang- Van criterion

$$\Delta \tau + \alpha p < \beta \qquad \text{Equ. (3.17)}$$

The $\Delta\eta$ is the shear stress range in the most unfavorably oriented plane, p is the hydrostatic pressure and α and β are material constants. When the inequality is fulfilled during the whole fretting cycle, then no fatigue, else fatigue is predicted. [9]

- McDiarmid criterion

This criterion was developed for multiaxial fatigue in cases where crack initiation is governed by shear stresses. It can be included within the group of the so-called "critical plane" criteria. In this criterion the critical plane is that in which the variation range of the shear stresses throughout one load cycle becomes maximum. Thus, the equivalent stress is defined at the point of initiation as:

$$\sigma_{eq} = \frac{\Delta\tau_{max}}{2} + \frac{t}{2\sigma_{uts}}\sigma_{max} \qquad \text{Equ. (3.18)}$$

$\Delta\eta_{max}$	Maximum shear stress range
t	Shear fatigue strength
ζ_{uts}	Ultimate tensile strength
ζ_{max}	Maximum normal stress in the direction perpendicular to the plane where $\Delta\eta$ is maximum

McDiarmid mentioned two shear fatigue limits, t_A and t_B, depending on whether the crack grows along the surface or towards the inside of the surface, respectively. Normally there is only one value for t, which will be the one to use. [6], [37]

- Crossland criterion

The Crossland criterion is different from the previous ones in the sense that it is no longer a critical plane criterion, but a global one, based on the values of an invariant of the stresses. While previous criteria require a maximum value among all directions projecting the stresses (or strains), in the Crossland criterion the calculation of stresses can be done in any direction, and it only requires the calculation of an invariant. This criterion has the obvious advantage of a much shorter computation time, with the inconvenience of the loss of a physical sense of the problem. The stress or equivalent stress parameter is [37]:

$$Cross = \sqrt{J_{2,a} + \frac{I_{1,max}}{3}}\left(\frac{3\tau_{sf}}{\sigma_{bf}} - \sqrt{3}\right) \qquad \text{Equ. (3.19)}$$

$J_{2,a}$	Amplitude of the second invariant of the deviatoric stress tensor
$I_{1,max}$	Maximum of the first invariant of the stress tensor
η_{sf}	Shear fatigue limit
ζ_{bf}	Bending fatigue limit

3.3. Fretting of Ti-6Al-4V

The fretting behavior of Ti-6Al-4V is influenced by several parameters, e.g., relative slip, bulk load, normal load, tangential load and temperature. Contact configurations, microstructure, environment and surface conditions have also essential effects on the fretting behavior. Difficulties are encountered while it is not easy to find a direct relation between a single parameter and fretting damage, because fretting is a complex damage process with multiple states that are influenced by a large number of parameters as mentioned before. The influence of important parameters on the fretting behavior of Ti-6Al-4V, are discussed below.

3.3.1. Influence of the contact configuration

Jin and Mall [24] conducted fretting fatigue tests using cylindrical pads and flat pads with rounded edges (Fig. 3.20) at various applied pad displacements and at two normal forces on the pad under a constant bulk stress amplitude condition. All fretting fatigue tests were conducted at a stress amplitude between 266 MPa and 550 MPa (stress ratio of 0.03), normal forces (P) of 1334 or 4000 N and frequency of 2 Hz.

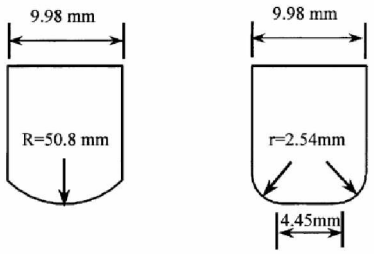

Fig. 3.20: Schematic drawing of different pad configurations [24]

They found that the evolution of tangential force is independent of the contact configuration at a given normal force (cf. Fig. 3.21). The ratio of the tangential force to normal force increases and stabilizes to a certain value with increasing applied pad displacement. They determined that the minimum fretting fatigue life occurred at relative slip ranges between 50 and 60 µm and it was independent of both contact configuration and applied normal force. The final increase in the fretting life resulted from gross slip. In the gross slip condition, fretting wear dominated during the fretting process and did not result in failure (Fig. 3.22).

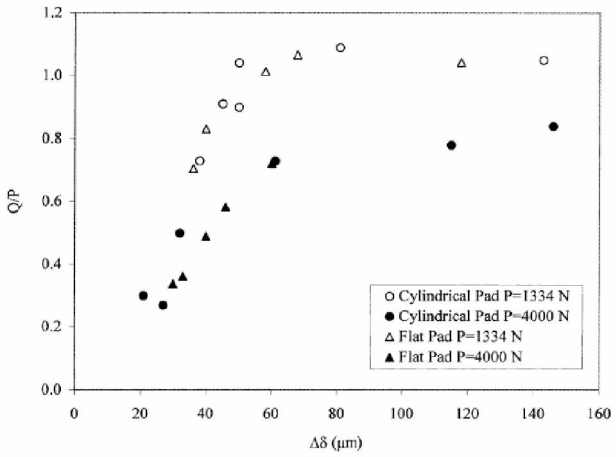

Fig. 3.21: Relative tangential force (Q/P) vs. $\Delta\delta$ for both cylinder-on-flat and flat-on-flat contact configuration at P = 1334 N and 4000 N [24]

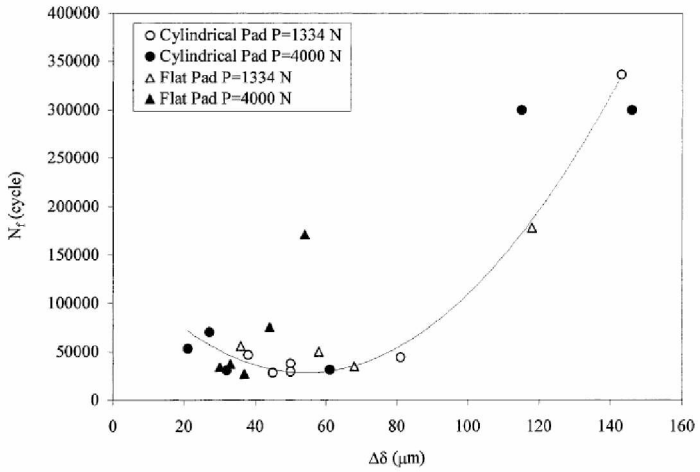

Fig. 3.22: Failure cycle N_f vs. relative slip $\Delta\delta$ range for both cylinder-on-flat and flat-on-flat contact configuration at P = 1334 N and 4000 N [24]

They also explained that the fretted surface profile was affected by the contact configuration. In the case of the cylinder-on-flat contact, the material was removed from the specimen under stick-slip conditions. The surface roughness increased with the relative slip range. Under gross slip, the material was transferred from the pad and deposited on the specimen. The most severe damage was observed at the trailing edge where the specimen failure occurred. For flat-on-flat contact configuration the material removal did not occur in the flat portion of the fretted region and was concentrated at the edges.

3.3.2. Influence of relative slip

Lee and Mall [29] investigated fretting fatigue behavior of unpeened and shot-peened Ti-6Al-4V using a dual-actuator test setup which was capable of applying an independent pad displacement while maintaining a constant cyclic load on the specimen. The fretting regime changed from stick to partial slip and then to gross slip with increasing relative slip range, and the transition from partial to gross slip occurred at a relative slip range of 50-60 μm regardless of the applied cyclic load, surface treatment, contact load and contact geometry (cf. Fig. 3.23).

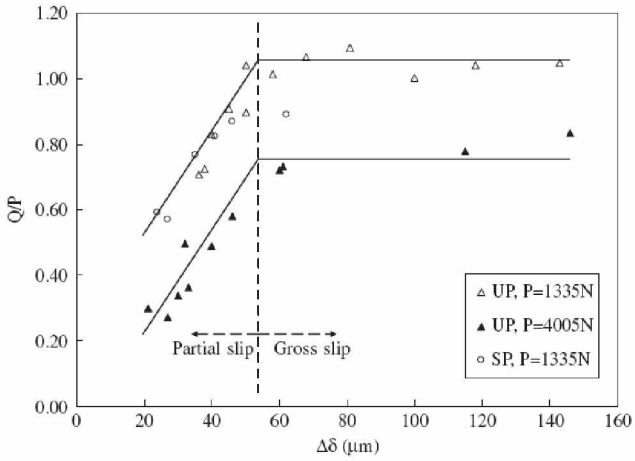

Fig. 3.23: Normalized tangential force (Q/P) versus relative slip range $\Delta\delta$ [29]

The fretting fatigue life initially decreased as the relative slip range increased and reached a minimum value, and then increased with increase of the relative slip range due to the transition in fretting regime from partial slip to gross slip. Shot-peened specimens had longer fatigue lifes than unpeened specimens at a given relative slip range, but the minimum fatigue life was found to be at the same value of relative slip range for both shot-peened and unpeened specimens (cf. Fig. 3.24). Tangential force was directly related to relative slip and this relationship was independent of other fretting variables.

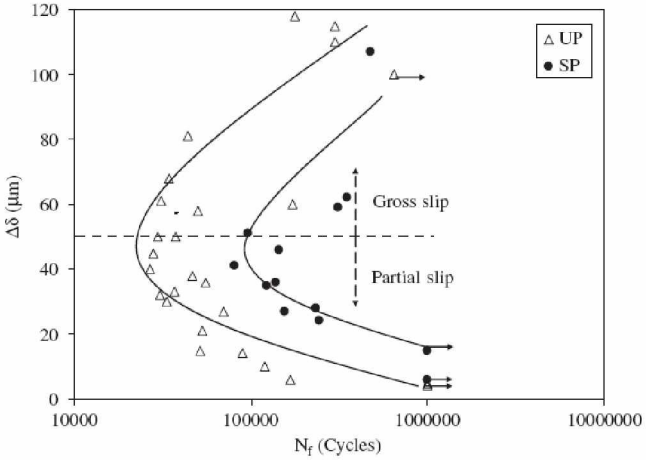

Fig. 3.24: Relative slip range versus fretting fatigue life [29]

Conner et al. [8] point out that both wear, which is related to slip, and state of stress play a role in crack development. Fretting fatigue produces wear debris that can enter cracks a few microns in length and cause crack closure in very small cracks in Ti-6Al-4V. While wear debris interact with cracks, the depth of wear or appearance of wear is a poor indicator of fretting fatigue life.
The overall contact mechanic in fretting fatigue are elastic, although localized plasticity is present. The plasticity results in wear damage at the surface and near-surface ratcheting. Micro-notches form in the wear region with lengths as small as 1 μm and root radii as small as 0.5 μm (cf. Fig. 3.25). These features, seen mainly on specimens that were shot-peened prior to testing, become crack initiation sites and contribute to further wear damage through the development of small cracks that propagate until surface material is removed.

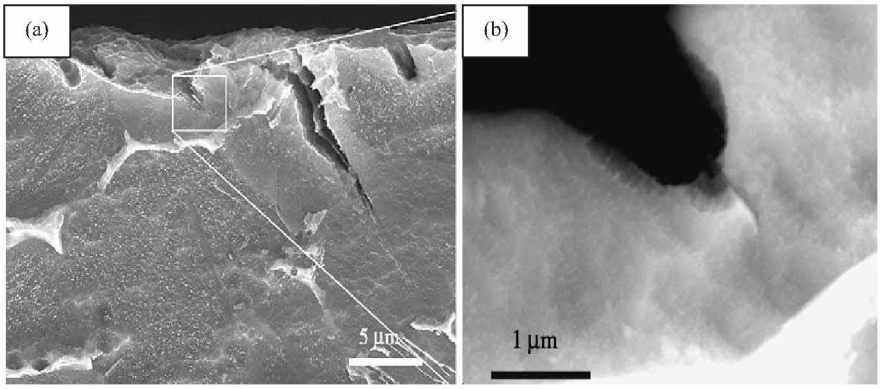

Fig. 3.25: SEM image of surface damage showing (a) delimination and the formation of small notches developing into cracks, (b) small crack (0.5 μm) growing out of a notch [8]

3.3.3. Influence of the bulk load

Venkantesh et al. [50] asserted in their experiments with varying bulk stresses (while all other parameters are kept constant), that the critical length at the transition from stage I to stage II growth and the life in the stage II are effectively reduced by fretting, resulting in a decreased total fretting fatigue life. Four sets of experiments were performed on mill-annealed material (cf. Fig. 3.26).

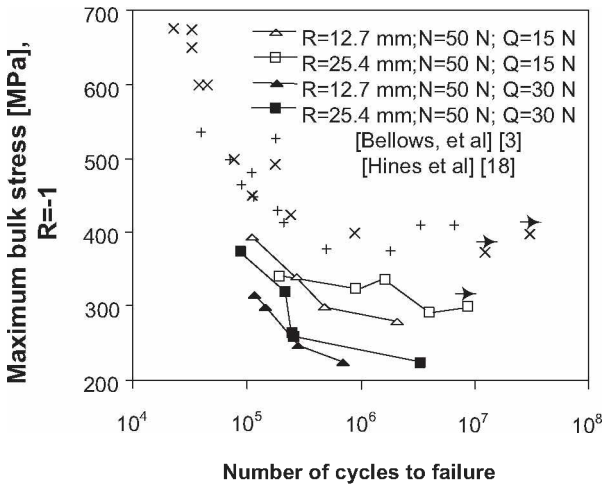

Fig. 3.26: Fretting fatigue results on mill-annealed Ti-6Al-4V (Uniaxial fatigue results cf. [39] and [40]) [50]

3.3.4. Influence of the normal load

Venkantesh et al. [50] conducted two sets of experiments on mill-annealed Ti-6Al-4V, where for each set the tangential load, the bulk stress and the fretting pad radius were maintained constant while the normal load was varied, as shown in Fig. 3.27. The total life to failure of the fretted materials increased as the normal load decreased. The increase in life is large for the experiments with larger pad radius. Nakazawa [35] too observed for Ti-6Al-4V that the fretting fatigue life decreases with the increase of contact pressure.

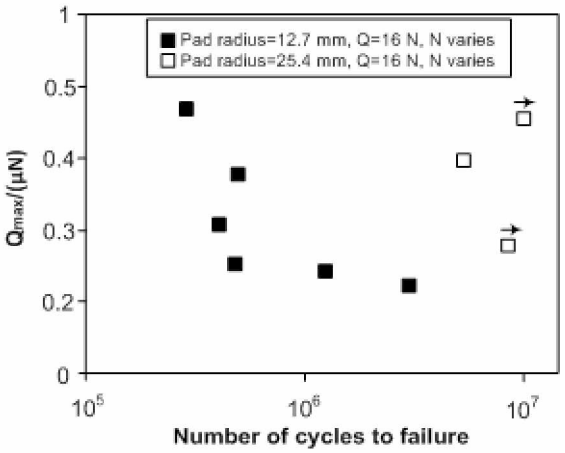

Fig. 3.27: Influence of the normal load *N* on mill-annealed Ti-6Al-4V [50]

Iyer [23] identified a linear relation between peak contact pressure p_0 in a Hertz cylindrical contact and fretting fatigue life (cf. Fig. 3.28). With higher peak pressure the life increases.

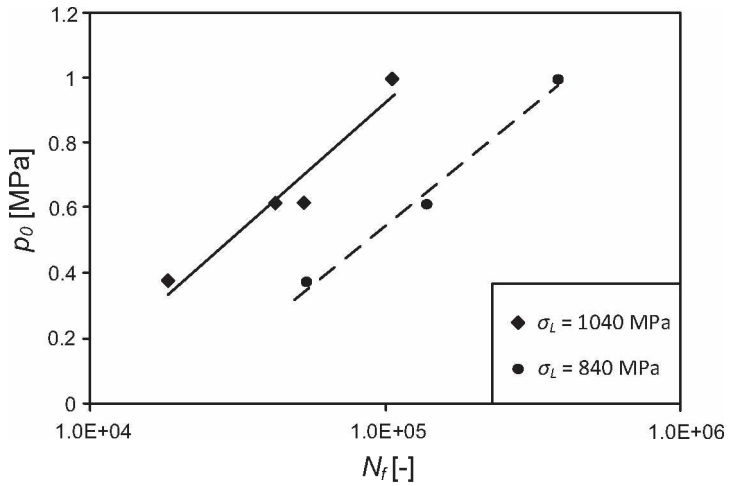

Fig. 3.28: Liner Fretting fatigue life N_f versus peak contact pressure, for two bulk stresses ζ_L [23]

3.3.5. Influence of the tangential load

Venkantesh et al. [50] showed that by varying of the tangential load, total life to failure of the fretted material is reduced as the tangential load increases (cf. Fig. 3.29). The reduction of life increases with lower radius.

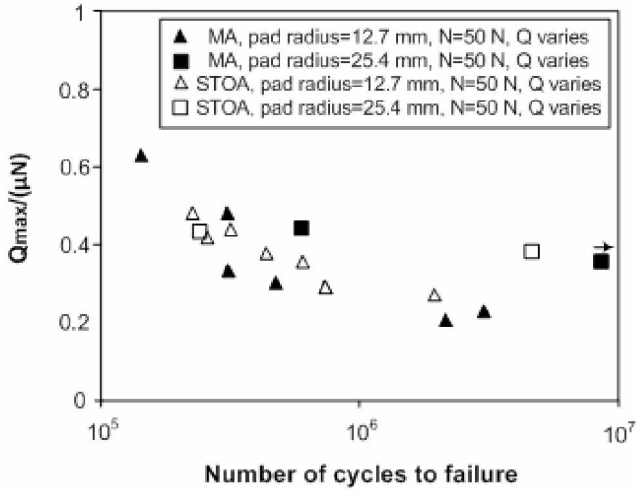

Fig. 3.29: Influence of tangential load on mill-annealed (MA) and solution treated and over-aged (STOA) Ti-6Al-4V [50]

3.3.6. Influence of temperature

Jin et al. [25] investigated the fretting fatigue behavior of Ti-6Al-4V at elevated temperature of 260°C. He found that the reduction in fatigue life and fatigue strength due to fretting from their counterparts in plain fatigue as significant at 260°C as well as at room temperature (cf. Fig. 3.30). However, there was practically no difference between room temperature and 260°C life data either in the plain fatigue or fretting fatigue condition (cf. Fig. 3.31).

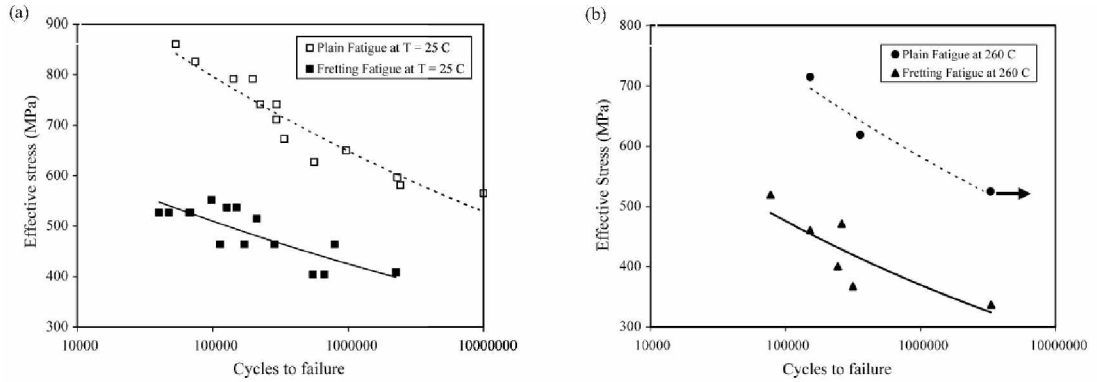

Fig. 3.30: Comparison between plain and fretting fatigue data: (a) room temperature; (b) 260°C [**25**]

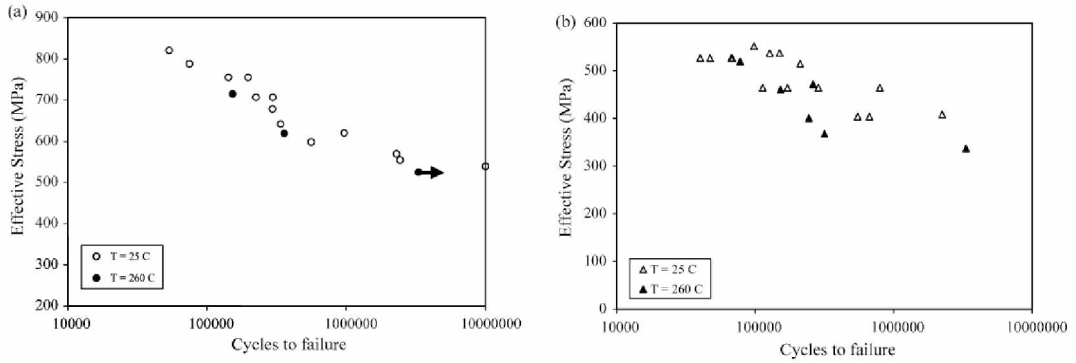

Fig. 3.31: Comparison of S/N relationship between room temperature and 260°C: (a) plain fatigue (b) fretting fatigue [25]

They reported that the value of the coefficient of friction at 260°C and its variation with cycling was similar to those at room temperature, as shown in Fig. 3.32. They assumed that this is due to the fact that the glaze oxide layer does not form on the Ti-6Al-4V surface at 260°C.

Furthermore, a critical plane model, modified shear stress range parameter was found to be effective to correlate the lives from the fretting and plain fatigue at both room and elevated temperature. It predicts also the location of fretting fatigue crack initiation and its orientation, which are in agreement with their experimental counterparts.

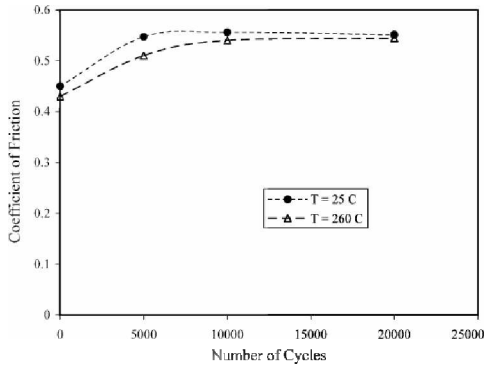

Fig. 3.32: Change in static coefficient of friction with increasing fretting cycles at room temperature and 260°C [**25**]

Lee et al. [28] found that fretting fatigue live of shot-peened Ti-6Al-4V decreases at elevated temperature of 260°C compared to room temperature. Residual stress measurements before and after fretting tests showed that the residual compressive stress was relaxed during fretting fatigue and elevated temperature fostered more stress relaxation.

3.3.7. Influence of microstructure

Mall et al. [33] investigated the fretting fatigue crack initiation and its dependence on the microstructure of Ti-6Al-4V, which is ranged from homogeneous duplex to transformed lamellar. All fretting fatigue tests were conducted at a cyclic frequency of 200 Hz, constant normal contact load with a Hertzian peak pressure of 304 MPa, with constant amplitude over a range of axial stress levels from 200 to 700 MPa and with stress ratios ranging from a nominal value of 0.0 to 0.7 under the displacement controlled mode. They observed that the resistance to crack initiation decreases with the change in microstructure from homogenous duplex to heterogeneous lamellar (cf. Fig. 3.33).

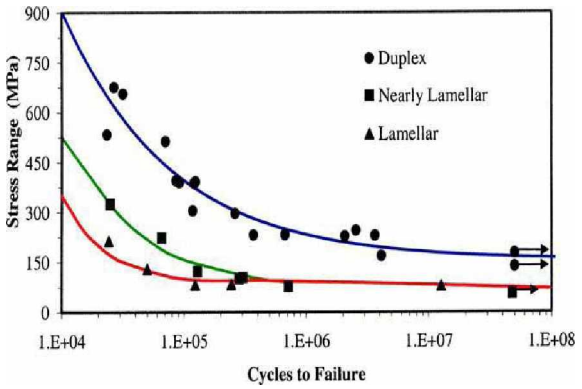

Fig. 3.33: S/N curve for a duplex, nearly lamellar and lamellar Ti-6Al-4V microstructure [33]

To account the effect of the mean stress or stress ratio they used the effective stress proposed by Walker [55], Equ. (3.20). Thereby, $\zeta_{effective}$ is the effective stress taking into account the stress ratio effect, ζ_{max} is the maximum applied stress on the specimen, R is the stress ratio and m is a fitting parameter which was determined to be 0.45. Fig. 3.34 shows fretting fatigue life diagrams for all three microstructures on the basis of this effective stress.

$$\sigma_{effective} = \sigma_{max} \cdot (1 - R)^m \qquad \text{Equ. (3.20)}$$

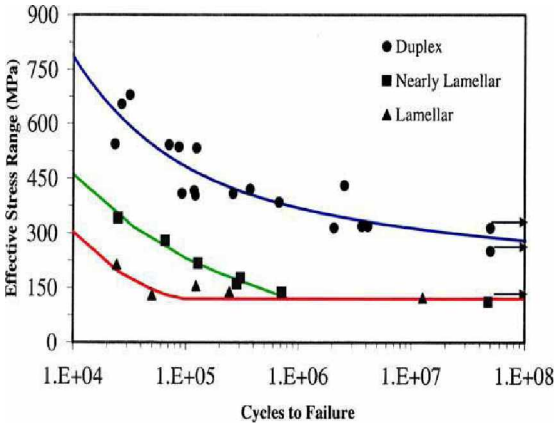

Fig. 3.34: S/N curve based on effective stress range [33]

Venkatesh et al. [50] investigated the effects of microstructures on the fretting fatigue behaviour of Ti-6Al-4V using a sphere-on-flat contact configuration. The initial solution-treated and overaged (STOA) microstructure was modified to coarse grained STOA, martensitic, acicular and lamellar/Widmanstatten microstructures through different heat treatment processes. The experiments showed that the microstructure does not have an appreciable influence on fretting fatigue life, see Fig. 3.35. However, the martensitic microstructure appeared to have better fretting resistance. It was mentioned that this enhanced fretting resistance may be related to the higher yield strength and hardness observed in the martensitic microstructure.

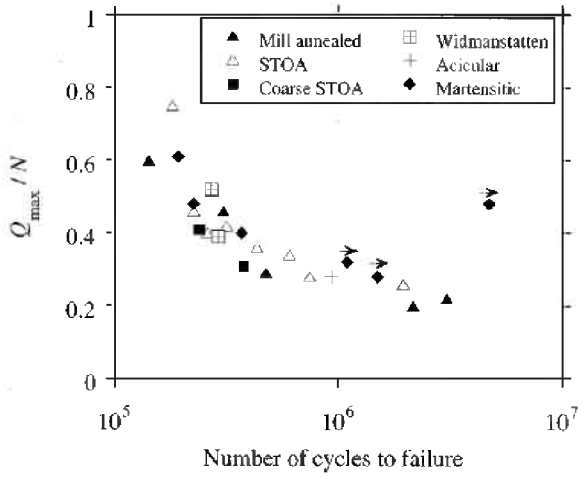

Fig. 3.35: Fretting fatigue results of different microstructures of Ti-6Al-4V [50]

Shaffer and Glaeser [47] reported that annealed materials were found to be less susceptible to fretting fatigue than in their work-hardened state. Similarly, cast structures were less susceptible than forged structures. The authors also mentioned that for three (α+β)-titanium microstructures, the finer or acicular microstructure was found to be more resistant to damage than the coarser annealed structure.

3.3.8. Influence of various surface conditions

Hutson et al. [22] analyzed the fretting fatigue behavior of Ti-6Al-4V specimens in contact with varying pad surface conditions. To characterize fretting fatigue behavior as a function of contact material and surface roughness, a test matrix was developed to incorporate Cu-Ni plasma spray coated pads and bare Ti-6Al-4V pads over a range of contact pad roughness. The Cu–Ni coating was deposited on as-received Ti–6Al–4V pads via a plasma spray process representative of that used in real hardware. Some uncoated Ti–6Al–4V pads were modified from the as-received condition to achieve a smoother surface through metallographic mechanical polishing. Additional pads were modified to achieve a rougher surface through grit blasting and subsequent stress relief annealing. The rougher surface was intended to simulate the roughness of the Cu–Ni coated pads to determine if previously observed changes in fretting fatigue behavior were a result of the coating or of the rougher surface. The behavior against all four pad conditions was evaluated with S/N fatigue tests.
An increase in fretting fatigue strength of 20 to 25% was observed for specimens tested against Cu–Ni coated pads as compared to those tested against as-received pads. The experimental results from the S/N tests indicated that surface roughness of the coated pads was primarily responsible for the increased fretting fatigue capability.

Rajasekaran and Raman [41] reported that plasma nitriding treatment enhanced the fretting fatigue lives of Ti-6Al-4V. This was attributed to the beneficial influence of lower friction force, higher surface hardness and higher surface compressive residual stress exhibited by the nitrided specimens.

Ren et al. [44] investigated four coating systems: TiCN, CrN+MoS_2, Cu-Al and Ag+ irradiated layer, which were evaluated for their potential towards improving fretting fatigue behavior of Ti-6Al-4V. They determined that the CrN+MoS_2, Cu-Al and Ag+ irradiated coating reduced the COF compared to the uncoated Ti-6Al-4V, while the TiCN coating did not vary the COF. The TiCN and CrN+MoS2 coatings could not improve the fretting fatigue life, because they were almost destroyed by a single friction slip. The Cu-Al coating exhibited relative better wear resistance.

Golden et al. [15] investigated in his work the performance of several coatings and surface treatments subjected to fretting fatigue with Ti-6Al-4V specimens and pads. Several hard coatings were considered in this study of fretting fatigue performance. These included two diamond-like-carbon (DLC) coatings, plasma sprayed Mo, electroless Ni–B, and a nitriding process. Additionally, two coatings, DLC and Mo, were chosen for testing along with two advanced surface treatment processes, laser shock processing (LSP) and low plasticity burnishing (LPB). Only one surface treatment performed significantly worse than the baseline for the coating evaluations. The nitrided specimen had significantly reduced fretting fatigue strength. The thicker coatings, Mo and Ni–B, both had nominally the same performance as baseline tests in both plain fatigue and fretting fatigue. These could be very good coating choices if the fretting fatigue application has other design factors such as wear resistance. Finally, the DLC coatings showed no decrease in plain fatigue properties, but a significant improvement in fretting fatigue performance which was likely due to a reduction in coefficient of friction μ throughout the test. The addition of LSP and LPB to the dovetail specimens with no coatings greatly improved fretting fatigue strength as expected. The addition of DLC to the LSP or LPB treated specimens resulted in no loss of performance, but no judgment can be made about additional benefit since results were inconclusive since all of these tests were run-outs.

Shepard et al. [48] asserted in their study the benefits of shot peening and particularly low plasticity burnishing on Ti-6Al-4V specimens in a fretting fatigue environment. While both surface treatments provided a clear benefit over the baseline condition, the performance of LPB treated specimens was superior. This is attributed to the enhanced surface finish and the deeper, more thermally stable compressive residual stresses associated with the LPB treated specimen.

Fu et al. [13] investigated the improvement of fretting wear and fretting fatigue resistance of Ti-6Al-4V by using several types of surface treatments and thin films, including shot-peening, ion-beam-enhanced deposition (IBED) CrN films, shot-peening + IBED CrN films as well as IBED CuNiIn films. Results showed that with the application of all the above surface coatings and treatments, the fretting wear and fretting fatigue resistance of Ti–6Al–4V were improved (cf. Fig. 3.36). However, the mechanisms and effects of several surface modification methods to mitigate the fretting damage were quite different. IBED CrN film exhibited the best fretting fatigue performance while the duplex treatment by shot-peening/IBED CrN film exhibited the highest fretting wear resistance. There are four mechanisms which can be used to explain the different fretting performance of these surface treatments and coatings: (1) to induce a compressive residual stress; (2) to decrease the coefficient of friction; (3) to increase the hardness; (4) to increase the surface roughness.

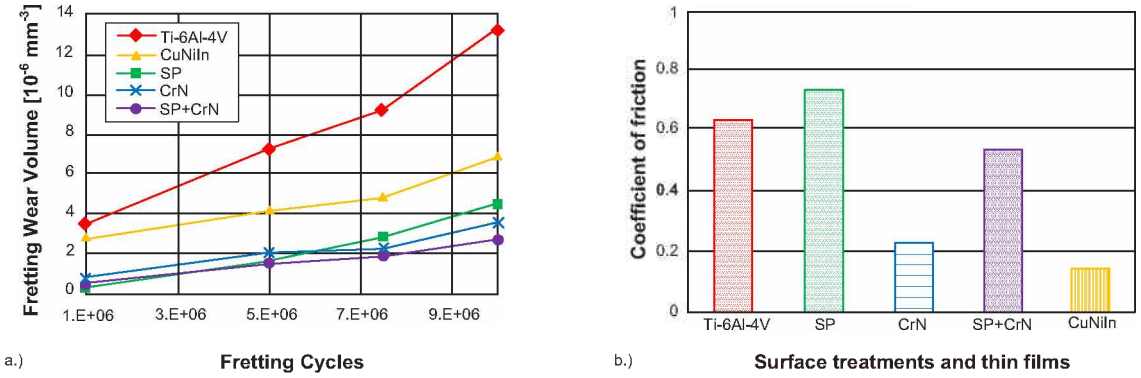

Fig. 3.36: (a) Fretting wear and (b) fretting fatigue resistance of Ti-6Al-4V with various surface conditions [13]

3.3.9. Influence of environment

Wharton and Waterhouse [56] determined longer fretting fatigue lives in low-cycle high stress fatigue but lower fretting fatigue strengths in high-cycle low stress fatigue in non-corrosive (dry argon) as compared to corrosive (humid argon) atmosphere, as shown in Fig. 3.37. The increase in fatigue strength was attributed to the protective influence of corrosion products. Thick layers of corrosion product formed within the fretted region in humid argon giving some protection to the surface and rendering the generation of fatigue cracks by fretting less likely, resulting in higher fatigue strengths at high cycle lives. At higher stresses and short lives the corrosion atmosphere were regarded as having a significant effect on crack propagation rates with a consequent reduction in fatigue life. It was noted that results in air were included and were seen to fit within the non-corrosive regime.

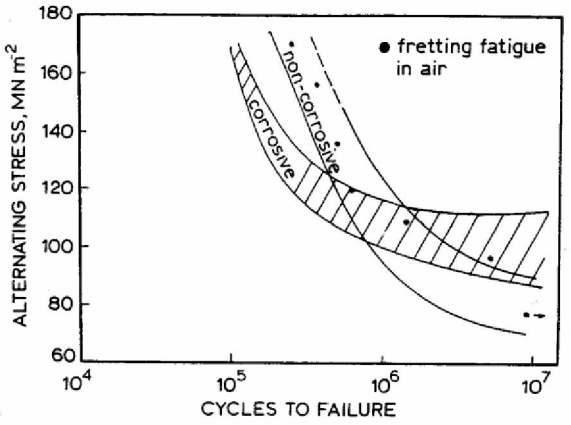

Fig. 3.37: Effect of corrosive and non-corrosive atmosphere on fretting fatigue of Ti-6Al-4V [56]

Lee et al. [31] investigated the fretting fatigue behaviour of shot-peened Ti-6Al-4V under seawater environment and asserts that seawater reduces the fretting fatigue life of shot-peened Ti-6Al-4V in both high and low cycle fatigue regimes relative to their counterparts in ambient laboratory condition (cf. Fig. 3.38). Shot-peening increased the fretting fatigue life of Ti–6Al–4V when tested under the laboratory and seawater conditions relative to their respective counterparts from unpeened Ti–6Al–4V. On the other hand, the unpeened specimen showed a slightly improved fatigue life in high cycle fatigue regime than that in ambient laboratory fretting condition, while the seawater fretting fatigue condition reduced the life in the low cycle fatigue regime. This different behavior between unpeened and shot-peened specimens can be attributed to the relative effects from the corrosive seawater environment and residual compressive stresses from shot-peening on the crack initiation behavior. Further, the seawater environment enhanced the crack propagation rate relative to that in the laboratory condition in both unpeened and shot-peened specimens. In addition, seawater may have indirectly beneficial effect on the fretting fatigue life through the excessive debris generation which may provide shielding effect on micro-crack generation during crack nucleation phase.

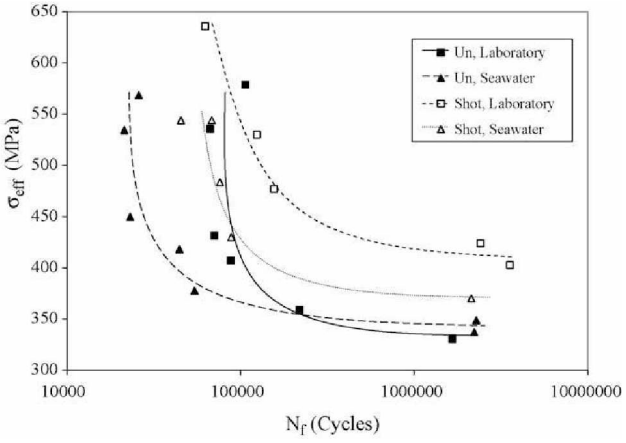

Fig. 3.38: Shot-peened and unpeened specimens under ambient laboratory and seawater environments [31]

3.3.10. Residual stresses

Lee et al. [30] investigated the behavior of residual stresses in a stress-free titanium alloy Ti-6Al-4V under fretting fatigue loading conditions. Compressive residual stress developed in the contact region due to the local plastic deformation between contacting bodies. They assumed that the compressive residual stress increased initially with increasing number of fretting fatigue cycles reaching to a maximum value and then it relaxed with further cycling (cf. Fig. 3.39). This relaxation of compressive residual stress was due to the delamination and detachment of flake-like (wear sheet) material in the fretted region.

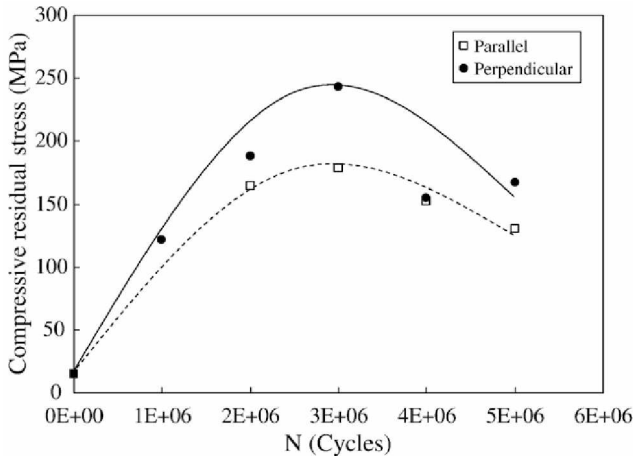

Fig. 3.39: Evolution of stress along the parallel and perpendicular directions to the loading direction during fretting fatigue [30]

3.4. Fretting life estimation

3.4.1. Fretting fatigue life assessment

Navarro et al. [37] analyzed the influence of different multiaxial fatigue criteria on life assessment in fretting fatigue conditions. The materials that were used for analysis are aluminum and titanium alloys, and the geometries were spherical and cylindrical contacts (cf. Tab. 3.1). A number of methods were used to predict initiation and total life. These methods can be divided into two groups; (i) those that take only crack initiation criteria into account when assessing total life, and evaluate stress on the surface or near it, (ii) those that combine crack initiation and propagation. This second group can in turn be divided into two subgroups. On one hand there are the models that consider propagation to begin at a previously fixed length. On the other hand, there exist models where it is considered that this length is not previously fixed. Four aspects were analyzed with these models: the influence on estimating life when using the value of stresses and strain either in a critical dimension or on the surface; the effect of the initiation length considered over the life obtained; the importance of one phase versus the other; and the influence of the multi-axial criterion employed.

Material:	G1 7075 T6	G2 7075 T651	G3 Ti6Al4V	G4 Al4%Cu	G5 2024 T351
Geometry:	Spherical	Spherical	Spherical	Cylindrical	Cylindrical

Tab. 3.1: Materials used for analysis [37]

Fig. 3.40 shows the results of the total life estimation obtained with the model that combines initiation plus propagation with variable initiation length for spherical contact. Fatemi-Socie criterion gives the same results as McDiarmid and with SWT criterion the estimated lives lie between the ones obtained with McDiarmid and Crossland. In any cases, in general, it can be said that Crossland and SWT produced better average results than McDiarmid and Fatemi-Socie.

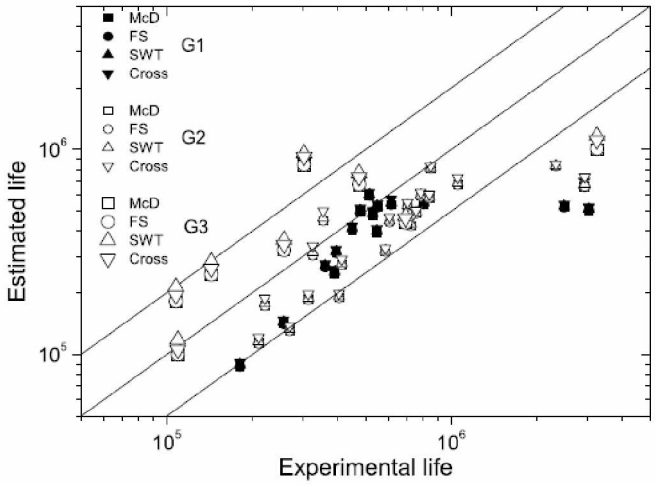

Fig. 3.40: Life estimations with spherical contact [37]

Chambon and Journet [7] investigated the use of fracture mechanics as an alternative to stress-based fatigue criteria by using the "crack analogue" concept to deal with crack initiation in a fracture mechanics framework. A very simple model, based entirely on independently derived parameters is shown to be able to capture the qualitative effects of the normal and tangential loads of fretting fatigue performance. The accuracy of the total life prediction is also satisfactory.
The comparison between the experimental and predicted curves is presented in Fig. 3.42, for the case with fixed normal load and fixed tangential load, respectively. The number of cycles for the first three stages (cf. Fig. 3.41) is split. Stage I is negligibly short (about 1 to 2% of the total life), while stage II represents the major part (approximately 70%) of the total life, regardless to the relative of Q/P.

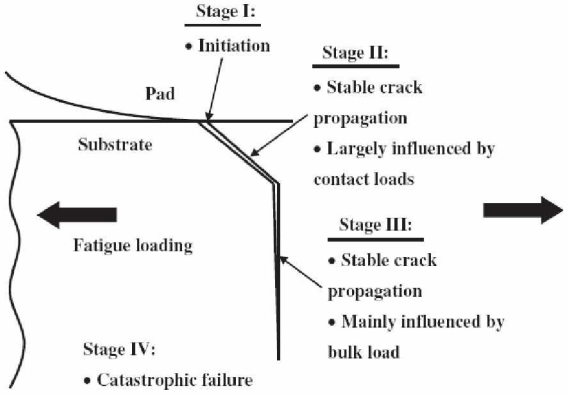

Fig. 3.41: Shematic representation of the different stages of fretting fatigue crack propagation [7]

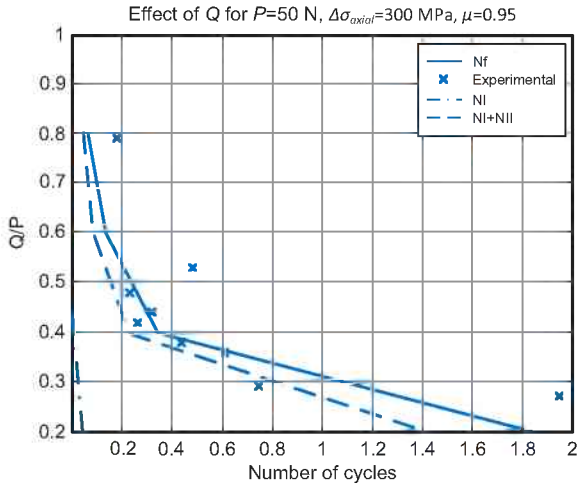

Fig. 3.42: Number of cycles to failure as a function of the tangential to normal load ration [7]

3.4.2. Fretting wear damage estimation

A quantitative approach of Ti-6Al-4V fretting damage was done by Fouvry et al. [12], [11]. They investigated the fretting behavior in a plain cylinder/plane contact configuration under ambient conditions and specified a quantitative methodology to formalize the friction, crack nucleation and wear behavior of Ti-6Al-4V under fretting loading.

The sliding condition was analyzed by observing the fretting loops, which are recorded during the fretting wear test. The sliding transition from partial to gross slip was identified from an energy discontinuity of the contact. Extending this approach, the running condition fretting map was defined.
The sliding transition is associated to a maximum friction coefficient μ_t and can be formalized by applying a pressure dependence formulation. This pressure dependence suggested that the friction law near the sliding transition is partly controlled by adhesion and metal transfer phenomena.
The friction behavior under gross slip conditions was formulated through an energy approach. Controlled by titanium oxide third body, it displays a constant value independent of the pressure field.
The schematic illustration of the methodology developed to identify the pertinent variables which control the fretting fatigue damage of Ti-6Al-4V alloy is shown in Fig. 3.46.

Fig. 3.43-Fig. 3.45 show some of the performed results for gross slip conditions by Fouvry et al. [12], [11].

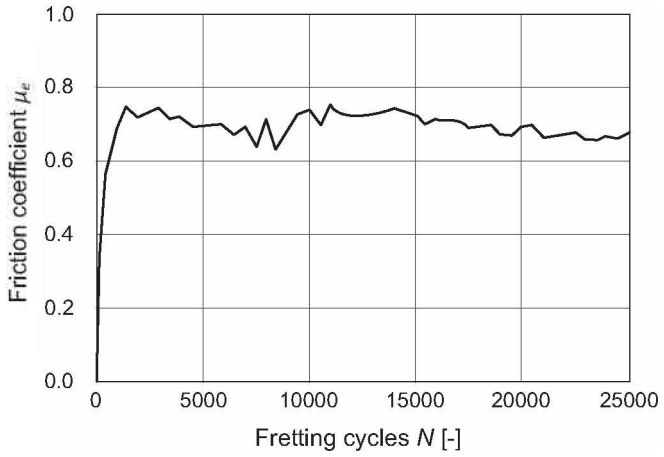

Fig. 3.43: Evolution of the energy friction coefficient (δ = 75 µm) [11]

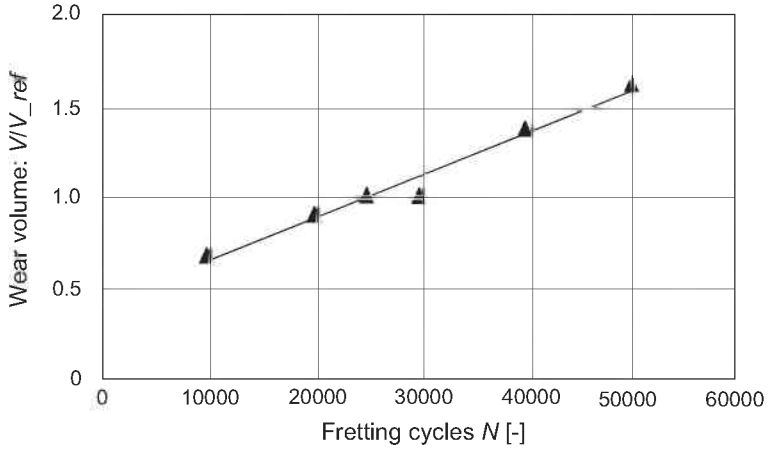

Fig. 3.44: Wear volume extension of Ti-6Al-4V as a function of the fretting cycles [12]

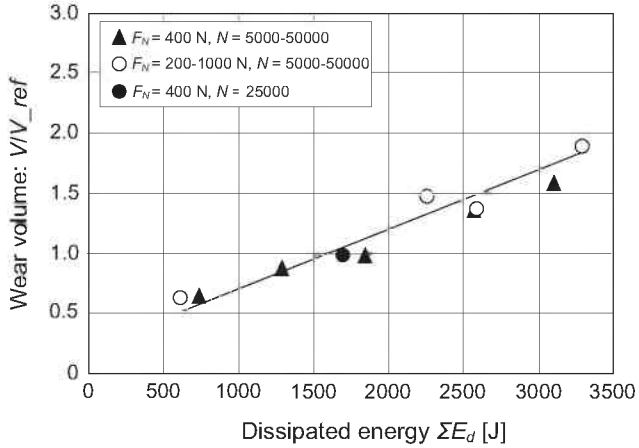

Fig. 3.45: Wear volume of Ti-6Al-4V as a function of the dissipated energy [12]

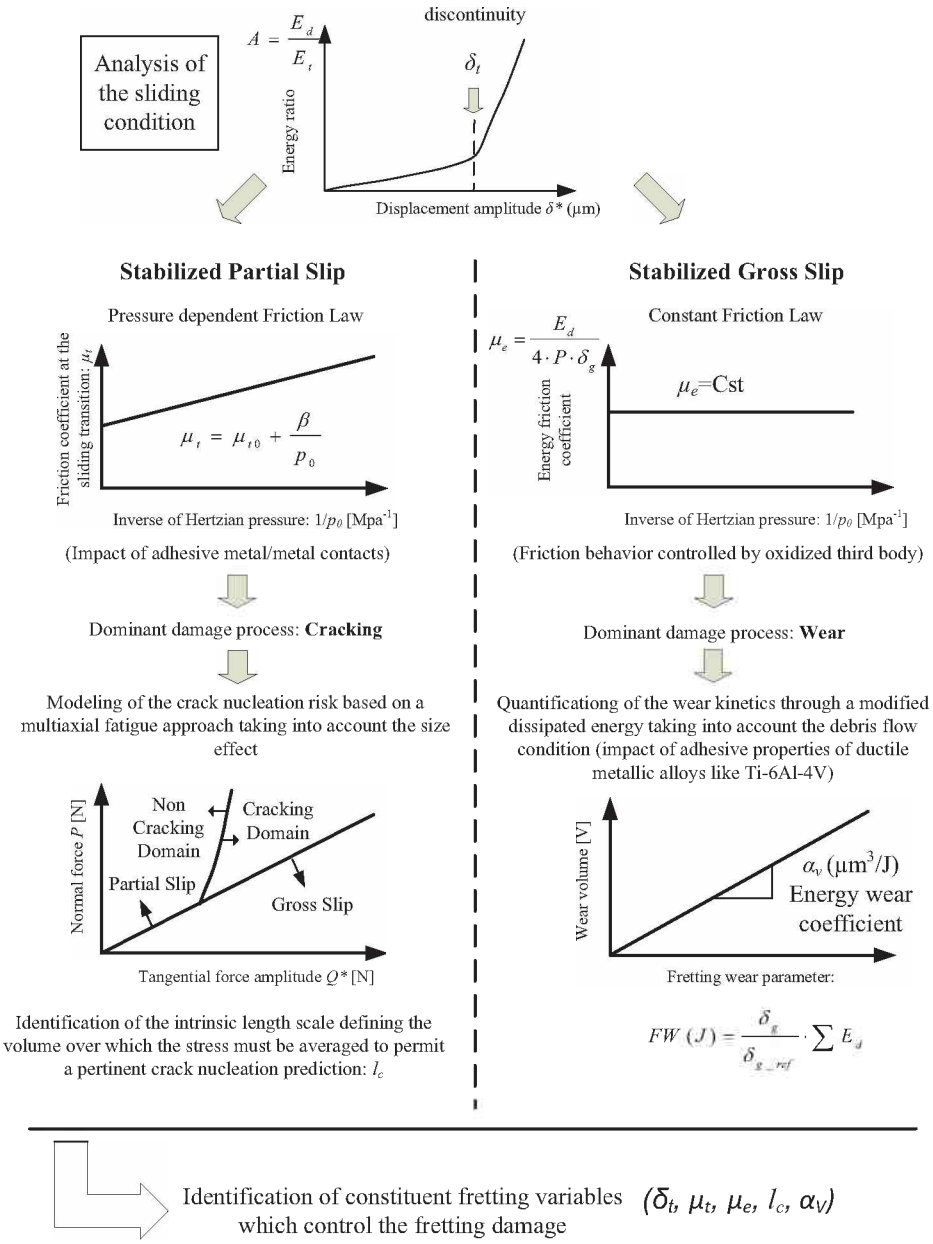

Fig. 3.46: Schematic methodology [11]

Magaziner et al. [32] investigated the wear behavior of Ti–6Al–4V subjected to fretting reciprocating sliding condition to analyze the effects of contact load, relative slip, contact geometry, lubrication, and applied cyclic load on the substrate (specimen). They observed that dry and lubricated surface conditions produced “W” (scar with multiple valleys) and “U” (scar with single valley) shaped scars on both specimen and pad, respectively. They observed also that the wear volume was linearly proportional to cumulative product of contact load and relative slip as well as to the total dissipated energy. These correlations suggested that linear relationships exists to characterize the fretting wear of a material which are independent of the contact load, relative slip, contact geometry, lubrication, and applied cyclic load on the substrate (specimen).

4. Material characterization

The material used for this research was provided by Böhler Schmiedetechnik GmbH & Co KG in form of Ti-6Al-4V V-shape and side-pressed pancake forgings, respectively.

4.1. Forging simulation

The forging processes of the pancakes and V-shapes were simulated with the aid of finite element analysis in the Deform™ software tool. The effective strain distribution of both pancake and V-shape is shown in Fig. 4.1.

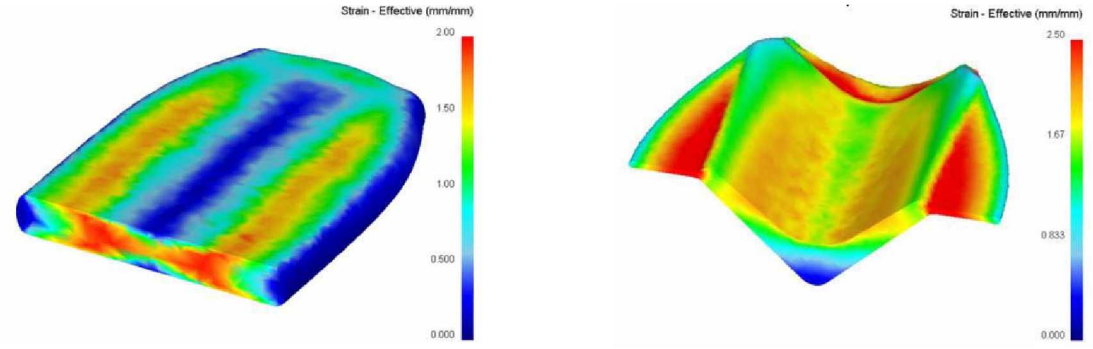

Fig. 4.1: Effective strain distribution of pancake (left) and V-shape (right)

4.2. Forging process

The pancakes were forged on a hydraulic press. The diameter of the feedstock was 45 mm. The forging process was done in one heating (furnace temperature 930°C) with one pressing operation with an average ram speed of 15 mm/s.
The feedstock billet for the V-shape had a diameter of 230 mm. It was heated in a furnace up to 940°C and forged with an open die hammer to semi-finished products with a diameter of 100 mm. These were heated in a rotating hearth furnace up to 930°C and forged at a 350 MN-screw-press in two heats with one blow each heat.

4.3. Heat treatments

For the investigation of the effect of microstructure on fretting fatigue behavior of Ti-6Al-4V, five different microstructures were achieved by different heat treatment processes.

On the one hand, pancakes were subjected to four various heat treatments to obtain mill-annealed (MA), solution treated (ST), recrystallization-annealed (RA) and beta-annealed (BA) microstructures. On the other hand, the V-shapes were heat-treated to mill-annealed and solution treated polymer quenched (STPQ) microstructures. The process parameters for the heat treatments are summarized in Tab. 4.1.

Material	Step 1	Step 2	Microstructure
Pancake MA	720° C / 2 hours /AC	-	Mill-annealed
Pancake ST	950°C / 70 min. /AC	730°C / 2 hours /AC	Bimodal
Pancake RA	950°C / 2 hours	FC to 730°C / AC	Equiaxed
Pancake BA	1030°C / 100 min. / AC	730°C / 2 hours /AC	Lamellar
V-Shape MA	720° C / 2 hours /AC	-	Mill-annealed
V-Shape STPQ	950°C / 70 min. / PQ	720°C / 2 h / AC	Bimodal

Abbr.: AC = air-cooling, FC = furnace-cooling, PQ = polymer-quenching

Tab. 4.1: Heat-treatment processes

4.4. Microstructures

Metallographic sections were produced from all materials. Etching was performed with an etching time of 3 seconds. The composition of the etching medium is represented in Tab. 4.2. All microstructures were analyzed with a light optical microscope. They are discussed below.

Volume	Medium	Concentration
5 ml	HNO_3	70-percent
10 ml	HF	50-percent
85 ml	H_2O	-

Tab. 4.2: Etching medium

4.4.1. Pancake

4.4.1.1. Mill-annealed microstructure

Fig. 4.2 shows the mill-annealed microstructure, where the white region represents the α-phase and the dark region the lamellar (α+β)-phase. Mill-annealing does not cause complete recrystallization, and therefore leads to a distinct texture of the primary α-grain shapes, representative of the forging process. Due to the forging temperature of 930°C, no crystallographic texture occurs in the microstructure.

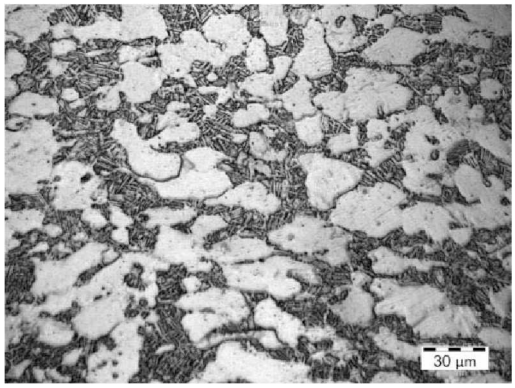

Fig. 4.2: Mill-annealled microstructure

The percentage of the α-phase in comparison to the (α+β)-phase is essentially higher and amounts 76%. According to the line cutting method, two different mean values of primary α-grain sizes were determined. The mean average α-grain size was found to be 8.2 µm and the average grain size in direction of the grain shape elongation was determined to be 8.7 µm. The average colony size of the (α+β)-lamellae-packets amounts 7.1 µm.

4.4.1.1. Solution treated microstructure

A bimodal microstructure, as depicted in Fig. 4.3, is achieved by a solution treatment close under the β-transus temperature.

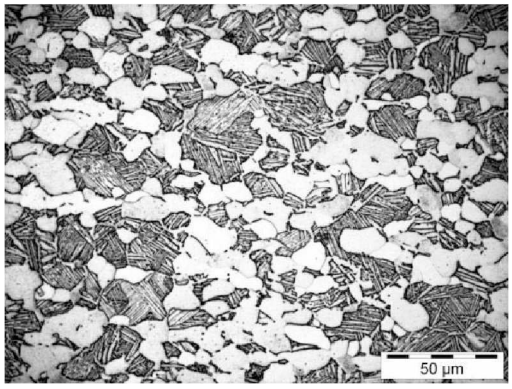

Fig. 4.3: Bimodal microstructure

Basic bimodal microstructures displayed a duplex microstructure with primary alpha grains surrounded by lamellar matrix of (α+β)-phase. The used bimodal microstructure in this study contains 44% lamellar (α+β)-phase. The average primary alpha grain size approximates 7.9 µm. In comparison to the mill-annealed microstructure, the bimodal microstructure exhibits a large colony size of 15.9 µm.

4.4.1.2. Recrystallization-annealed microstructure

An equiaxed microstructure is achieved by a recrystallization process. The favored microstructure can be adjusted with the annealing temperature and annealing time. Thereby, the annealing temperature determines the volume of the primary α-grains and the annealing time the fineness of the microstructure. The analyzed equiaxed microstructure has an average alpha grain size of 11.3 µm, which was determined with the line cutting method (cf. Fig. 4.4).

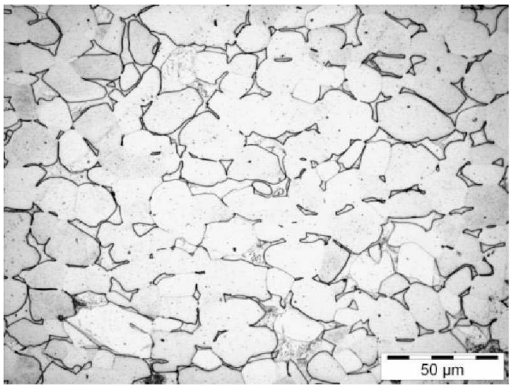

Fig. 4.4: Equiaxed microstructure

4.4.1.3. Beta-annealed microstructure

Lamellar microstructures such as used in this work develop by cooling from a temperature over the β-transus during the transition from the single-phase β-region to the two-phase (α+β)-region. At the transition of the β-transus temperature lamellae occur at first at the grain boundaries and grow then radial in the β-grains. Depending on temperature fine or coarse lamellae accumulate.
Fig. 4.5 depicts the lamellar microstructure used in this work. The lamellar microstructure exhibits an average lamellae width of 0.75 µm and a primary β-grain size of 400 µm.

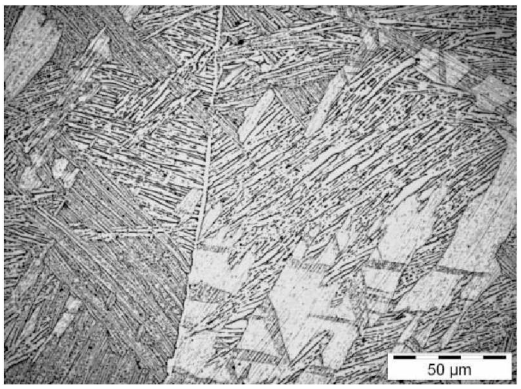

Fig. 4.5: Lamellar microstructure

4.4.2. V-Shape

4.4.2.1. Mill-annealed microstructure

The mill-annealed microstructure of the V-shape (Fig. 4.6) has the same treatment parameters as the mill annealed microstructure of the pancake. Due to the missing recrystallization step, a primary α-grain shape texture is identifiable. In comparison to the pancake mill-annealed microstructure, the (α+β)-phase accounts for only 20%. The mean primary alpha grain size is a little larger, namely 8.7 µm. The average grain size in direction of the grain shape elongation is 10.7 µm and the colony size amounts 10.1 µm.

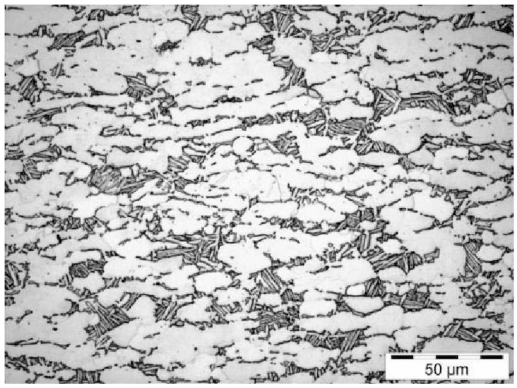

Fig. 4.6: Mill-annealed microstructure

4.4.2.2. Solution treated polymer-quenched microstructure

In comparison to the solution treated microstructure with air-cooling, the solution treated polymer-quenched (STPQ) microstructure has a higher percentage of (α+β)-phase, namely 62.4%. The primary alpha grain size amounts 8.3 µm and the colony size is 13.4 µm. Fig. 4.7 depicts the solution treated polymer-quenched microstructure.

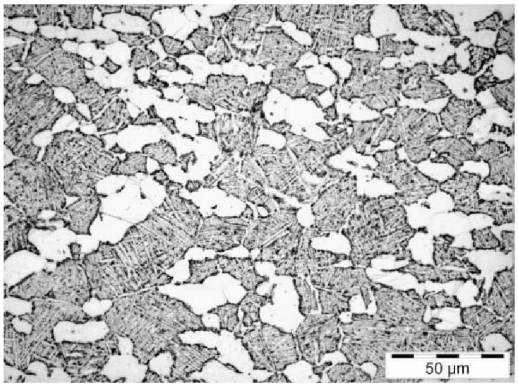

Fig. 4.7: STPQ microstructure

4.5. Micro-hardness of the microstructures

The micro-hardness of the different microstructures was measured with a micro-hardness tester (Micro-Duromat 4000). This micro-hardness tester has the alternative to use two different indenters, the Vickers diamond pyramid or the Knoop elongated diamond pyramid. In this study the Vickers diamond pyramid was used. The procedure for testing is very similar to that of the standard Vickers hardness test, except that it is done on a microscopic scale with higher precision instruments. The surface being tested generally requires a metallographic finish.

Four different microstructures were analyzed and evaluated, namely recrystallization-annealed, mill-annealed, solution treated, and solution treated polymer-quenched. In Fig. 4.8, micro-indentations in these microstructures are shown.

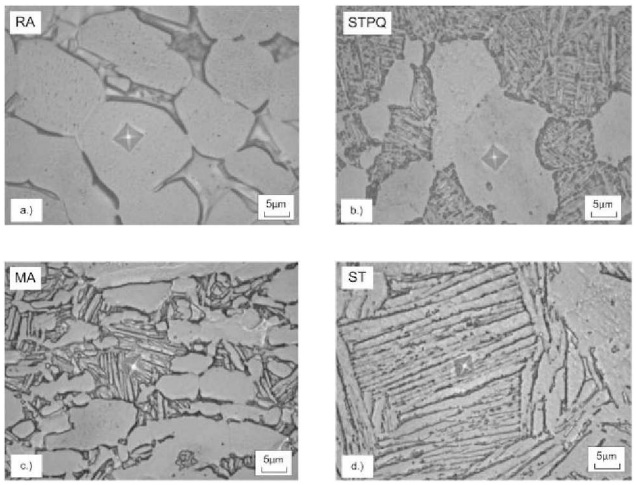

Fig. 4.8: Micro-hardness indentations

For every phase and microstructure, twenty indentations were performed. The diagonals of the Vickers pyramid indentations (Fig. 4.9) were admeasured with an optical microscope and documented. According to Vickers the hardness is defined as the applied load [kp] divided by the surface area of the indentation [mm^2]. The applied load at all measurements was 10 pond, which approximates 0.01 N.

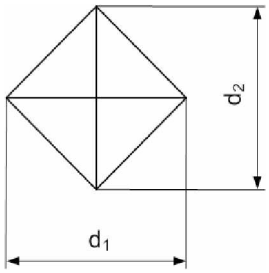

Fig. 4.9: Diagonals of the pyramid indentation

The formula for the calculation of the Vickers hardness (HV) is presented in Equ. (4.1), where F is the applied load in kilopond and d is the arithmetic mean of the two diagonals, d_1 and d_2, in mm.

$$HV = 1.854 \cdot \frac{F}{d^2} \qquad \text{Equ. (4.1)}$$

It was determined that the results of the micro-hardness measurements can be represented with the Weibull distribution. The formula for the probability is depicted in the following equation. The parameters b and T were calculated according to the method of Gumbel.

$$R(t) = e^{-\left(\frac{t}{T}\right)^b} \qquad \text{Equ. (4.2)}$$

The results of the micro-hardness measurements are presented in Fig. 4.10. Thereby, the cumulative probabilities of the different microstructural phases are plotted versus micro-hardness.

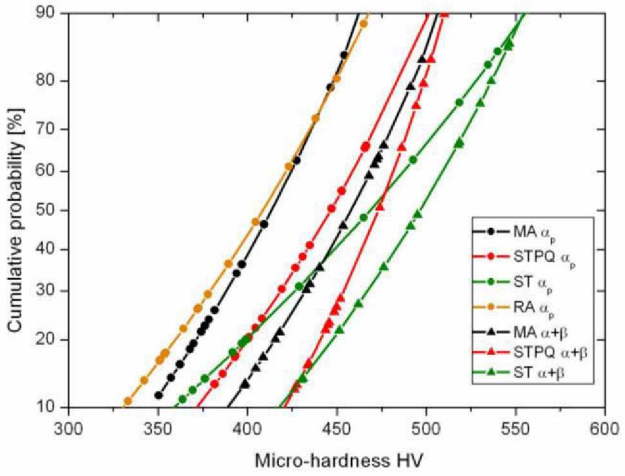

Fig. 4.10: Micro-hardness results

In Fig. 4.10, it is apparent that the primary alpha grains of the recrystallization-annealed and of the V-shape mill-annealed microstructure have the lowest micro-hardness, whereas the (α+β)-phase of the ST microstructure has the highest micro-hardness. In general, the (α+β)-phase exhibits higher micro-hardness values compared with the primary α-grains of the same microstructure.

The measured micro-hardness values were weighted with respect to their phase contents at a probability of 63% with the Equ. (4.3). The weighted values of all microstructures are represented in Tab. 4.3.

$$HV_w = \frac{HV_\alpha \cdot C_\alpha + HV_{(\alpha+\beta)} \cdot C_{(\alpha+\beta)}}{100} \qquad \text{Equ. (4.3)}$$

HV_w	Weighted micro-hardness HV
HV_α	Micro-hardness of α_p-phase at 63% probability
$HV_{(\alpha+\beta)}$	Micro-hardness of (α+β)-phase at 63% probability
C_α	Content of α_p-phase
$C_{(\alpha+\beta)}$	Content of (α+β)-phase

	STPQ	RA	MA	ST
HV_w	476	425	437	501

Tab. 4.3: Weighted micro-hardness of microstructures

The weighted micro-hardness values are compared in Fig. 4.11. The solution treated microstructure exhibits the highest, and the recrystallization-annealed microstructure the lowest micro-hardness. The difference between them amounts 15%.

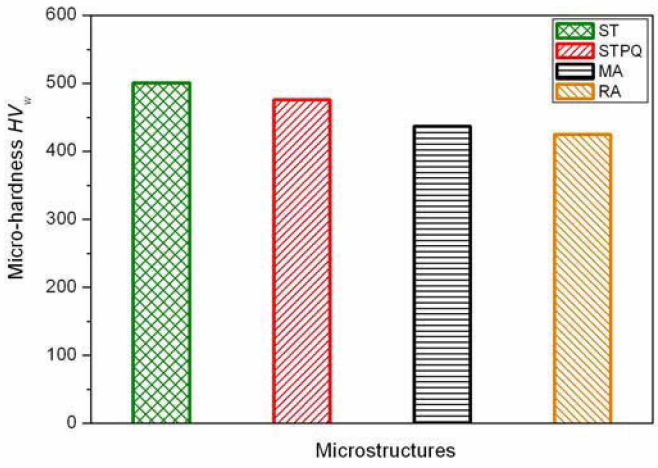

Fig. 4.11: Micro-hardness in respect of microstructure

5. Experimental procedure

5.1. Aim of the investigations

The aim of the investigations is to determine the influence of different parameters such as microstructure, temperature, relative slip amplitude and normal load, on fretting wear and fretting fatigue.

5.2. Used test equipment

5.2.1. Confocal laser scanning microscope Olympus LEXT OLS3000

The LEXT is a confocal laser scanning microscope for ultra-precise measurements and observations with the highest levels of reliability from the company Olympus, which accomplishes a resolution of 0.12 µm and exhibits a total magnification, from 120-timesl to 14,400-times. Both 3D-observations and high-precision 3D-measurements are possible in real time, which is ideal for surface observations. In this work the roughness of the fretting area was determined with the LEXT.

5.2.2. Light optical microscope Olympus BX51M

This microscope exhibits a magnification up to 100-times and was used to analyze the microstructure of the material.

5.2.3. Light optical stereo microscope Olympus SZX12

The stereo microscope with a magnification ranging from 3.5-times to 144-times was used to analyze the fretting and fracture surfaces.

5.2.4. Micro-Duromat 4000

The micro-hardness tester Micro-Duromat 4000, attached to the optical microscope Reichert-Jung was used to determine the micro-hardness of the different microstructures.

5.2.5. Instron Fasttrack 8800

Instron Fasttrack 8800 is a uniaxial servo hydraulic testing machine with a nominal force of 10kN, which was used to accomplish the fretting wear tests.

5.2.6. SincoTec Power Swing 100 MOT

SincoTec Power Swing 100 MOT is an electromotive resonance testing machine with a nominal force of 100 kN. All fretting fatigue tests were carried out with this testing machine, which is shown in Fig. 5.6.

5.2.7. Fretting test rig

The used fretting test rig was designed at the Chair of Mechanical Engineering by Reichhart [42] and modified by Reiser [43]. It was used for the fretting wear and fretting fatigue tests.

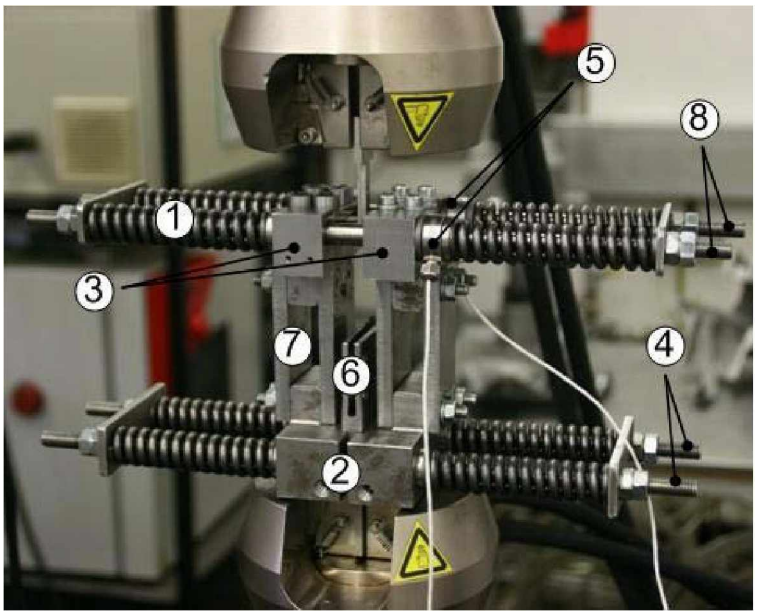

Fig. 5.1: Test rig for fretting

The basic assembly of the test rig consists of eight coil springs (1), lower clamping jaws (2), upper clamping jaws (appliance for pads) (3), two thread rods (4), two load cells (5), clamping bracket (6), four metal sheets (7) and two thread bolts with check rails (8), as depicted in Fig. 5.1.
During fretting testing the hydraulic jaws of the testing machine are clamped on the clamping bracket. Two rigid clamping jaws (2) are friction-locked with the clamping bracket (6). The clamping force was applied through preloaded coil springs. The lower clamping jaws (2) are jointed through four metal sheets (7) with the upper clamping jaws (3), which are guided on two thread rods with check rails (8). In both upper clamping jaws (3) pads can be clamped. Two load cells were used to measure the normal load on the pads. Hence it is possible to apply well-defined normal forces on the pads. The clamping force is thereby applied with coil springs.

5.3. Specimen and pad geometry

Fig. 5.2 shows the test specimen with dog-bone shape used in this study for the fretting fatigue tests. The specimen for fretting wear tests is depicted in Fig. 5.3. Both specimens have the same geometry in the contact region where the pads were applied, with a width of 7 mm and a thickness of 4 mm. All specimens were machined and additionally polished with an abrasive paper (600 µm grit).

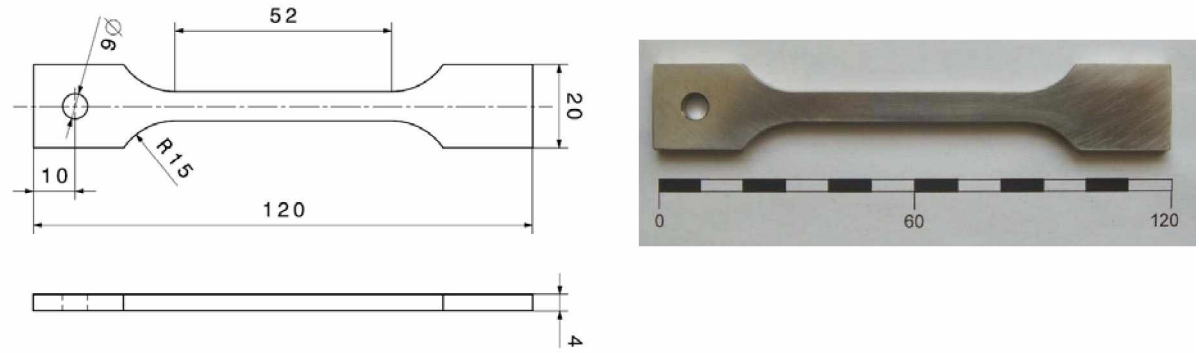

Fig. 5.2: Fretting fatigue specimen

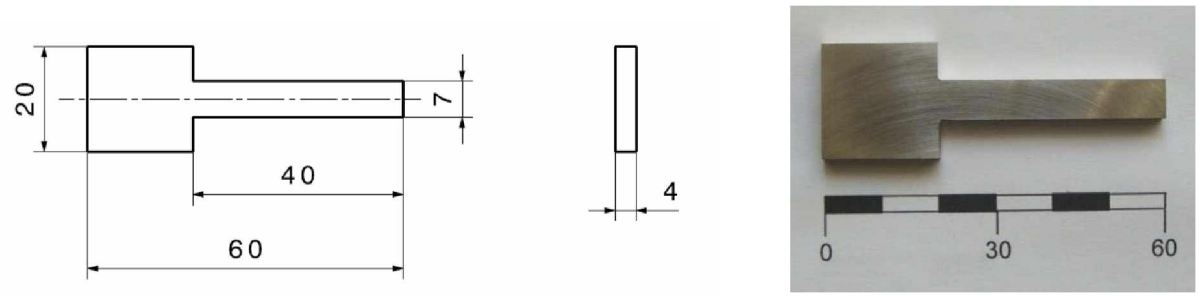

Fig. 5.3: Fretting wear specimen

The pad geometry is for both, fretting fatigue and fretting wear tests the same, Fig. 5.4. At first, the pads were machined on a milling machine. Then, the radius of the pads was machined on a turning machine with a purpose adapter.

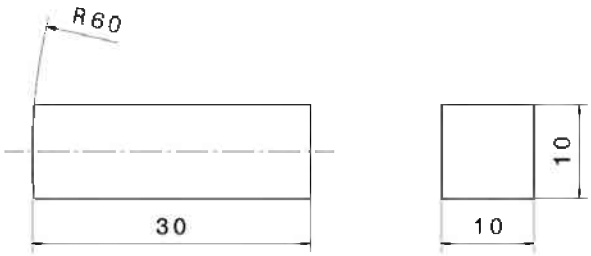

Fig. 5.4: Pad geometry

To compare the surface conditions of the specimens and pads, the roughness of them was measured with a confocal laser scanning microscope (LEXT), with a cut-off of 98.1 µm. Fig. 5.5 shows the 3-D-topography of both polished specimen and turned pad. A slight difference in the arithmetic mean height was determined.

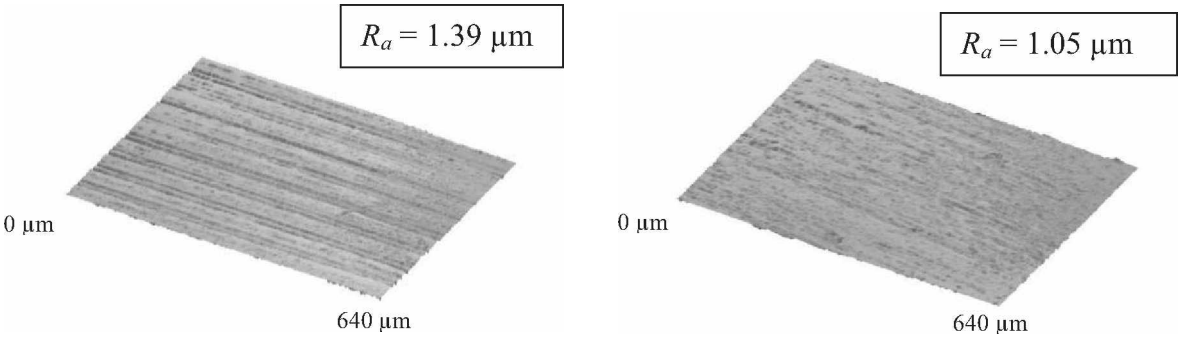

Fig. 5.5: 3-D-topography: pad (left), specimen (right)

5.4. Experimental Setup

5.4.1. Fretting Fatigue

All fretting fatigue tests were carried out on an electromotive resonance testing machine under stress controlled mode (Fig. 5.6). During fretting fatigue testing the specimen was fixed on one side at the clamping bracket of the fretting test rig and on the other side at the actuator .of the resonant testing machine. The pads were exactly aligned to the fretting fatigue specimen. The normal load between specimen and pads was adjusted through coil springs and load cells. Applying a defined stress-amplitude to the specimen leads to a relative oscillatory displacement in the contact between specimen and pads.

Fig. 5.6: Fretting fatigue testing setup

The fretting fatigue tests were conducted with a frequency of 57 Hz. During the testing procedure the temperature and the normal load were recorded. To be able to accomplish these measurements, additional hard- and software were used:

- HBM Spider 8 measurement amplifier
- Load cells with an effective range of 0-40kN
- HBM Catman® Software for the adjustment of the load cells and for reading of the measurements
- Thermo elements for temperature measurements

HBM Catman® is a powerful data acquisition software for configuring, visualizing and analyzing measurements. The load cells and the thermo elements were implemented in the software with an HBM Spider 8 measurement amplifier.

5.4.2. Fretting wear

The fretting wear tests were carried out on a uniaxial hydraulic testing machine under displacement controlled mode (Fig. 5.7). During the fretting wear testing, the specimen was mounted on a rigid clamping device of the hydraulic testing machine. The normal load between specimen and pads was adjusted through coil springs and load cells, identical to fretting fatigue testing. The relative displacement amplitude between pads and specimen was achieved with the hydraulic testing machine in displacement controlled mode.

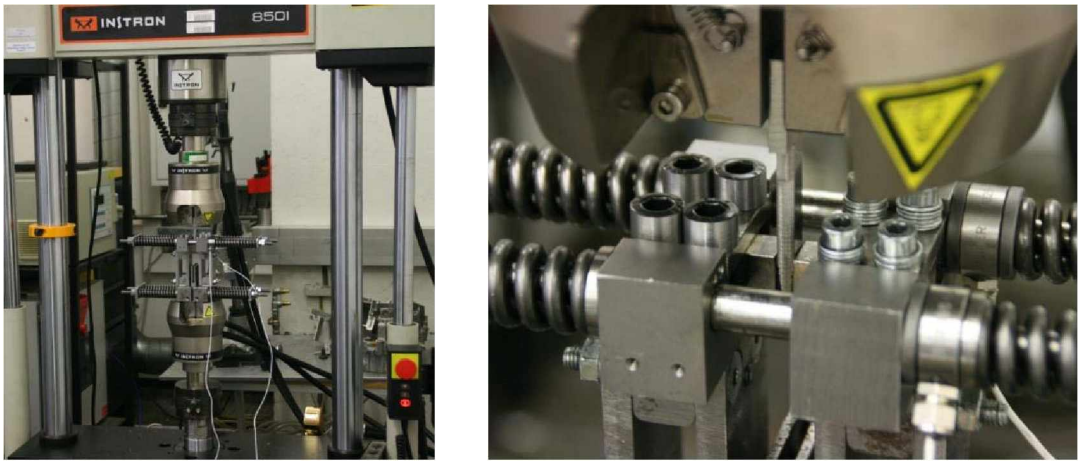

Fig. 5.7: Fretting wear testing setup

A frequency of 20 Hz was used during all fretting wear tests. The measurement equipment for the normal load and the temperature was the same as for fretting fatigue testing. Different parameters were recorded, such as the frictional force or tangential load, the relative slip amplitude and the number of cycles. The normal force of the pads was kept constant.

6. Experimental results

6.1. Fretting wear

Fretting wear tests were carried out to characterize the wear behavior in respect of varying parameters such as normal load, fretting cycles and relative slip amplitudes on a cylinder/plane contact. For the characterization of the fretting wear behavior of Ti-6Al-4V, a specific set of experiments were arranged, such as shown in Fig. 6.1. The black points depict the accomplished fretting wear tests. Unless otherwise noted, the fretting wear tests were performed with non-lubricated contact condition. The material for these fretting tests has the mill-annealed microstructure.

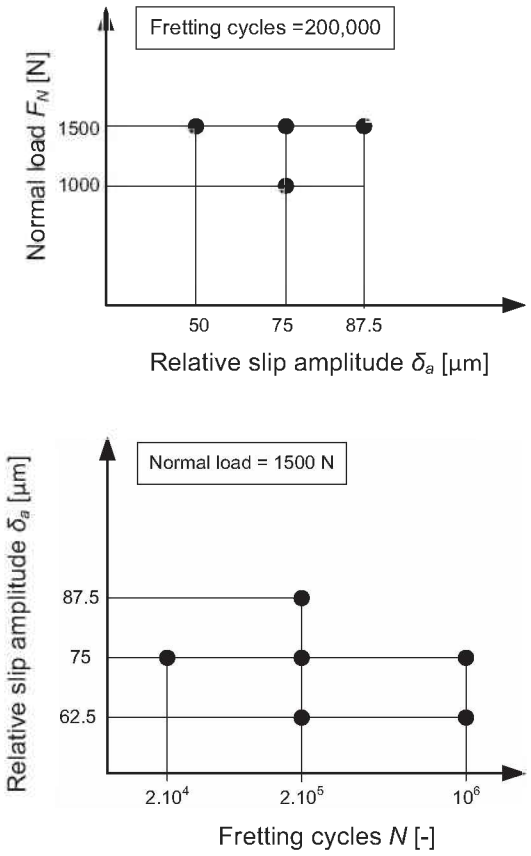

Fig. 6.1: Illustration of the experimental test procedure

The applied normal loads F_N of 1000 N and 1500 N correspond to Hertzian pressure of 218 and 267 MPa.

For every fretting wear test, the tangential load was plotted three-dimensionally versus imposed displacement and number of cycles by using the recorded data (cf. Fig. 6.2).

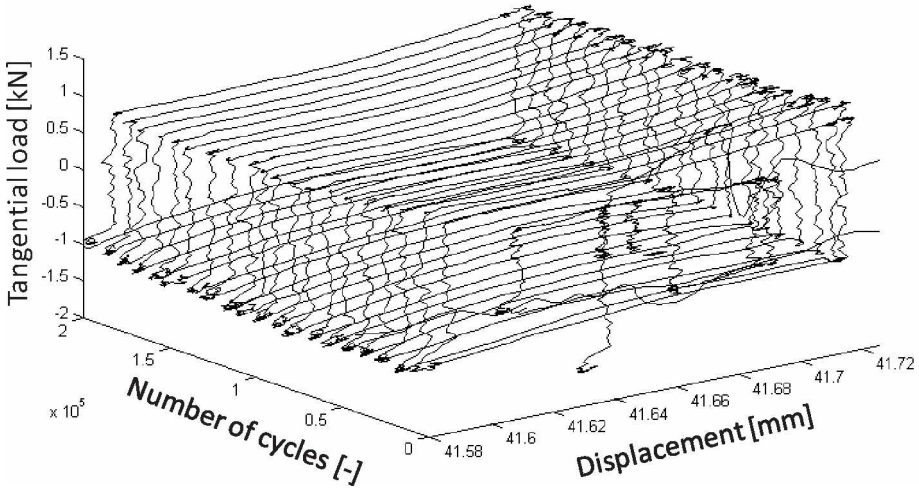

Fig. 6.2: 3D-plot of the hysteresis from an accomplished fretting wear test

The hystereses were analyzed and the dissipated energy was calculated for every fretting cycle of each test with the software tool MATLAB®. In Fig. 6.3, a hysteresis of a fretting cycle is shown at which the area defines the dissipated energy.

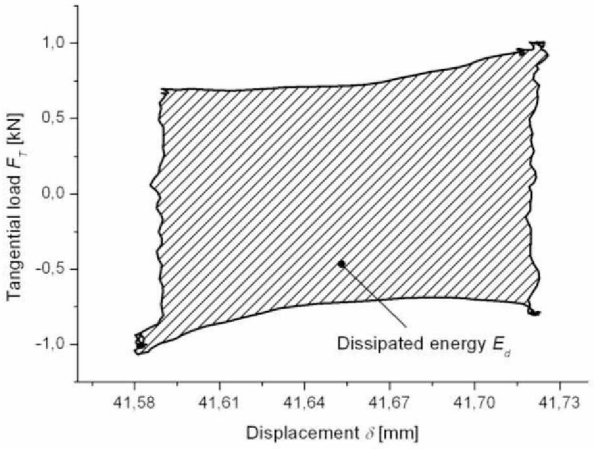

Fig. 6.3: Hysteresis of one tested fretting cycle

All tests were conducted under gross slip conditions, which is characterized through square and open fretting loops.

6.1.1. Friction analysis

For the characterization of the friction behavior of the fretting wear tests, the friction law according to Fouvry et al. [11], based on an energy description, was used. This is necessary, because the normalized tangential force ratio F_T/F_N is no longer appropriate due to plunging effect (cf. Fig. 6.4). Equ. (6.1) shows the used friction law, where an energy friction coefficient μ_e is defined.

$$\mu_e = \frac{E_d}{4 \cdot F_N \cdot \delta_0} \qquad \text{Equ. (6.1)}$$

E_d Dissipated energy for one cycle [J]
F_N Normal load [N]
δ_0 Displacement amplitude when $F_T = 0$

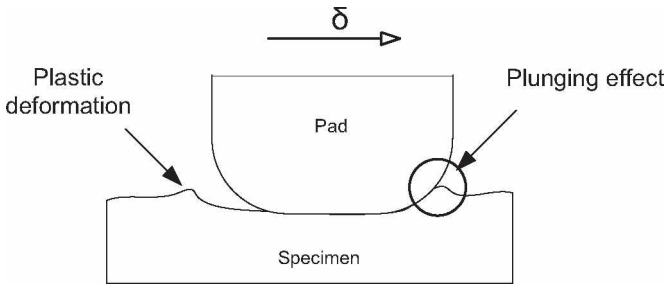

Fig. 6.4: Illustration of the plunging effect

In Fig. 6.5 the friction coefficient of two different normal loads is shown, whereas the relative slip amplitude was the same for both. The distribution of the friction coefficient for the lower pressure is slight lower in comparison to the higher pressure.

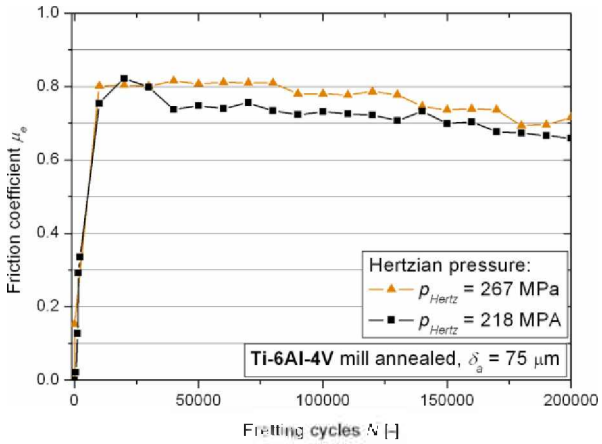

Fig. 6.5: Energy friction coefficient distribution for different Hertzian pressures

Generally, in the first few hundred cycles, the friction coefficient increases, which corresponds to establishment of the metal/metal contact and the formation of a tribologically transformed structure, called TTS.

The friction coefficient distributions for different relative slip amplitudes, where the normal force was kept constant are depicted in Fig. 6.6. It was observed that the friction coefficient with decreasing amplitude decreases.

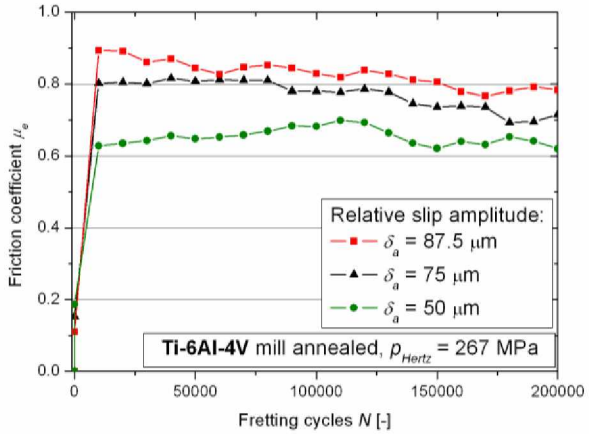

Fig. 6.6: Energy friction coefficient distribution for different relative slip amplitudes

The friction distributions as represented before were recorded up to 200,000 fretting cycles. Additionally fretting tests were conducted to show the friction distribution until to 10^6 fretting cycles for lubricated and non-lubricated test conditions. For the lubricated condition, specimen and pads were lubricated with a thin film of commonly used corrosion oil. In real components these corrosion oils are also used before assembling.
It was observed for the lubricated condition for the first 10^5 fretting cycles, that the coefficient of friction increases fast to 0.6 and then slightly to 0.8. For the non-lubricated condition the coefficient of friction increases direct after a few hundred fretting cycles to a value of circa 0.8. After 10^5 fretting cycles the coefficient of friction decreases slightly for both the lubricated and the non-lubricated fretting tests and seems to reach a plateau of 0.65 at 10^6 fretting cycles.

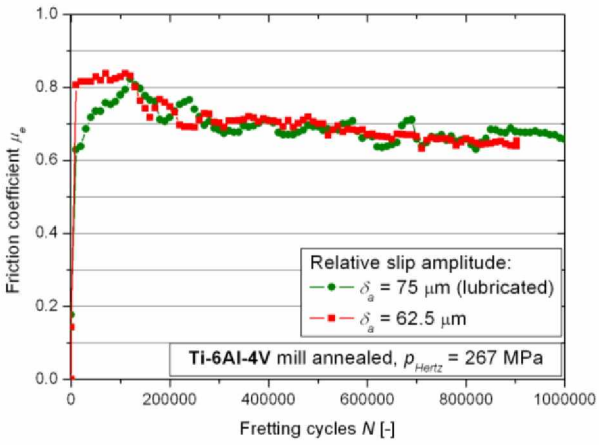

Fig. 6.7: Energy friction coefficient distribution until to 10^6 fretting cycles

6.1.2. Wear analysis

Before fretting wear testing, specimens and pads were cleaned twice with acetone to remove dust and dirt. The cleaned specimens and pads were subsequently weighed with a high precision scale. After fretting wear testing, both the specimens and pads were once again cleaned fairly with acetone and weighed. This procedure was done to determine the wear mass, which was removed due to fretting during the fretting wear testing.

It was determined that the wear mass increases potentially with the fretting cycles, as shown in Fig. 6.8, if the normal load and the relative slip amplitude are kept constant. No influence of normal load on wear mass was observed for the applied testing conditions in this study. Fig. 6.9 shows a horizontal distribution of the wear mass for two different normal loads. This declaration was also certified at the comparison of wear mass as a function of relative slip amplitude, whereas fretting tests with two different normal loads were accomplished. The wear mass increases linear with the amplitude and both the tests with lower and higher pressure lie on the linear line, as depicted in Fig. 6.10.

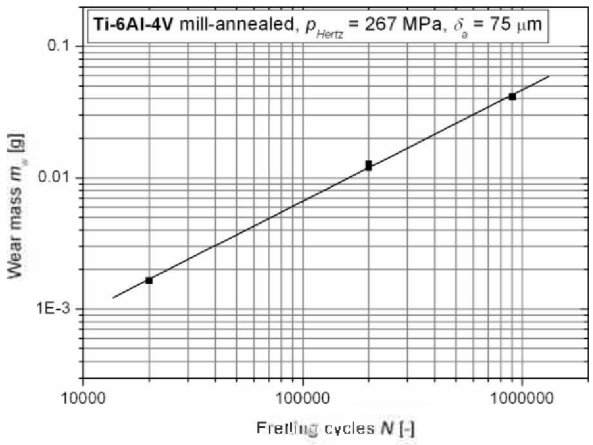

Fig. 6.8: Wear mass distribution of Ti-6Al-4V as a function of the fretting cycles

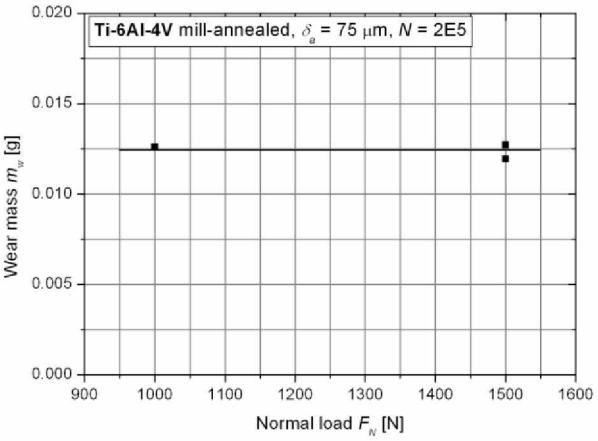

Fig. 6.9: Wear mass distribution of Ti-6Al-4V as a function of the normal load

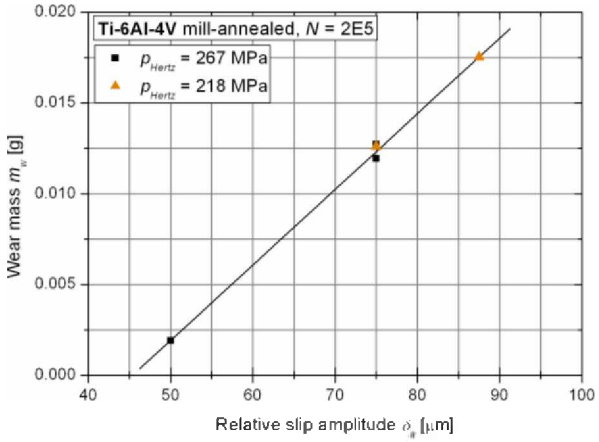

Fig. 6.10: Wear mass distribution of Ti-6Al-4V as a function of the relative slip amplitude

The removed wear mass was compared with the dissipated energy during fretting wear testing. As mentioned before, the dissipated energy was calculated with the aid of fretting hysteresis. It was observed that a linear correlation between wear mass and dissipated energy exists. Those fretting tests with the test condition of 267 MPa Hertzian pressure and 75 µm relative slip amplitude show a good accordance with the linear correlation. The other fretting wear tests deviate slightly from the linear correlation owing to the variation of relative slip amplitude and Hertzian pressure.

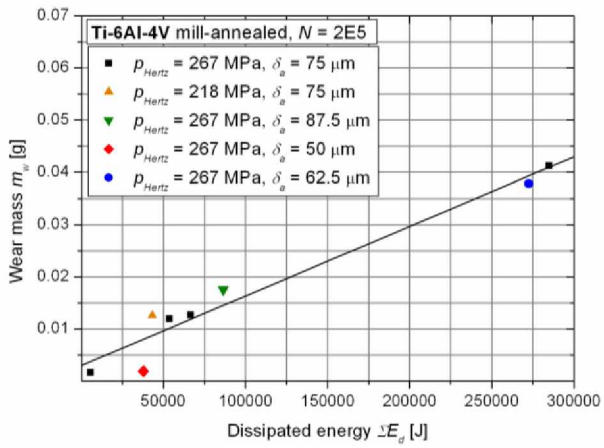

Fig. 6.11: Wear mass distribution of Ti-6Al-4V as a function of the dissipated energy

The wear energy density is used to characterize, which friction energy is essential to remove a defined wear volume. The wear energy density is defined according to Equ. (6.2). For the calculation of the wear energy density, the measured wear mass m_w was converted with the density of Ti-6Al-4V to the removed wear volume V_w.

$$e_v = \frac{\Sigma E_d}{V_w} \qquad \text{Equ. (6.2)}$$

ΣE_d Summation of the dissipated energy during the fretting wear test
V_w Removed wear volume

A potential correlation was observed between wear energy density and fretting cycles, Fig. 6.12, for a relative slip amplitude of 75 µm and a Hertzian pressure of 267 MPa. The wear energy density e_v increases with a increasing of fretting cycles. This can be attributed to the fact that the contact area increases with increasing wear volume and leads therefore to lower Hertzian pressure.

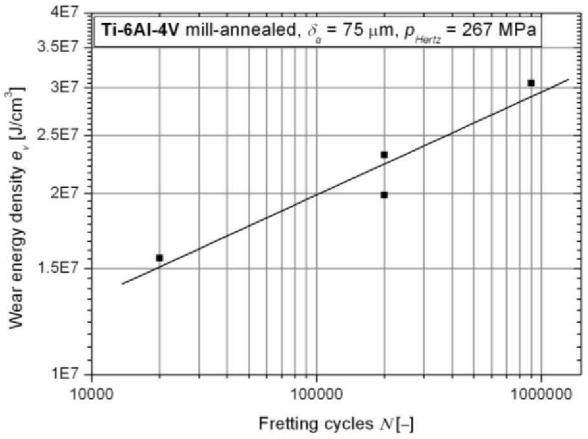

Fig. 6.12: Wear energy density of Ti-6Al-4V as a function of the fretting cycles

The damaged regions of the fretting wear specimens were analyzed with a light optical microscope. Fig. 6.13 shows two damaged surfaces after 200,000 fretting cycles, with different testing amplitudes, whereas the Hertzian pressure was the same for both. On the damaged surface, the produced brittle and hardened material due to fretting is visible. It is spalling and forms the debris powder during the fretting wear tests. It was observed that the surface degradation increases with higher testing relative slip amplitude

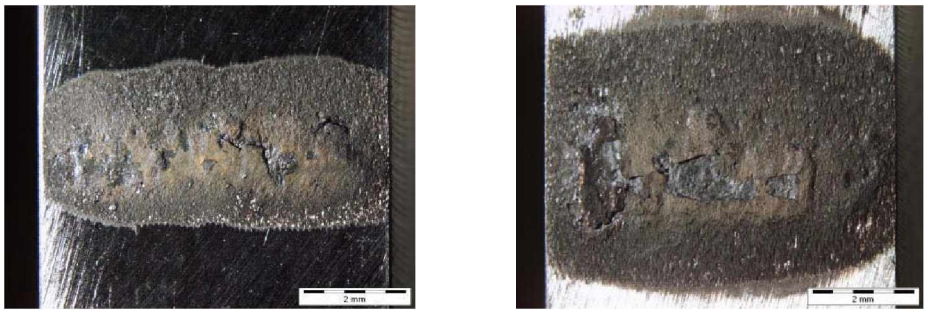

Fig. 6.13: Fretting wear damaged surface after 200,000 fretting cycles: δ_a = 50 µm (left), δ_a = 75 µm (right)

Fig. 6.14 shows a fretting damaged surface after 10^6 fretting cycles. The comparison of the damaged surface after $2 \cdot 10^5$ (Fig. 6.13) and 10^6 (Fig. 6.14) reveals that the contact area between specimen and pads increases with increasing fretting cycles due to the wear losses.

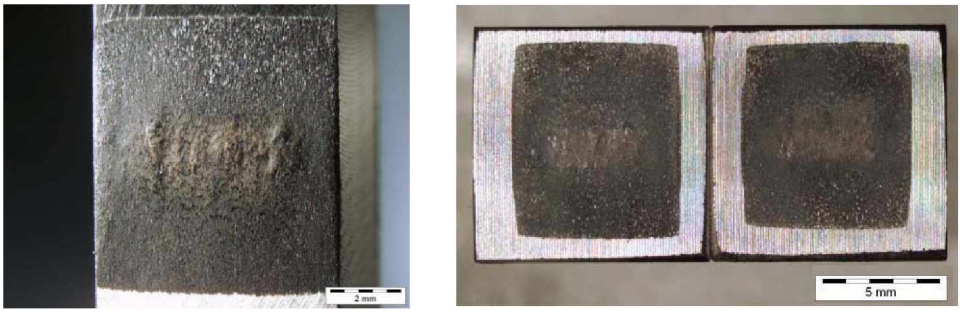

Fig. 6.14: Fretting wear damaged surface after 10^6 fretting cycles: $\delta = 75$ µm, $p_{Hertz} = 267$ MPa

6.1.3. Influence of microstructure on fretting wear

Fretting wear tests were performed for different microstructures of Ti-6Al-4V. For all microstructures, the fretting wear tests were conducted up to 2E4 fretting cycles with a Hertzian pressure of 267 MPa and a relative slip amplitude of 75 µm. For characterization of the influence of microstructure on fretting wear, the wear energy density, was used, Tab. 6.1.

	ΣEd [J]	μ_e	m_w [g]	e_v [J/cm^3]
ST1	5910	0.82	0,0007	3.7E7
ST2	5205	0.74	0,00066	3.4E7
STPQ1	5699	0.74	0,00169	1.5E7
STPQ2	5554	0.74	0,00128	1.9E7
RA1	6333	0.78	0,00113	2.5E7
RA2	5747	0.78	0,00126	2.0E7
V-shape MA	5817	0.78	0,00165	1.5E7

Tab. 6.1: Fretting wear parameters of different microstructures

The results were compared in the following diagram. It was observed, that the solution treated microstructure has the highest wear energy density. This means, that this microstructure has the highest wear resistance in comparison to the other microstructures. The recrystallization-annealed microstructure has a slightly higher wear energy density than the V-shape mill-annealed and solution treated polymer-quenched.

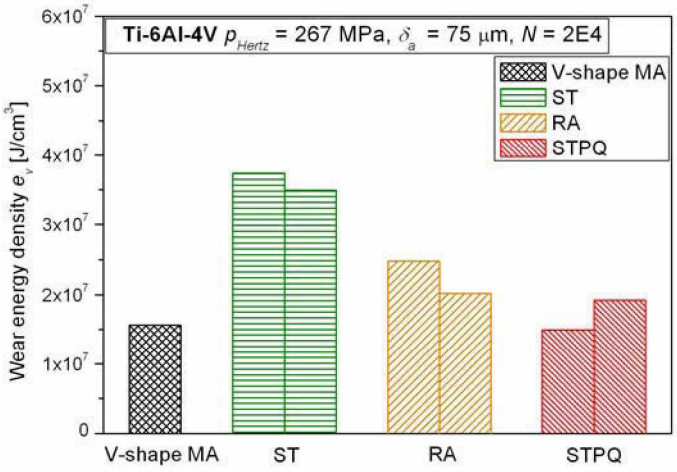

Fig. 6.15: Influence of the microstructure on fretting wear

The fretting wear damaged surfaces of the solution treated and recrystallization-annealed microstructures are depicted in Fig. 6.16 and Fig. 6.17. No special surface degradation was observed in respect of microstructure.

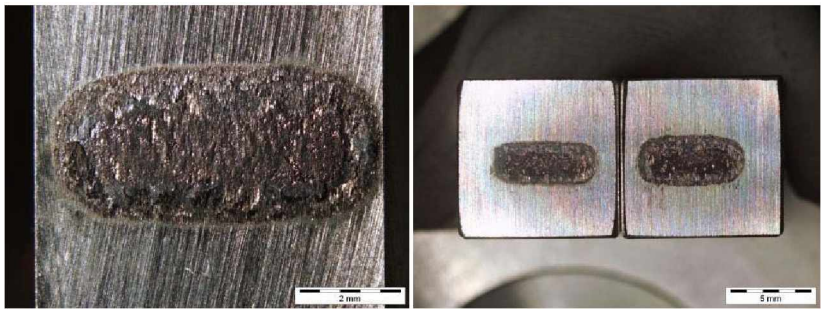

Fig. 6.16: Fretting wear damaged surface of solution treated microstructure

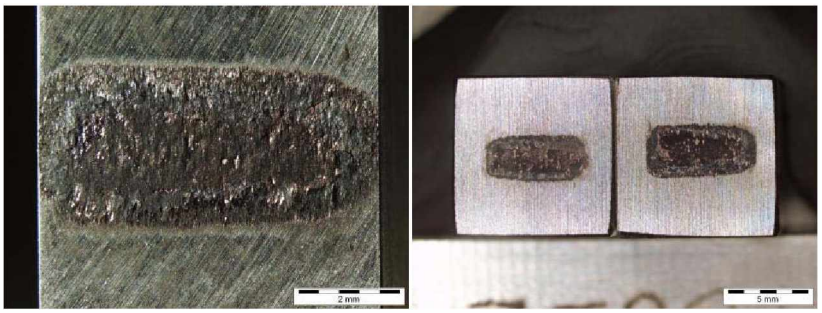

Fig. 6.17: Fretting wear damaged surface of a recrystallization-annealed microstructure

6.1.4. Discussion

The friction distribution, wear behavior and influence of different microstructures on fretting wear were investigated under gross slip conditions. Tests with two different normal loads and hence contact pressure were performed. The friction coefficient for the lower pressure of 218 MPa is slightly lower (~5%) than those of the higher pressure of 267 MPa. It was observed that the friction coefficient decreases with decreasing slip amplitude.

Fretting wear tests showed that with increasing fretting cycles or relative slip amplitude, the wear mass increases, whereas no influence of the contact pressure was observed. The wear mass has a linear correlation with the dissipated energy and increases with increasing dissipated energy. A potential correlation was observed between wear energy density and fretting cycles. This can be attributed to the fact that the contact area increases with increasing wear volume and leads therefore to lower Hertzian pressure. It was observed that the surface degradation increases with higher testing relative slip amplitude.

A comparison of different Ti-6Al-4V microstructures revealed, that the bimodal microstructure has the highest wear resistance. It can be assumed that the micro-hardness of the solution treated microstructure is one reason for the highest wear resistance. Micro-hardness tests showed that this microstructure has the highest micro-hardness of all investigated microstructures. No special surface degradation was observed in respect of microstructure.

In literature no comparable investigations were found for the influence of microstructure on fretting wear. All further investigated results tie in well with the experimental data of Fouvry et al. [11], [12], cf. Fig. 3.43 to Fig. 3.45. Fu et al. [13] and Magaziner et al. [32], reported similar results. Other authors, such as Jin and Mall [24] or Lee and Mall [29], determined the friction coefficient with the use of the normalized tangential force ratio F_T/F_N. Therefore the distributions of the friction coefficients in their studies deviate from presented results in this thesis. They do not account the plunging effect, which is caused by plastic deformation in the contact range. However, this has an essential effect on the frictional behavior at the contact between pads and specimen.

6.2. Fretting Fatigue

6.2.1. Influence of microstructure

Fretting fatigue tests were carried out, to determine the influence of microstructure on fretting fatigue strength. The fretting fatigue test results are depicted in Fig. 6.18. Five different microstructures were investigated. The testing frequency for all tests was 57 Hz. The normal load of the pads on the fretting fatigue specimen was kept constant with a Hertzian pressure of 268 MPa. The performed stress ratio R (ratio of minimum and maximum stress) was $R = 0$.

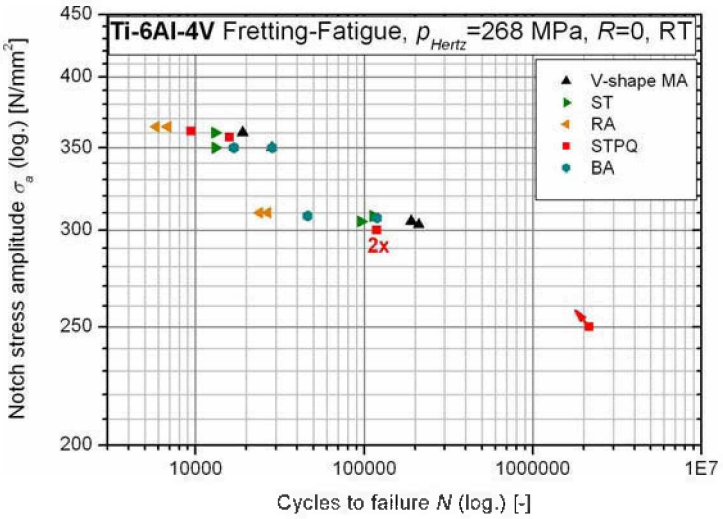

Fig. 6.18: Fretting fatigue strength in respect of microstructure

It was observed that the recrystallization-annealed microstructure has the lowest fretting fatigue strength. The solution treated, solution treated polymer-quenched and beta-annealed microstructures exhibit almost the same fretting fatigue life. It has to be mentioned that the beta-annealed microstructure has a high scatter range (cf. Fig. 6.18). The mill-annealed V-shape shows the highest fretting fatigue strength. At a stress amplitude of 320 MPa, the fatigue life of the V-shape with the mill-annealed microstructure is two times higher than those of the solution treated, solution treated polymer-quenched and beta-annealed microstructures. In contrast, the recrystallization-annealed microstructure has an almost ten times lower fretting fatigue life than the V-shape mill-annealed microstructure.
The experimental data was fitted for each microstructure with a power law representing a line in double logarithmic scale, Fig. 6.19. This allows for a qualitative comparison of the fretting fatigue strength in respect of microstructure. The plain fatigue strength was calculated according to Oberwinkler B. [38]. His models permit the determination of the fatigue strength of Ti-6Al-4V for the high cycle, finite life and low cycle fatigue region. These models incorporate parameters such as microstructure, relative stress gradient, mean stress, multiaxial loading, flaws, surface state and temperature. Using the established microstructural parameters, it was possible to calculate the plain fatigue strengths for different microstructures.

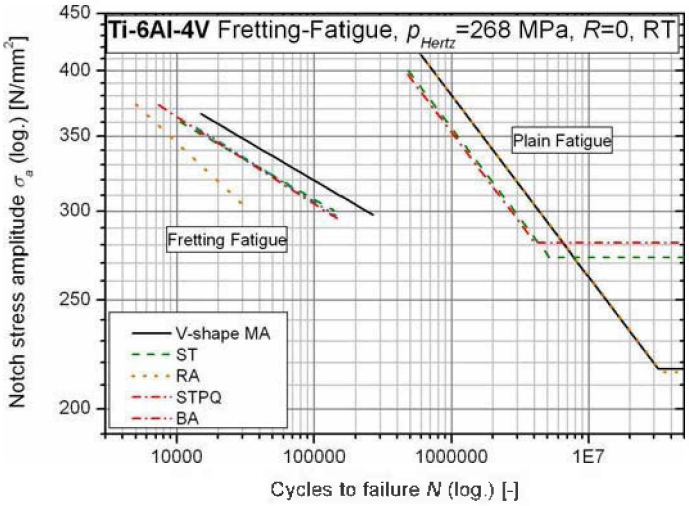

Fig. 6.19: Fretting fatigue and plain fatigue results of different microstructures

Comparing the plain and fretting fatigue data, it is obvious that fretting significantly decreases the fatigue strength. However, the influence of microstructure is similar for both, fretting and plain fatigue. At a stress level of 320 MPa, the V-shape mill-annealed microstructure exhibits a thirty-times lower fatigue life due to fretting in comparison to the plain fatigue data. An anomalous behavior was determined for the recrystallization-annealed microstructure, which has one of the highest plain fatigue strengths, whereas the fretting fatigue strength is the lowest of all microstructures. An explanation for this behavior is given in [38].

The following figures depict a fracture surface and a damaged surface due to fretting of the different microstructures for stress amplitudes of 300 MPa and 350 MPa. Fig. 6.20 shows the fracture and fretting damaged surface of a V-shape mill-annealed specimen for a stress amplitude of 300 MPa. The crack initiation occurred in the middle of the contact due to fretting loading. Fig. 6.21 shows the fracture surface of a V-shape mill-annealed material at a stress level of 350 MPa. In this case, multiple cracks initiated along the damaged fretting surface.

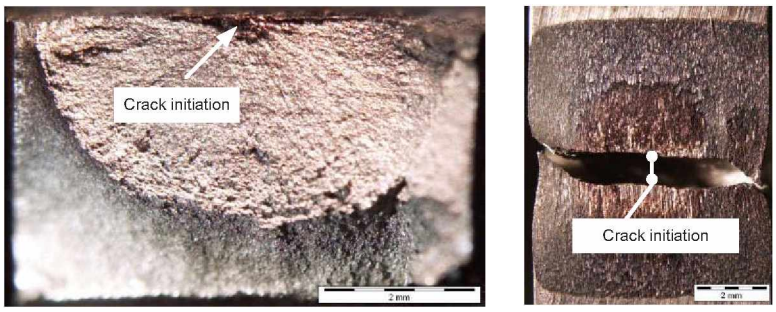

Fig. 6.20: Fracture and fretting damaged surface of a V-shape mill-annealed specimen at 300 MPa

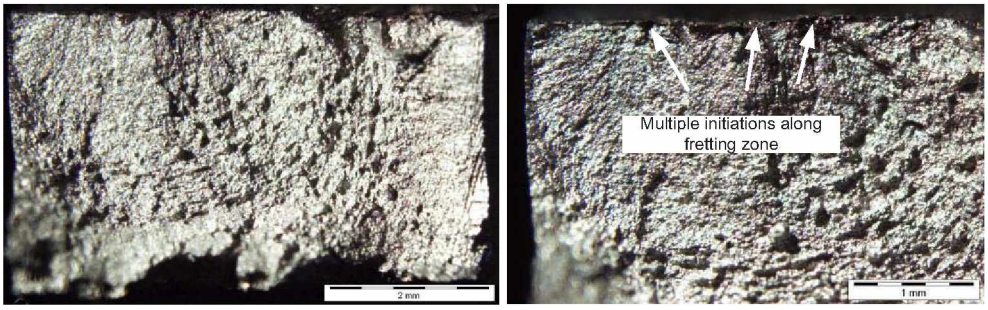

Fig. 6.21: Fracture surface of a V-shape mill-annealed specimen at 350 MPa, overview (l) and detail ®

Fig. 6.22 depicts the fracture surface of the recrystallization-annealed material with multiple crack initiations for a stress amplitude of 300 MPa.

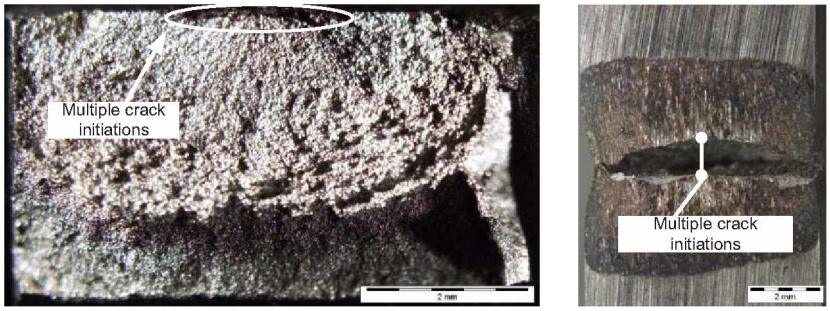

Fig. 6.22: Fracture and fretting damaged surface of a recrystallization-annealed specimen at 300 MPa

Fig. 6.23 shows the fracture and fretting damaged surface of a solution treated specimen for a stress amplitude of 300 MPa. The crack initiations occurred at two different levels.

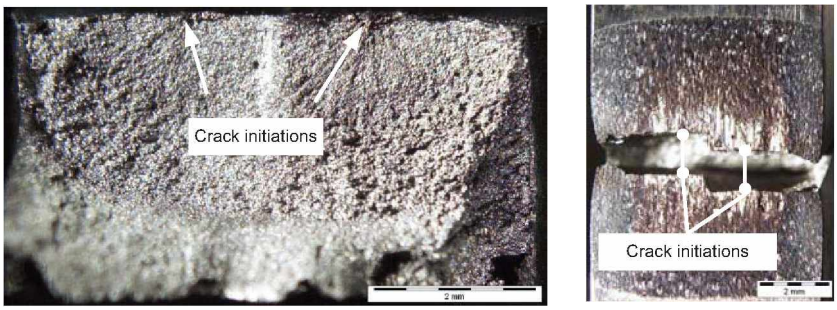

Fig. 6.23: Fracture and fretting damaged surface of a solution treated specimen at 300 MPa

Fig. 6.24 shows the fracture and fretting damaged surface of a beta-annealed microstructure with the crack initiation site marked with an arrow. It was observed, that the fatigue fracture surface is essentially rougher compared to the other microstructures.

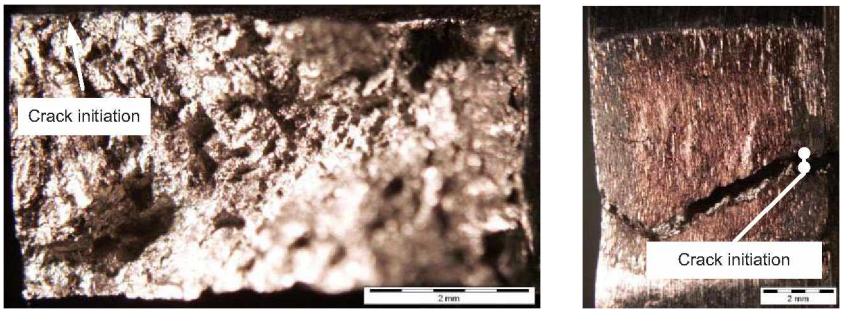

Fig. 6.24: Fracture and fretting damaged surface of a beta-annealed specimen at 300 MPa

Fig. 6.25 shows the fracture and fretting damaged surface of a solution treated polymer quenched material for a stress level of 350 MPa. Cracks initiated at both fretting damaged sides of the specimen.

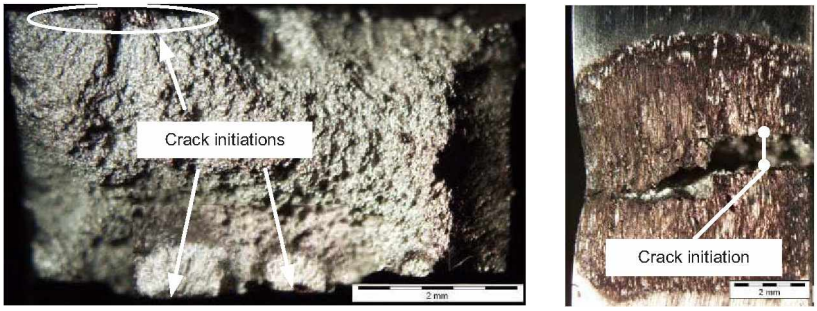

Fig. 6.25: Fracture and fretting damaged surface of a solution treated polymer-quenched specimen at 350 MPa

6.2.2. Influence of pressure

Fretting fatigue tests were performed with two different Hertzian contact pressures between pads and fretting fatigue specimen, namely 218 MPa and 267 MPa, respectively. The aim was to determine the influence of contact pressure on fretting fatigue strength. Three different materials were analyzed, namely pancake mill-annealed, V-shape mill-annealed and solution treated polymer-quenched. Fig. 6.26 shows the determined fretting fatigue results.

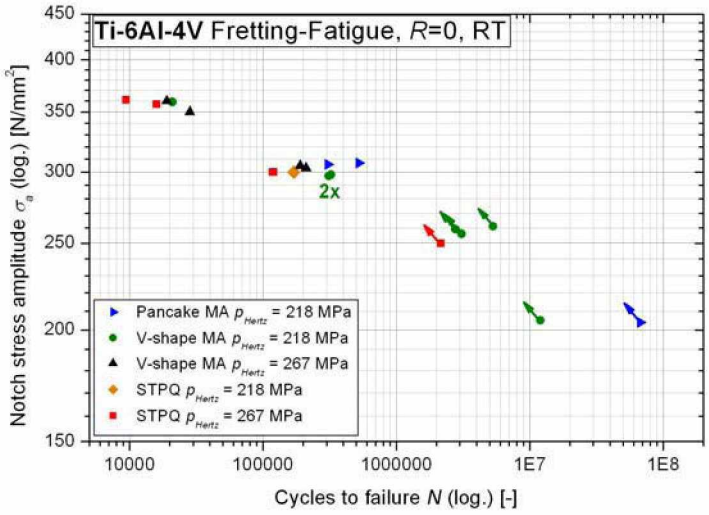

Fig. 6.26: Fretting fatigue tests with two different contact pressures

The comparison of fretting fatigue test results (ζ_a = 300 MPa) for low (218 MPa) and high (267 MPa) contact pressures reveals for both microstructures V-shape mil-annealed and solution treated polymer-quenched, that the fretting fatigue life decreases by a factor of 1.5 with increasing contact pressure. The pancake mill-annealed material shows for the low contact pressure the highest fretting fatigue strength.
The fretting fatigue specimens tested at lower stress amplitudes of 200 MPa and 250 MPa failed due to plain fatigue fracture. Fretting does not affect the fatigue strength at these stress levels. These results are discussed later in chapter 6.4.

6.2.3. Discussion

Fretting fatigue tests were carried out, to determine the influence of microstructure and contact pressure on fretting fatigue strength.
It was observed that the recrystallization-annealed microstructure has the lowest fretting fatigue strength. It can be assumed that the crack initiation and crack growth of the recrystallization-annealed microstructure has a anomalous behavior in comparison to the other microstructures. Oberwinkler B. [38] observed in his work, that the recrystallization-annealed microstructure exhibits a relatively large portion of longer cracks at the initiation phase compared to the other microstructures, if no residual compressive stresses are present. Surface inspections showed more and longer fretting fatigue cracks at the fretted surface for the recrystallization-annealed microstructure compared to other microstructures (cf. Fig. 6.27). It has to be mentioned that the existence of a (α+β)-phase has possibly an influence on the crack initiation as well as on the fretting fatigue strength. Venkatesh et al. [50] investigated fretting fatigue tests with similar microstructures of Ti-6Al-4V. They observed no essential influence of microstructure on fretting fatigue strength. Jin and Mall [24] as well as Lee and Mall [29] produced at analogical conditions similar results for a solution treated microstructure.
Furthermore it was determined that the fretting fatigue strength decreases with increasing contact pressure. This ties in well with the experimental data of Venkantesh et al. [50] and Nakazawa [35].

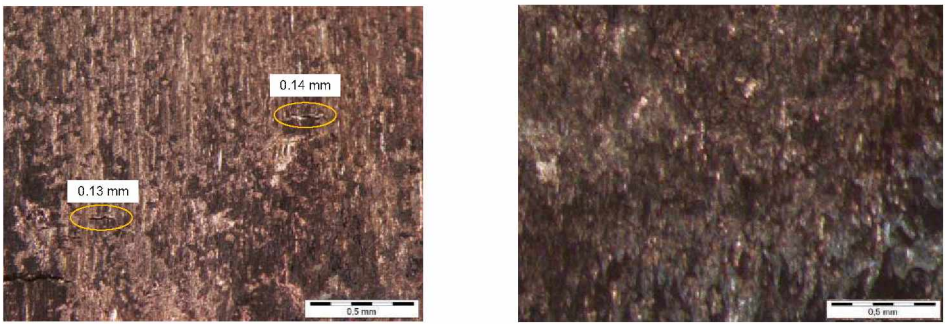

Fig. 6.27: Fretted surface of a recrystallization-annealed (l) and solution treated polymer-quenched material (r), ζ_a = 300 MPa, p_{Hertz} = 218 MPa

The analyses of the fretting damaged surfaces revealed that the contact between pad and surface is not uniform for the whole contact region. A most fretted region was identified for all specimens. It can be assumed that this is the region of full contact. The fretting fatigue cracks initiated at or near the outer borders of this region (cf. Fig. 6.28).

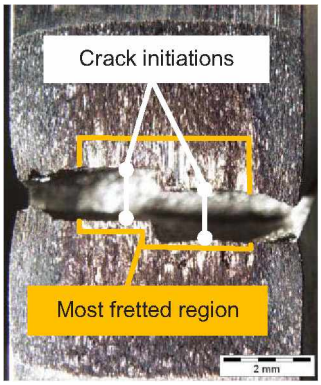

Fig. 6.28: Fretting damaged surface of a solution treated specimen

6.3. Influence of testing frequency and temperature

The influence of the testing frequency and consequently temperature was also analyzed in this thesis. Fretting wear tests were performed at a frequency of 20 Hz and fretting fatigue tests were performed at a frequency of 57 Hz. All tests were thereby performed with the same relative slip amplitudes.

Therefore, the fretting fatigue loading was simulated with the aid of finite element analysis in the Abaqus© software tool at different stress amplitudes for the determination of the relative slip amplitude between pads and specimen. Fig. 6.29 shows the model of the specimen geometry with the displacement distribution at a stress amplitude of 350 MPa. The used element type was an eight-node brick element C3D8R. The displacement distribution was readout with the aid of "paths".
Fig. 6.30 shows the simulated results at the stress levels 300 MPa and 350 MPa. The simulated results of the relative displacement amplitudes, for all tested stress amplitudes, are given in Tab. 6.2.

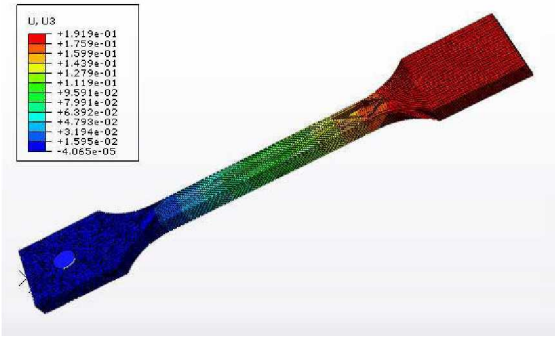

Fig. 6.29: Simulated model of the fretting fatigue specimen in Abaqus©

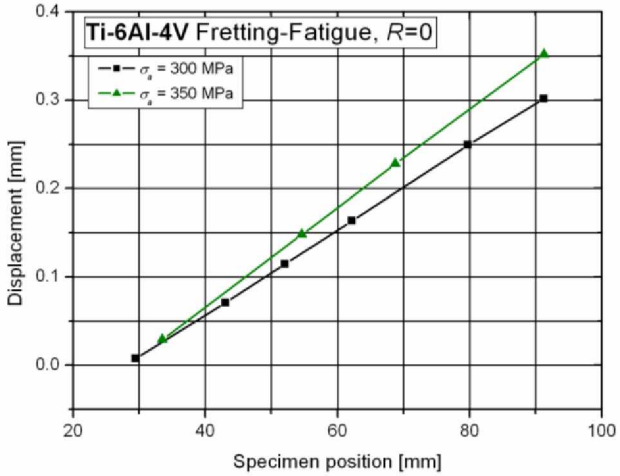

Fig. 6.30: Simulated results of the displacement along the specimen

Notch stress amplitude ζ_a [MPa]	Relative displacement amplitude δ_a [µm]
350	87.5
300	75
250	62.5
200	50

Tab. 6.2: δ_a for different ζ_a at the contact between specimen and pads

For both fretting wear and fretting fatigue tests, the temperature was measured. The temperature measurements were performed with a thermo element at the pad, near the contact region.

Fig. 6.31 (l) shows the measured temperature during the fretting fatigue test for a Hertzian contact pressure of 218 MPa at the stress levels 300 and 350 MPa. The measured temperature at the stress level of 300 MPa increases fast at the first twenty-thousand cycles and changes slight during the fretting fatigue test, in the range between 120 and 140°C. At the stress level of 350 MPa, an unexpected temperature was measured, which is lower compared to the stress level of 300 MPa. The measured temperature increases at the first cycles to a maximum of 130°C and decreases further to 120°C.

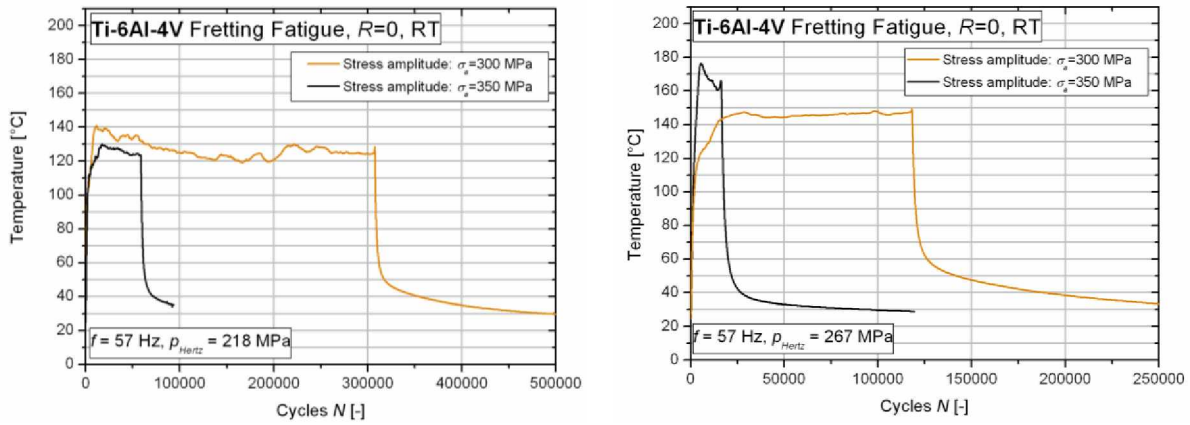

Fig. 6.31: Temperature profile versus fretting fatigue cycles for p_{Hertz}= 218 MPa (l) and p_{Hertz}= 268 MPa (r)

For the observation of the influence of pressure on the temperature distribution, measurements were also performed during fretting fatigue tests with a contact pressure of 267 MPa (Fig. 6.31 (r)). It was observed that the temperature increases with increasing contact pressure. At a stress amplitude of 300 MPa, the temperature increases fast during the first twenty-thousand cycles and reaches a plateau of 145°C. Whereas, at a stress amplitude of 350 MPa, the temperature increases rapidly to a maximum of 175°C, and decreases subsequently to 160°C.

The temperature distribution at a stress level of 250 MPa and with a Hertzian pressure of 218 MPa is depicted in Fig. 6.32. The mean temperature during the fretting fatigue test is 67°C. It can be concluded that the temperature decreases with decreasing stress amplitude.

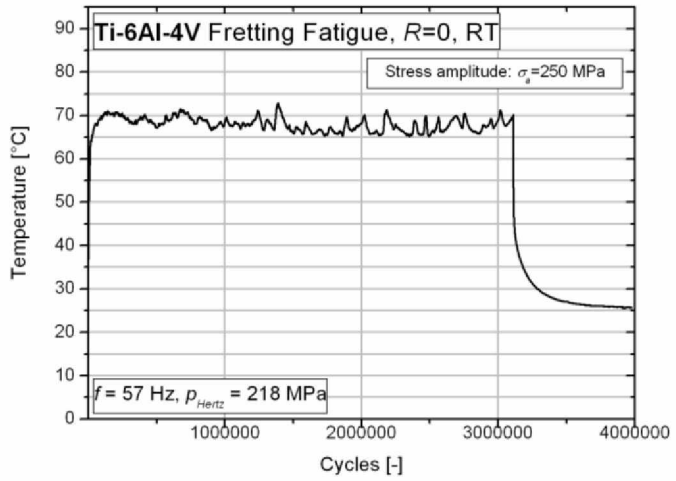

Fig. 6.32: Temperature profile versus fretting fatigue cycles (p_{Hertz}=218 MPa, ζ_a=250 MPa)

The measured temperature for fretting wear testing was recorded at the relative slip amplitude of 87.5 µm. This relative slip amplitude corresponds to the stress level of 350 MPa at fretting fatigue testing. The measured temperature lies in the range between 70 and 80°C, as shown in Fig. 6.33.
It was observe, that the frequency has a significant influence on the contact temperature. An increase of testing frequency leads to an elevated contact temperature. For equivalent relative slip amplitudes between specimen and pads during fretting wear (20 Hz) and fretting fatigue (57 Hz) tests, the temperature differs by a factor of more than two.

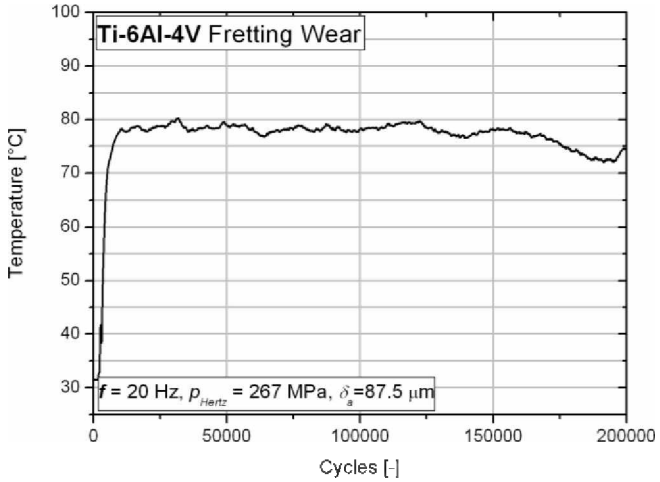

Fig. 6.33: Temperature profile versus fretting wear cycles

Fretting wear (f = 20 Hz) and fretting fatigue (f = 57 Hz) test were performed for identical relative displacement amplitudes (δ_a = 75 µm) and Hertzian pressure (p_{Hertz} = 267 Hz) and interrupted at the same number of cycles (N = 20,000). These tests were performed for the solution treated, solution treated polymer-quenched, recrystallization-annealed and V-shape mill-annealed microstructures. For both 20 Hz and 57 Hz tests, 3D-topography measurements of the fretted surfaces were done; Fig. 6.34 and Fig. 6.35.

Fig. 6.34 shows the 3D-topography for different microstructures at a testing frequency of 20 Hz. It was observed, that the arithmetic mean height lies in a small scatter range between 2.8 and 3.3 µm, for the solution treated, solution treated polymer quenched and recrystallization-annealed microstructures. Only the V-shape mill-annealed surface roughness has a higher arithmetic mean height of 4.4 µm.

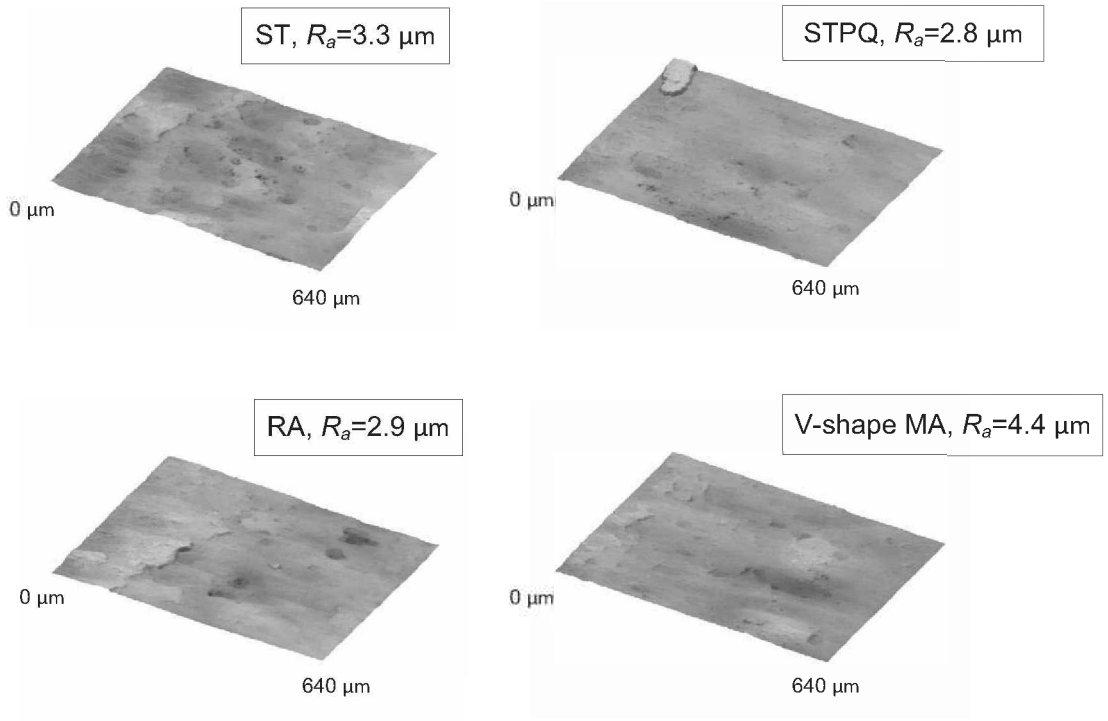

Fig. 6.34: 3D-topography of the fretted surfaces of different microstructures for f = 20 Hz

Fig. 6.35 shows the 3D-topography of the fretted surfaces of different microstructures at a testing frequency of 57 Hz. The arithmetic mean height of the fretted surfaces is two times higher than for the lower testing frequency of 20 Hz. It can be concluded that the surface roughness increases dramatically due to the increased local temperature, caused by the higher testing frequency.

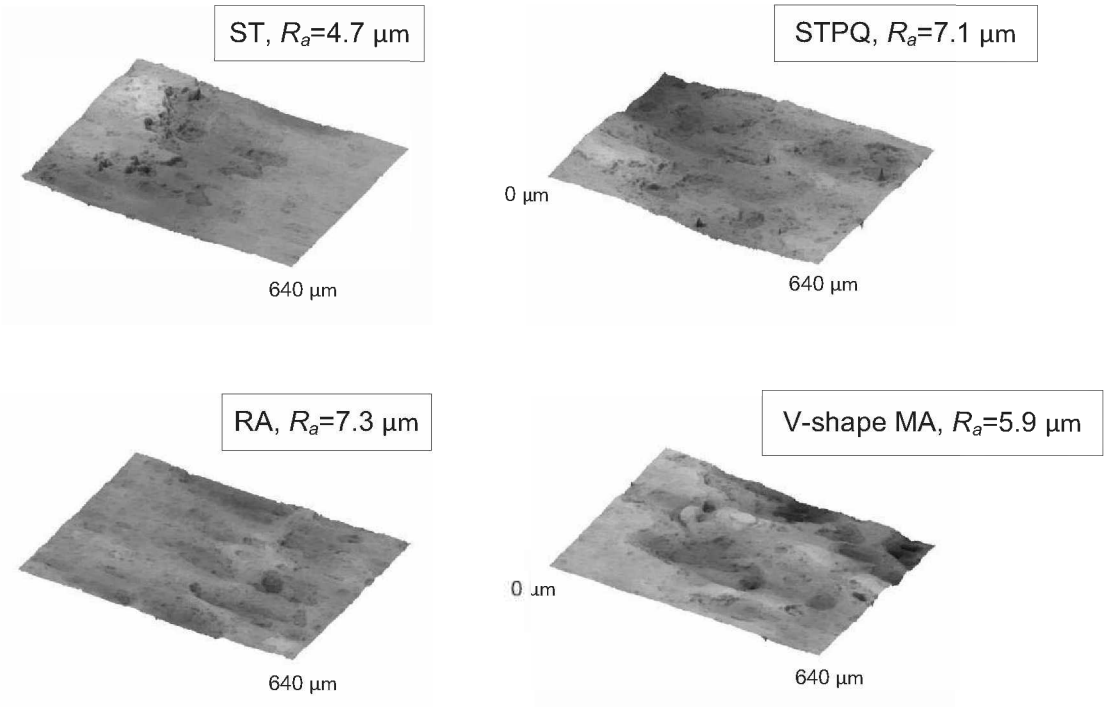

Fig. 6.35: 3D-topography of the fretted surfaces of different microstructures for f = 57 Hz

The surface topography of fretting damaged surfaces is hence influenced by temperature. it can be assumed that the wear behavior is also varying at different testing frequencies and consequently temperatures.

It was observed at fretting wear tests with a testing frequency about 20 Hz, that the difference of wear mass between solution treated polymer-quenched, recrystallization-annealed and V-shape mill-annealed microstructure, amounts 35%, whereas the solution treated microstructure exhibits a two-times lower wear mass. This means that the solution treated microstructure has a better fretting wear resistance compared to the other microstructures.
At a frequency of 57 Hz, the wear mass increases essentially compared to the fretting wear tests with 20 Hz, cf. Fig. 6.36. The wear mass increases by a factor of six for the solution treated microstructure. The maximum difference of wear mass between the four microstructures was determined to be approximately 20%. It can be assumed, that the influence of microstructure on wear disappears, due to the increased local temperature.

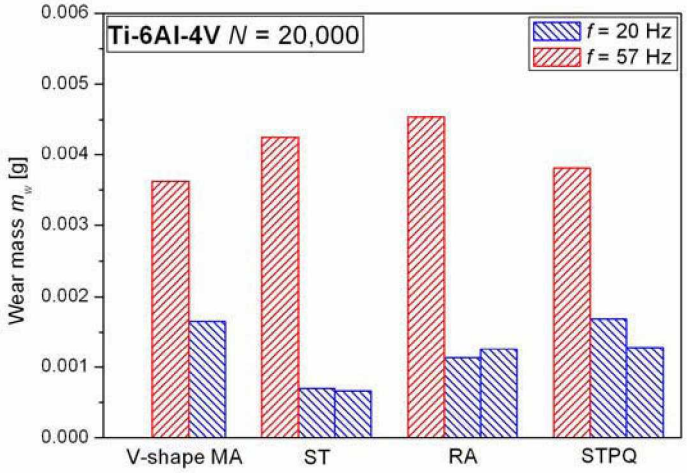

Fig. 6.36: Influence of frequency on wear mass

For the evaluation of the wear loss in respect of frequency, relative slip amplitude and fretting cycles, all fretting tests of the mill-annealed microstructure with a Hertzian pressure of 267 MPa are compared in Fig. 6.37. It was determined that the wear mass increases slightly with increasing temperature and increasing relative slip amplitude.

Fig. 6.37 (r) shows a single-logarithmic exposition of the fretting results. This distribution shows that the relative slip amplitude has a low influence on wear mass up to 1E6 fretting cycles. It can be assumed, that with increasing fretting cycles the influence of relative slip amplitude increases more and more. However, the main influence on the wear mass are the fretting cycles.

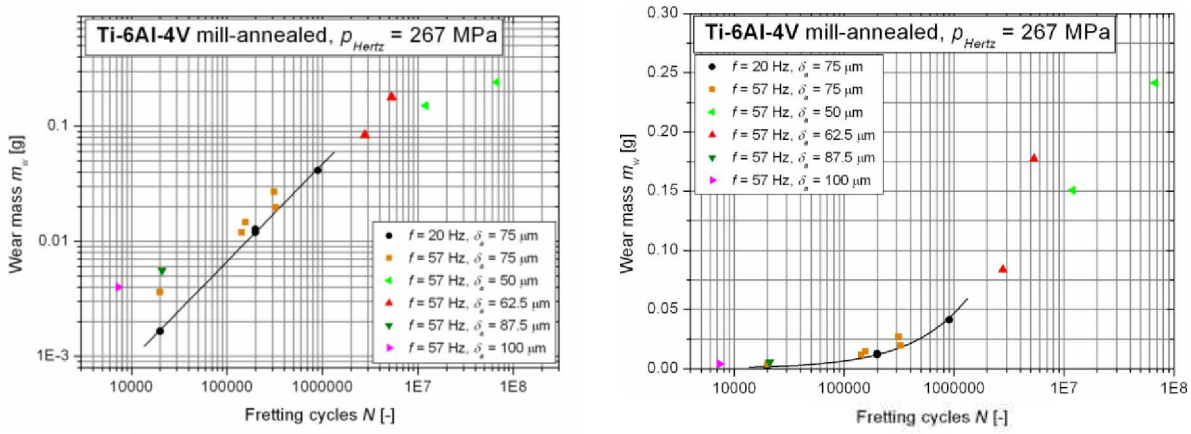

Fig. 6.37: Wear loss for both frequencies versus fretting cycles

6.4. Modeling of the fretting fatigue strength

The aim in this chapter is the estimation of the fretting fatigue strength of Ti-6Al-4V, with existing models according to Oberwinkler B. [38]. For the evaluation of the fretting fatigue damage it is important to characterize the contact conditions. Therefore the contact conditions at the beginning of the fretting fatigue tests and at the fretting fatigue fracture, were simulated with the aid of finite element analysis in the Abaqus© software tool.

For reducing the simulation time quarter a 2D-model was used for the simulation of the fretting fatigue contact. Fig. 6.38 shows a cylinder plane contact at the initial contact condition.

Fig. 6.38: Quarter 2-D-model of the fretting fatigue contact at the initial condition

For the definition of the interacting contact between pad and specimen a normal behavior "Hard Contact" and tangential behavior with a corresponding friction coefficient was used. The specimen surface was defined as "Master-surface" and the pad surface as "Slave-surface". The used meshing element type was eight-node plain strain elements, CPE8R. The fineness of the mesh at the contact was very high, with an element size of 0.004 mm (cf. Fig. 6.39).

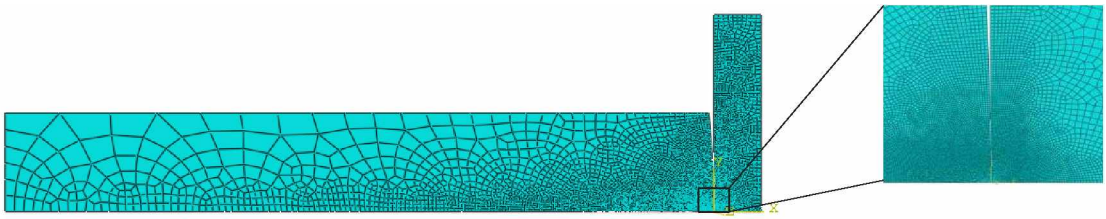

Fig. 6.39: Mesh of the cylinder plane contact

Two steps were performed in the simulation. In the first step, the normal load between pad and specimen was applied. In the second step, the fretting fatigue specimen was loaded with the stress amplitude. The simulated distribution of the Mises equivalent stresses for the first step with a normal load of 1500 N is shown in Fig. 6.40. The second step, with additionally applied stress amplitude of 300 MPa, is shown in Fig. 6.41. It was observed, that the stress distribution changes essentially in the contact range between the first and second step.

Fig. 6.40: Misies equivalent stress distribution at a normal load of 1500 N

Fig. 6.41: Mises equivalent stress distribution at a normal load of 1500 N and stress amplitude of 300 MPa

Two different normal loads between specimen and pads, 1000 N and 1500 N were used for the fretting fatigue tests. The resulting pressure was calculated with the theory according to Heinrich Hertz. To verify the simulation the calculated and simulated results were compared for the cylinder plane contact. For the normal load of 1500 N, the peak contact pressure according to Hertz is 267 MPa, and the simulated peak pressure amounts 268 MPa. The simulated and calculated pressures are hence identically. Fig. 6.42 show the pressure distribution of the simulated cylinder plane contact.

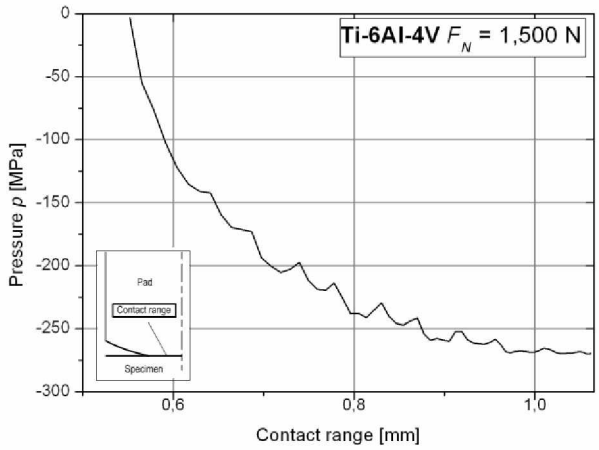

Fig. 6.42: Simulated pressure distribution in the contact range for the used cylinder plane contact

The contact surface is changing during the fretting fatigue test due to the wear loss. A change from cylinder plane contact to flat contact occurs. It is therefore necessary to simulate the different contact conditions. After the fretting fatigue tests, the worn surface area of all pads was measured with a light optical stereo microscope (cf. Fig. 6.43). This was the basis for the approximation of the geometry of the contact for different contact conditions. Fig. 6.44 shows a contact configuration for the simulation of a worn surface contact. The used finite element size in the contact range amounts 0.0014 mm.

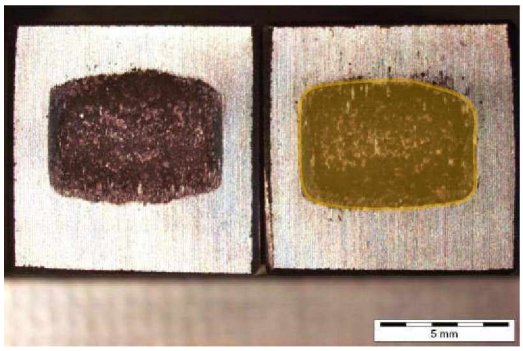

Fig. 6.43: Worn surface of pads

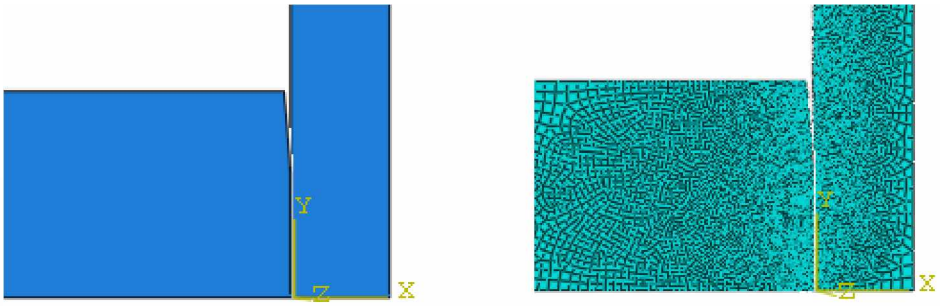

Fig. 6.44: Contact configuration of a worn surface

Fig. 6.45 shows the Mises equivalent stress distribution for an applied normal load of 1500 N. It was observed that the maximum stress concentration shifts to the edge of the contact.

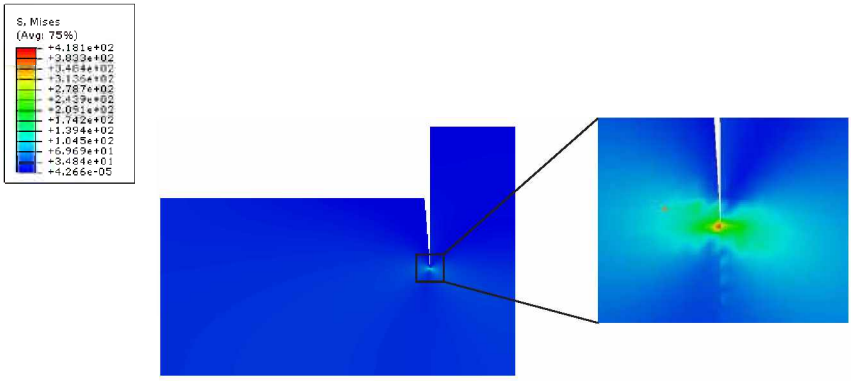

Fig. 6.45: Mises equivalent stress distribution with applied normal load of 1500 N at worn surface contact configuration

The applied stress amplitude of the performed fretting fatigue tests lies between 200 and 400 MPa. Fig. 6.46 shows the simulated results of the equivalent Mises stress distribution of a contact configuration with a normal load of 1500 N and at the stress level of 300 MPa. The maximum stress occurs at the edge of the contact between pad and specimen.
The comparison of the simulated results for constant normal load at different stress amplitudes shows, that the stress peak at the edge increases with increasing amplitude (cf. Fig. 6.46 to Fig. 6.48).

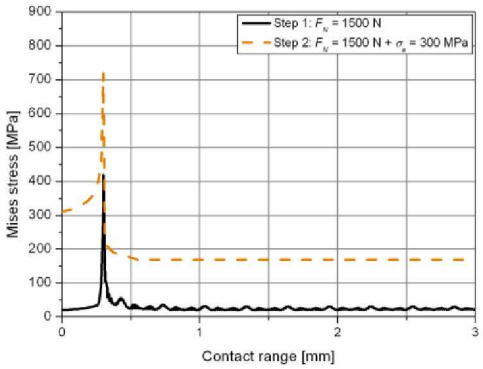

Fig. 6.46: Mises equivalent stress distribution in the contact range at the stress amplitude of 300 MPa

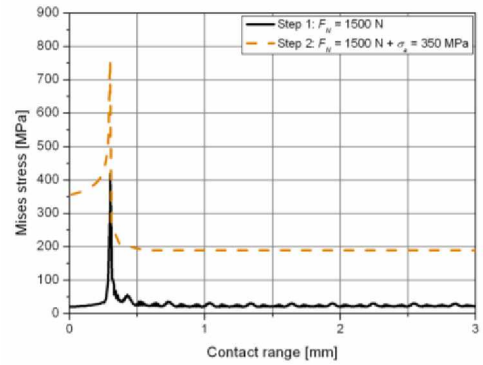

Fig. 6.47: Mises equivalent stress distribution in the contact range at the stress amplitude of 350 MPa

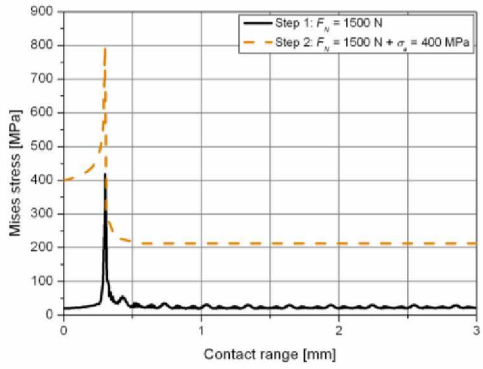

Fig. 6.48: Mises equivalent stress distribution in the contact range at the stress amplitude of 400 MPa

Fig. 6.49 shows the Misses stress distribution for a contact condition at the stress level of 250 MPa. At this level the curvature of the pad is worn complete and lies with the whole surface on the fretting fatigue specimen. The maximum Mises stress (240 MPa) occurs at the edge of the contact.

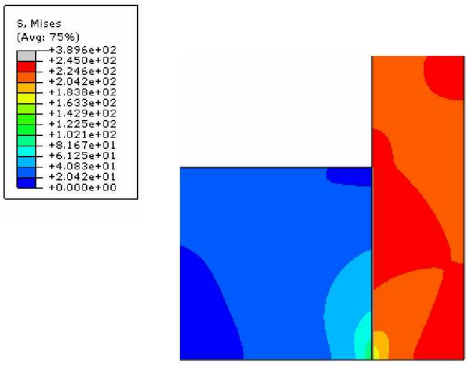

Fig. 6.49: Mises stress distribution of a contact with normal load 1500 N and stress amplitude of 250 MPa

As mentioned before, fretting fatigue tests were conducted for two normal loads between pads and specimen. The simulated results for both normal loads and for all performed fretting fatigue stress levels are summarized in Tab. 6.3.

Normal load F_N = 1500 N			
ζ_a	Step 1 ζ_{min}	Step 2 ζ_m	ζ_a
400	-177	569	746
350	-177	530	707
300	-177	491	668
250	-68	240	308
Normal load F_N = 1000 N			
ζ_a	Step 1 ζ_{min}	Step 2 ζ_m	ζ_a
400	-118	557	675
350	-118	516	634
300	-118	476	594
250	-39	234	273

Tab. 6.3: Simulated results for all conducted fretting fatigue stress levels

It has to be mentioned that the determined maximum local stresses were averaged between two finite elements. The averaging length was chosen to approximate the grain size of the analyzed material. Therefore, the stress values between two middle nodes and one edge node were averaged (cf. Fig. 6.50). This was done for both, step 1 where only the normal load is applied and step 2 where the normal load and specimen loading is applied. The occurring stresses in step 1 represent the minimum stress ζ_{min} of the fatigue load. The minimum principle stress at this configuration is negative. Therefore, the Mises equivalent stress was also assumed to be negative. The stress of step 2 are the occurring mean stresses ζ_m The difference of mean stress and minimum stress represents the local stress amplitude ζ_a.

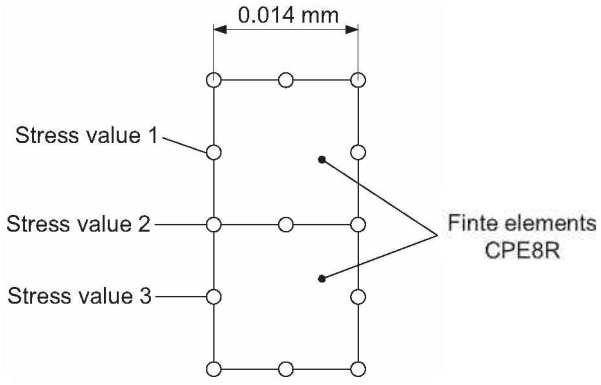

Fig. 6.50: Two finite elements CPE8R

The simulation results show that excessively high local stresses occur. This means that a local low cycle fatigue (LCF) loading is present due to the contact between pads and specimen, whereas the specimen has a global high cycle fatigue (HCF) loading. However, the crucial loading is the LCF loading in the contact range, because the occurring stresses are much higher in the contact region.
It should be noted, that in the stress amplitude range between 300 and 400 MPa, the specimens fractures due to fretting crack initiation, whereas between the range 200 and 250 MPa the specimens fail due to plain fatigue loading.

Fig. 6.51 shows the fracture surface of a specimen at a stress level of 200 MPa. The crack initiation occurred at the edge of the specimen, outside of the fretted region. Fig. 6.52 shows the fretted surface in the contact region between pads and specimen. The wear of the specimen is enormous. The whole worn height amounts for this specimen 0.4 mm. Despite high wear loss in the contact, the specimen fractures due to fatigue loading.

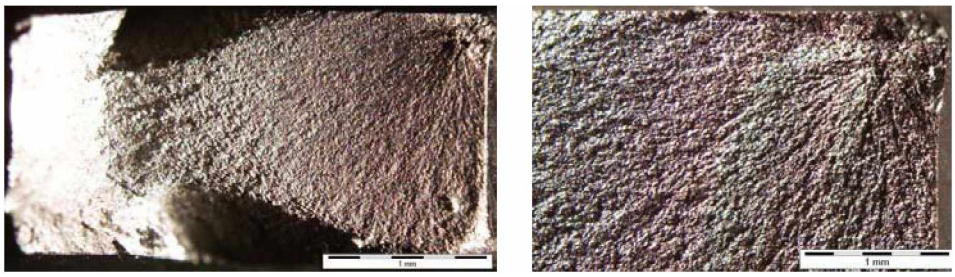

Fig. 6.51: Fracture surface of a fretting fatigue specimen at a stress level of 200 MPa

Fig. 6.52: Fretted surface of a specimen at a stress level of 200 MPa

6.4.1. Estimation of the fretting fatigue strength

The fretting fatigue strength was calculated for the high cycle and finite life fatigue region of Ti-6Al-4V, according to Oberwinkler B. [38]. For the estimation of the low cycle fatigue strength, the simulated results were used for calibration. The modeled fretting fatigue strengths compared with the conducted results are presented in Fig. 6.53.

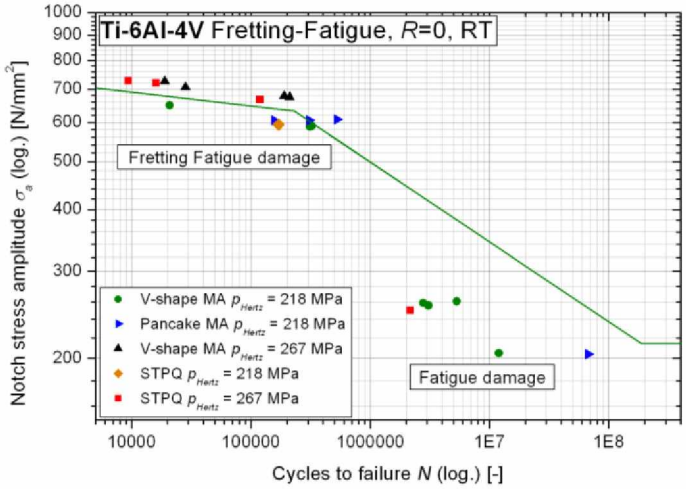

Fig. 6.53: Estimated model for the fretting fatigue strength of Ti-6Al-4V

The high cycle and finite life fatigue strength were calculated in respect of all influences, such as microstructure, relative stress gradient, mean stress, multi-axial loading, flaws, surface state and temperature. The low cycle fatigue strength was calibrated with the simulated results of Tab. 6.3. For verification of the model, the necessary temperature to achieve the calibrated LCF strength was calculated. It can be compared with the measured temperature of the fretting fatigue tests.

The calculation of the temperature was done with an existing model according to Oberwinkler B. [38], with the parameters at the intersection point of the LCF and finite life curve. The calculated temperature amounts 110°C, whereas the measured data at this point exhibits a temperature of circa 140°C. A deviation of 20% exists between estimated and real temperature.

6.4.2. Discussion

Simulation models of the contact configuration at the beginning of the fretting fatigue test and at fretting fatigue fracture were drafted. For this simulated models two steps were performed. In the first step, the normal load between pad and specimen was applied. In the second step, the fretting fatigue specimen was loaded with the stress amplitude. It was observed, that the stress distribution changed essentially in the contact range between the first and second step. Furthermore, it was concluded that due to the changing of the surface during fretting fatigue testing, the maximum stress concentration shifted from the middle to the edge of the contact, whereas the peak contact stress decreases with increasing contact area between pad and specimen. The comparison of the simulated results for constant load at different stress amplitudes showed, that the stress peak at the edge increases with increasing stress amplitude. Furthermore, the simulated results showed that excessively high local stresses occur. This means that a local low cycle fatigue (LCF) loading is present due to the contact between pads and specimen, although the specimen has a global high cycle fatigue (HCF) loading. However, the crucial loading is the LCF loading in the contact range, because the occurring stresses are much higher in the contact region.

The fretting fatigue strength was calculated for the high cycle and finite life fatigue region with existing models according to Oberwinkler B. [38]. The low cycle fatigue strength was calibrated with the simulated results, Tab. 6.3. For verification of the model, the necessary temperature to achieve the calibrated LCF strength was calculated. A deviation of 20% was determined between measured temperature (140°C) and calculated temperature (110°C). This can be attributed to the fact that the low cycle fatigue region is a rough estimation and the models according to Oberwinkler B. [38] are based on cyclic stabilized strain-controlled fatigue data. Furthermore, Mises equivalent stresses were used for the estimation of the low cycle fatigue strength,. It has to be mentioned that Mises stresses are usually used for the estimation of the high cycle fatigue strength.

Fretting fatigue specimen tested at lower stress levels (200 to 250 MPa) failed due to plain fatigue loading. Crack initiation might take place at the beginning of the fretting fatigue tests due to the initial cylinder plane contact with high local stresses. Nevertheless, the crack propagation is too slow owing to the low stress amplitudes and initiated cracks are eliminated by fretting wear. The wear losses lead to flat flat contact with a large contact region and relatively low contact stresses. However, the cross section of the specimen is decreased due to these wear losses and leads to increased plain fatigue stresses.
A deviation of experimental and modeled fretting fatigue strength was observed. This can be attributed to the fact that the increased stress amplitude due to decreasing cross section was neglected and the disregard of the edge effect, cf. [39].

7. Conclusion

- The micro-hardness of different microstructures of Ti-6Al-4V was measured and evaluated. It was observed that the solution treated microstructure has the highest micro-hardness.

- Fretting wear tests were performed under several contact conditions. It was determined, that the fretting wear mass increases with increasing fretting cycles or relative slip amplitude, whereas no influence of the contact pressure was observed. A linear relation was found between wear mass and dissipated energy.

- The influence of contact pressure and relative slip amplitude on friction coefficient was investigated. It was observed that the friction coefficient decreases with decreasing slip amplitude. A slight increase of the friction coefficient was determined for increasing contact pressure.

- The damaged regions of the fretting wear specimen were analyzed with a light optical a confocal laser scanning microscope. It was observed that the surface degradation increases with higher relative slip amplitude.

- The wear energy density factor was used for comparison of fretting wear results. The wear energy density characterizes, which friction energy is essential to remove a defined wear volume.

- The influence of microstructure on fretting wear was investigated for solution treated, recrystallization-annealed, solution treated polymer-quenched and mill-annealed microstructures of Ti-6Al-4V. It was observed that the solution treated microstructure has the highest wear resistance.

- The fretting fatigue behavior of Ti-6Al-4V was investigated with respect to the influence of microstructure. It was observed that the recrystallization-annealed microstructure has the lowest and the V-shape mill-annealed microstructure has the highest fretting fatigue life. In general, it was determined that fretting conditions essentially reduce the fatigue life in comparison to plain fatigue data.

- Fretting fatigue tests were performed with different contact pressures. It was observed that the fretting fatigue strength decreases with increasing contact pressure.

- The friction-caused heating was analyzed in respect of contact pressure and relative slip amplitude. It was determined that the temperature increases with increasing contact pressure or relative slip amplitude.

- The influence of testing frequency and hence contact temperature on fretting behavior of Ti-6Al-4V was investigated. The fretting damaged surfaces were analyzed at different temperatures. It was determined that the roughness of the fretted surface increases with increasing temperature. Furthermore, it was observed that the influence of microstructure on wear is getting lost with increasing temperature.

- Finite element analyses of the contact configurations for fretting fatigue testing were performed. Due to the changing of the surface during fretting fatigue testing, it was observed that the maximum stress concentration shifted from the middle to the edge region of the contact, whereas the peak contact stress decreases with increasing contact area between pad and specimen. Furthermore, it was observed that the stress peak increases with increasing stress amplitude.

- It was observed that the occurring local equivalent stresses between pads and specimen are crucial for the fretting fatigue damage. Therefore, a model for the fretting fatigue strength of Ti-6Al-4V was developed based on existing fatigue models.

8. Outlook

- Additional fretting fatigue tests with different contact pressures in combination with different stress levels should be conducted to gain a better understanding for the influence of the contact configurations on the fretting fatigue strength.

- For the verification of the investigated influence of microstructure on fretting wear, additional tests with more fretting cycles to failure should be performed and analyzed.

- The influence of surface state modifications such as shot-peening or nitriding, coatings and lubricants on fretting fatigue strength would be interesting.

- The applicability of different damage parameters summarized in this diploma thesis for the estimation of the fretting fatigue life should be proofed.

- It would be interesting to implement a real fretted surface, measured with 3D-scanning, in a finite element contact simulation.

9. References

[1] Archard J. F.:"Contact and rubbing of flat surfaces", Journal of Applied Physics, vol. 24, pp. 981-988, 1953

[2] ASM Handbook, Vol.13 "Corrosion", ASM International, 1987

[3] Bellows R.S., Muju S., Nicholas T.:"Validation of the step test method for generating Haigh diagrams for Ti-6Al-4V", International Journal of Fatigue (UK). Vol. 21, no. 7, pp. 687-697. Aug. 1999

[4] Bhushan B.:"Modern tribology handbook 1, Principles of tribology", 1th edition, CRC Press, Boca Raton, 2001, ISBN 0-8493-8403-6

[5] Bhushan B.:"Principles and applications of tribology", 1.Tribology, John Wiley & Sons, New York, 1999, ISBN 0-471-59407-5

[6] Cadario A.:"Fretting Fatigue - A Literaure Survey", Report 385, KTH Royal Institute of Technology, Stockholm, Sweden, 2005

[7] Chambon L., Journet B.:"Modelling of fretting fatigue in a fracture-mechanics framework", Tribology International, Vol. 39, pp. 1220-1226, 2006

[8] Conner B.P., Hutson A.L., Chambon L.:"Observation of fretting fatigue micro-damage of Ti-6Al-4V", Wear, Vol. 255, pp. 259-268, 2003

[9] Dick T.:"Mod´elisation multi´echelle du ph´enom`ene de fretting dans le contact aube–disque",ECOLE DES MINES DE PARIS, College doctoral, 2006

[10] Dobromirski J.M.:"Variables of Fretting Process: Are There 50 of Them?", Standardization of Fretting Fatigue Test Methods and Equipment, ASTM Publication, STP 1159, Philadelphia, pp. 60-66, 1992, ISBN 0-8031-1448-6

[11] Fouvry S., Duo P., Perruchaut Ph.:"A quantitative approach of Ti-6Al-4V fretting damage: friction, wear and crack nucleation", Wear, Vol. 257, pp. 916-929, 2004

[12] Fouvry S., Kapsa P., Vincent L.: "Quantification of fretting damage", Wear, Vol. 200, S. 186-205, 1996

[13] Fu Y., Loh N.L., Batchelor A.W., Liu D., Zhu X., He J., Xu K.:"Improvement in fretting wear and fatigue resistance of Ti-6Al-4V by application of several surface treatments and coatings", Surface & Coatings Technilogy, Vol. 106, pp. 193-197, 1998

[14] Godor I.: "Skriptum zur Tribologie für Maschinenelemente", Department Product Engineering, Chair of Mechanical Engineering, MU Leoben, WS 2007/08

[15] Golden P.J., Hutson A., Sundaram V., Arps J.H.:"Effects of surface treatments on fretting fatiuge of Ti-6Al-4V", International Journal of Fatigue, Vol. 29, pp. 1302-1310, 2007

[16] Grote K.-H., Feldhusen J.:"Dubbel, Taschenbuch für den Maschinenbau", 22. Auflage, Springer-Verlag Berlin, Heidelberg, New York 2007, ISBN 978-3-540-49714-1

[17] Hills D.A., Nowell D.:"Mechanics of Fretting Fatigue", Volume 30, Kluwer Academic Publisher, Dodrecht, 1994, ISBN 0-7923-2866-3

[18] Hines J.A., Lütjering G.:"Propagation of microcracks at stress amplitudes below the conventional fatigue limit in Ti-6Al-4V", Fatigue and Fracture of Engineering Materials and Structures (UK). Vol. 22, No. 8, pp. 657-665. Aug. 1999

[19] Hoeppner D.W.:"Mechanisms of Fretting Fatigue", Fretting Fatigue, ESIS 18 (Edited by R.B. Waterhouse and T.C. Lindley) 1994, Mechanical Engineering Publications, London, pp. 3-19

[20] Holm R.:"Electrical Contacts", Springer-Verlag, New York, 1946

[21] Hutchings I.M.:"Tribology: Friction and Wear of Engineering Materials – (Metallurgy&Materials Science Series)", I.Title, II.Series, Edward Arnold- A division of Hodder&Stoughton London, 1992, ISBN 0-340-56184

[22] Hutson A.L., Niinomi M., Nicholas T., Eylon D.:"Effects of various surface conditions on fretting fatigue behavior of Ti-6Al-4V", International Journal of Fatigue, Vol. 24, 1223-1234, 2002

[23] Iyer K.:"Peak contact pressure, cyclic stress amplitudes, contact semi-width and slip amplitude: relative effects on fretting fatigue life", International Journal of Fatigue, Vol. 23, pp. 193-206, 2001

[24] Jin O., Mall S.:"Influence of contact configuration on fretting fatigue behaviour of Ti-6Al-4V under independent pad displacement condition", International Journal of Fatigue, Vol. 24, pp. 1243-1253, 2002

[25] Jin O., Mall S., Sahan O.:"Fretting Fatigue behavior of Ti-6Al-4V at elevated temperature", International Journal of Fatigue, Vol. 27, pp. 395-401, 2005

[26] John A. Williams:"Wear and wear particles-some fundamentals", Cambrige University, Tribology International 38(10): 863-870

[27] Kapsa P., Fouvry S., Vincent L.:"Basic Principles of Fretting", Wear, Materials, Mechanisms and Practice, S.317-338, ISBN-13: 978-0-470-01628-2

[28] Lee H., Jin O., Mall S.:"Fretting fatigue of shot-peened Ti-6Al-4V at room and elevated temperatures", Fatigue Fracture of Engineering Materials and Structures, Vol. 26, pp. 767-778, 2003

[29] Lee H., Mall S.:"Investigation into effects and interaction of various fretting fatigue variables under slip-controlled mode", Tribology International, Vol. 39, pp. 1213-1219, 2006

[30] Lee H., Mall S., Sathish S., Blodgett M.O.:"Evolution of residual stresses in stress-free titanium alloy subjected to fretting fatigue", Materials Letters, Vol. 60, pp. 2222-2226, 2006

[31] Lee H., Shankar M., Allen W.Y.:"Fretting Fatigue behavior of shot-peened Ti-6Al-4V under seawater environment", Materials & Science and Engineering, A240, pp. 72-78, 2006

[32] Magaziner R. S., Jain V. K., Mall S.:"Investigation into wear of Ti-6Al-4V under reciprocating sliding conditions", Wear, vol. 267, pp 368-373, 2009

[33] Mall S., Namjoshi S.A., Porter W.J.:"Effects of microstructure on fretting fatigue crack initiation behavior of Ti-6Al-4V", Materials Science & Engeneering, A 383, pp. 334-340, 2004

[34] Maxian T. A., Brown T. D., Pederson D. R., Challaghan J. J.:"A sliding-distance-coupeld finite elemente formulation for polyethylene wear in total hip arthroplasty", Journal of Biomechanics, vol. 29, pp. 687-692, 1996

[35] Nakazawa K., Sumita K., Maruyama N:"Effect of Contact Pressure on Fretting Fatigue of Hifh Strength Steel and Titanium Alloy", Standardization of Fretting Fatigue Test Methods and Equipment, ASTM STP 1159, pp. 115-125, Philadelphia, 1992

[36] Nakazawa K., Sumita M., Maruyama N.: "Effect of relative slip amplitude on fretting fatigue of high strength steel", Fatigue & Fracture of Engineering Materials & Structures, Vol. 17, S. 751-759, 1994

[37] Navarro C., Munoz S., Dominguez J.: "On the use of multiaxial fatigue criteria for fretting fatigue life assessment", International Journal of Fatigue, Vol. 30, S. 32-44, 2008

[38] Oberwinkler B.:"Fatigue-Proof and Damage Tolerant Lightweight Design of Ti-6Al-4V Forgings", Doctoral Thesis, Montanuniversität Leoben, Chair of Mechanical Engineering, 2010

[39] Oberwinkler B., Riedler M., Eichlseder W.:"Importance of Residual Stresses and Surface Roughness Regarding Fatigue of Titanium Forgings", Journal of ASTM International, Vol. 7, No. 2, February 2010, Paper ID JAI102534 (PA)

[40] Petiot C., Vincent L., Dang Van K., Maouche N., Foulquier J., Journet B.: "An analysis of fretting fatigue failure combined with numerical calculations to predict crack nucleation", Wear, Vol. 181-183, S. 101-111, 1995

[41] Rajasekaran B., Ganesh Sundara Raman S.:"Plain fatigue and fretting fatigue behaviour of plasma nitrided Ti-6Al-4V", Material Letters, Vol. 62, pp. 2473-2475, 2008

[42] Reichhart M.: "Entwicklung einer Fretting-Fatigue-Prüfkonstruktion", Projektarbeit, Lehrstuhl für Allgemeinen Maschinenbau, Montanuniversität Leoben, 2007

[43] Reiser J.:"Entwicklung einer Untersuchungsmethodik zur Evaluierung des Fretting-Widerstandes", Montanuniversität Leoben, Chair of Mechanical Engineering, Diploma thesis, 2008

[44] Ren W., Mall S., Sanders J.H., Sharma S.K.:"Evaluation of coatings on Ti-6Al-4V substrate under fretting fatigue", Surface & Coatings Technology, Vol. 192, pp. 177-188, 2005

[45] Ruina A., Rudra Pratap:"Introduction to Statics and Dynamics", Oxford University Press, 2002

[46] Sauger E., Fouvry S., Ponsonnet L., Kapsa Ph., Martin J.M., Vincent L.:"Tribologically transformed structure in fretting", Wear, Volume 245, pp. 39-52, 2000

[47] Shaffer S.J., Glaeser W.A.:"ASM Handbook", The Material Information Society, vol.19, pp.321-330, Ohio, 1996

[48] Shepard M.J., Prevey P.S., Jayaraman N.:"Effects of Surface Treatments on Fretting Fatigue Performance of Ti-6Al-4V", 8th National Turbine Engine HCF Conference, Monterey, 2003

[49] Szolwinski M.P., Farris T.N.: "Mechanics of fretting fatigue crack formation", Wear, Vol. 198, S. 93-107, 1996

[50] Venkatesh T.A., Conner B.P., Lee C.S., Giannakopoulos A.E., Lindley T.C., Suresh S.:"An experimental Investigation of Fretting Fatigue in Ti-6Al-4V: the Role of Contact Conditions and Microstructure", Metallurgical and materials transactions A, Vol. A32, pp. 1131-1146, 2001

[51] Vincent L., Berthier Y., Godet M.: "Testing Methods in fretting fatigue, a critical appraisal", ASTM Publications, STP 1159, Philadelphia, S. 33-48, 1992, ISBN 0-8031-1448-6

[52] Vincent L.:"Materials and fretting" Freting Fatigue ESIS 18 (Edited by R.B. Waterhouse and T.C. Lindley) 1994, Mechanical Engineering Publication, London, pp.323-337

[53] Vingsbo O.B.:"Fretting and Contact Fatigue Studied wirh the Aid of Fretting Maps", Standardization of Fretting Fatigue Test Methods and Equipment, ASTM Publication, STP 1159, Philadelphia, pp. 49-59, 1992

[54] Vingsbo O., Söderberg S.: "On fretting maps", Wear, Vol. 126, S. 131-147, 1988

[55] Walker K.:"The effect of stress ratio during crack propagation and fatigue for 2024-T3 and 7075-T6 aluminium, in effects of environment and complex load history on fatigue life", ASTM STP 462, pp. 1-14, 1970

[56] Wharton M.H., Waterhouse R.B.:"Environmental effects in the fretting fatigue of Ti-6Al-4V", Wear, Vol. 62, 287-297, 1980

[57] Wörl H.:"Literaturrecherche über den Stand der Forschung bei reibdauerbeanspruchten zusammengesetzten Maschinenelementen", TU Chemnitz, 2003

[58] Zhou Z.R., Fayeulle S., Vincent L.:"Cracking behaviour of various aluminium alloys during fretting wear", Wear, 1992

[59] Zhou Z.R., Nakazawa K., Zu M.H., Maruyama N., Kapsa P., Vincent L.: "Progress in fretting maps", Tribology International, Vol. 39, S. 1068-1073, 2006

[60] Zhou Z.R., Pellerin V., Vincent L.: "Wear Mechanisms in Fretting of Aluminium Alloys", Ecole Centrale de Lyon, Department Materiaux, Meqanique, Physique, 69131, Ecully Cedex France

[61] Zhou Z.R. Vincent L.:"Mixed fretting regime", Wear, 1995

10. Symbols

10.1. Latin symbols

a	Radius of a contact area
C_α	Content of primary α-phase
$C_{(\alpha+\beta)}$	Content of (α+β)-phase
d	Arithmetic mean of d_1 and d_2
d_1, d_2	Diagonals of the Vickers pyramid indentations
e	Ratio for the barrier between fretting and reciprocating sliding
e_v	Wear energy density
E_d	Dissipated energy
E_i	Young's moduli
F	Applied load
F_N (or P)	Normal load
F_R	Friction force
F_T (or Q)	Tangential force
h_{TTS}	Depth of the TTS
HV	Vickers hardness
HV_α	Micro-hardness of the primary α-phase
$HV_{(\alpha+\beta)}$	Micro-hardness of the (α+β)-phase
$I_{1,max}$	Maximum of the first invariant of the stress tensor
$J_{2,a}$	Amplitude of the second invariant of the deviatoric stress tensor
k	Material parameter
$K_{Archard}$	Archard wear coefficient
K_{Energy}	Energy wear volume coefficient
l_m	Roughness measurement length
m_w	Wear mass
M	Fitting parameter for calculation of the shear stress range parameter
m	Fitting parameter for calculation of $\zeta_{effective}$
M_R	Friction moment
N	Normal load or cycles to failure
N_f	Cycles to failure
N_i	Cycles to crack nucleation
p	Pressure or hydrostatic pressure
p_0	Peak contact pressure
p_{Hertz}	Hertzian pressure
p_{max}	Maximum pressure
v	Sliding speed
V_w	Wear volume
q	Shear stress
R	Radius or stress ratio
R_a	Arithmetic mean height
R_q	Root mean square
$R(t)$	Probability
s	Local sliding distance
t	Shear fatigue strength
T	Temperature
x, y	Data set values

10.2. Greek symbols

α	Alpha-phase or material constant
β	Beta-phase or material constant
$\Delta\gamma_{max}$	Maximum shear strain increment
δ_a (or δ)	Displacement amplitude or relative slip amplitude
δ_0	Displacement amplitude when $F_T = 0$
$\Delta\delta$	Relative slip range
ε	Strain
μ	Coefficient of friction
μ_e	Energy friction coefficient
ζ_a	Stress amplitude
ζ_{bf}	Bending fatigue limit
$\zeta_{effective}$	Effective stress
ζ_{eq}	Equivalent stress
ζ_L	Bulk stress
ζ_m	Mean stress
ζ_{max}	Maximum stress
ζ_{min}	Minimum stress
ζ_{uts}	Ultimate fatigue strength
ζ_y	Yield strength
η	Shear stress
$\Delta\eta$	Shear stress range
$\Delta\eta_{crit}$	Critical shear stress range
$\Delta\eta_{max}$	Maximum shear stress range
η_{max}	Maximum shear stress
η_{st}	Shear fatigue limit
ν_i	Poisson ratios